Nitrogen-doped and Porous Carbons Towards New Energy Storage Mechanisms for Supercapacitors with High Energy Density

Dissertation

zur Erlangung des akademischen Grades

Doktor der Naturwissenschaften (Dr. rer. nat.)

in der Wissenschaftsdisziplin „Kolloidchemie"

eingereicht an der

Mathematisch-Naturwissenschaftlichen Fakultät

der Universität Potsdam

von

Runyu Yan

Potsdam-Golm, im Februar 2019

Acknowledgement

First of all, I would like to acknowledge my senior supervisor, Prof. Dr. Markus Antonietti, for providing me the opportunity to pursue my doctorate in Max Planck Institute of Colloids and Interfaces. All his fruitful discussions and the encouragement greatly enlightened me on my research topics, particularly regarding the ordering transitions in ionic liquids. I really appreciate his guidance and support not only for the research work, but also for my future career.

I express my deep acknowledgement to my supervisor Dr. Martin Oschatz for accepting me as one of his first Ph.D. students and leading me to the area of electrochemical energy storage. His tolerance towards my mistakes, great patience in the numerous and fruitful discussions, so many constructive suggestions, ideas and continuous supports paved the way for my Ph.D. study. With all his patient education in over two years, I gained plenty of fundamental knowledge regarding carbons, physisorption, and chemistry from zero basis. Without his splendid guidance and teaching, I would never have finished my dissertation as it is.

Thanks to Prof. Helmut Schlaad for being my second supervisor, reviewing this thesis, and providing me the opportunity to help teach the lab course as the teaching assistant.

Many thanks to Guigang for helping me with the topic transfer to electrochemical energy storage, which imposes significant influence on my future career.

Table of Contents

1.   Motivation

Energy access is the "golden thread" that weaves together economic growth, human development and environmental sustainability. Energy has long been acknowledged as a vital role for human beings to develop and thrive. However, a growing gap gradually emerges between the energy demand and energy supply. With average growth of 84 million people per year, the global population is expected to reach up to 9.8 billion by 2050.[1] Together with the improving life standard in the majority of the countries, there is an ever-growing energy demand led by China and India (**Figure 1.1**), which increases from around 9,100 TWh in 2016 to approximately 13,700 TWh (50 percent increase) by 2040.[2] Turning to the supply side, fossil fuels remain dominant, but the limited sources of fossil fuels tend to be depleted in the future, contradicting to a demanded sustainability of human society. Its usage is generally accompanied with the release of large amounts of various pollutants (CO_x, SO_x, NO_x; dust, ash, organic by-products), which causes serious environmental issues such as global warming and Chinese haze.
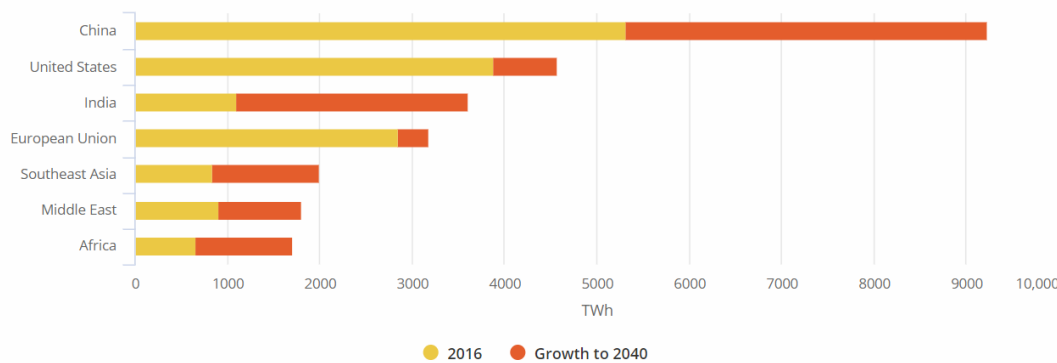
Figure 1.1. Electricity demand by selected region.[2]

For those reasons, great attention and efforts have been devoted to the utilization of renewable energy sources (primarily solar, wind, geothermal, and hydropower), which are sustainable and cause less contamination. According to the International Energy Outlook 2017, renewable energy has become the world's fastest-growing energy source, increasing an average of 160 GW a year over the period from 2017 to

2040. This is higher than the sum of coal, gas, and nuclear (**Figure 1.2**). By 2040, the share of all renewable energies will reach 40% in total power generation as the least-cost energy source, and they are predicted to capture two-thirds of global investment in power plants. More specifically, fast development of solar photovoltaic, especially in China and India, endows solar energy the largest source of renewable capacity by 2040. In the European Union, renewable energies take up 80% of new capacities and wind energy is about to turn into the leading renewable source until around 2030.[2]
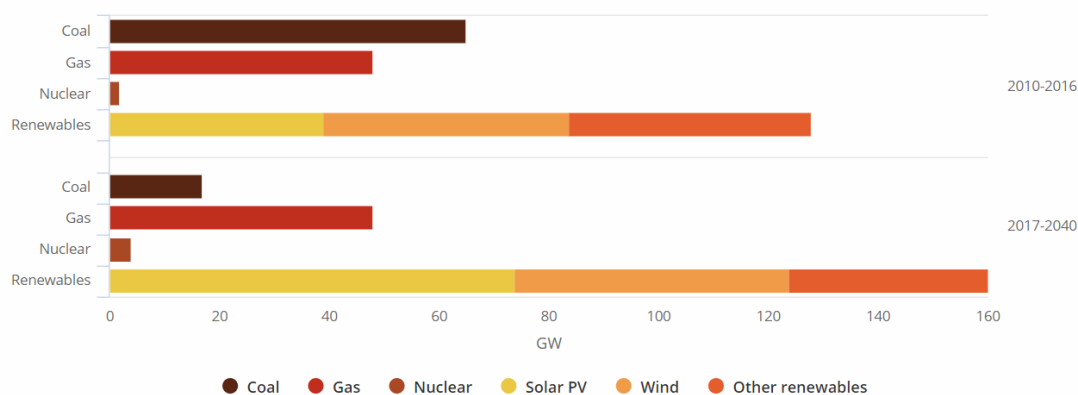
Figure 1.2. Global average annual net capacity additions by type. [2]

The future is electrified, with the electricity as the basis of the 'nervous system' of our society in the perspective of distributing information and energy elegantly and efficiently. Statistically, the growing pace of electricity demand is twice that of the whole energy demand. Consequently, the most appealing and effective way to utilize the renewable energies is the electricity production, such as by wind and solar power plants. These energy sources are inexhaustible, sustainable, and pollution-free, which causes innumerable attention and efforts for efficient utilization both in academia and industry. With the cost of electricity production from renewable sources decreasing to an affordable level and even lower in the future, there gradually emerges another big challenge, namely the time discrepancy between energy supply and usage. Typically, the most powerful time of electricity production by solar power plants is during midday and in summer, while the energy demand mostly reaches the peak during evenings and in winter

(**Figure 1.3**). In the case of wind power plants, the electricity generation is generally irregular. The large gap between the energy supply and usage leads to great energy dissipation. The more elegant and efficient utilization of renewable energies require energy storage techniques with large-scale capacity, including compressed air, pump storage, thermal energy storage, and electrochemical energy storage. The mostly common used technique is the pump storage due to its admirable overall efficiency of more than 75 % as well as the lack of energy loss during storage. But its further deployment is hindered by the enormous investment cost and the special location requirements. Electrochemical energy storage, with its high efficiency, absence of geographical restrictions, and gradually decreasing costs, has emerged as an alternative approach in recent years. Besides, continuous and forceful support by policies worldwide pushes the expansion in the global electric vehicles markets with a rapid rate, which is about to approach 300 million cars by 2040 (**Figure 1.4**). Rechargeable batteries are a key element in these contexts. Currently, lithium-ion batteries and supercapacitors are to the fore, in the future sodium-based batteries will certainly play a crucial role as well.[3] One concept alone can hardly be adapted to all the application scenarios. The future must lie in the combination of different electrochemical energy storage concepts. However, in every specific technology, there exist problems that urgently need to be addressed, such as the small reserves of lithium for lithium-ion batteries,[4] undesirable cycling stability for batteries, and insufficient energy and power density for all techniques.[5] Thus, the development of each technique is by no means less substantial.

Example Seasonal PV Production vs. Loads
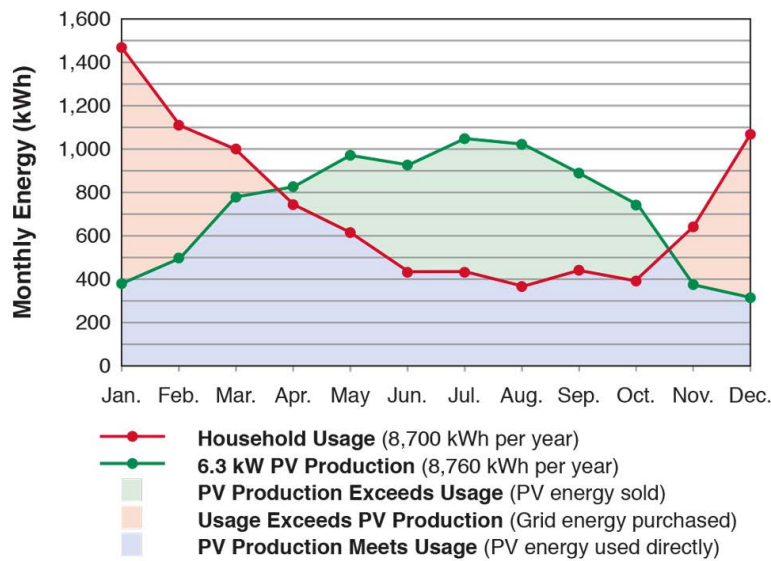
Figure 1.3. Mismatch between energy produced by photovoltaics and household power demand in Canada.[6]
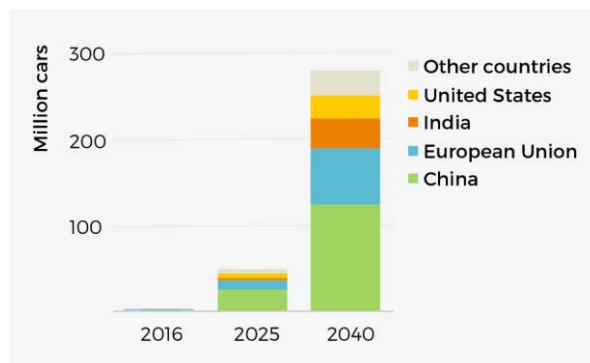
Figure 1.4. Electric car fleet, 2016-2040.[7]

Electrode materials are the core part in all electrochemical energy storage devices. Porous (heteroatom doped) carbon materials have been acknowledged to be of vital significance in this context due to their abundant sources, large specific surface area, high electric conductivity, and excellent chemical/thermal stability.[8-11] Numerous studies have verified their versatile application in different scenarios, including but not limited to conductive additives in electrodes,[12] electrodes for supercapacitors,[9] cathode hosts for lithium-sulfur batteries,[13] anodes for sodium-ion batteries,[14] and current collectors for metal anodes.[15] In many cases, the optimal

designs of pore structure and chemical functionality/atomic construction seem to have been achieved on the basis of traditional theories. But for the further momentous improvement, it is crucial to establish novel and fundamental mechanisms for different given applications. Accordingly, the designs of porous carbon materials need to be adjusted and optimized.

Hence, this dissertation aims at developing novel carbon materials and synthetic routes for the better performance for different electrochemical energy storage devices (electrochemical double layer capacitors and sodium-ion capacitors), and revealing currently ambiguous energy storage mechanisms in these devices. More importantly, these carbons are employed as model systems to provide experimental evidence for the comprehensive interpretation and profound understanding of the relationship between the intrinsic material property and the ultimate device performance. Thus they contribute to future targeted design of optimal carbon based electrodes.

2. Background and Outline

2.1. Porous carbonaceous materials

"Carbon is the essential building block of life", written by Eric Roston in *The Carbon Age*,[16] which indicates the significance of carbon to all aspects of our lives and the human society. Indeed, albeit carbon ranks the 17th in terms of the terrestrial elements abundance, with the amount of only ~180 ppm, it is one of the most crucial elements which has, together with hydrogen, the largest number of compounds. This is due to its upmost tendency to form covalent bonds with all similar atoms, as well as the versatile combination with elements of very different electronegativities according to its position in the periodic table of elements. While the majority of these chemical compounds belong to the category of organic chemistry, only a limited number of them belong to the area of inorganic chemistry or materials science.[17-18]

Yet, in the field of inorganic chemistry, even the elementary substance carbon plays a vital role because of its various allotropes and versatile applications. The importance is further identified by the peer-reviewed journals of *Carbon* (published by Elsevier Science) and *C* (published by MDPI) which are named after the element carbon, and it is the exclusive one that is endowed with this special "honor". The carbon allotropes, namely graphite and diamond, provide versatile physical and chemical properties. Graphite, composed of sp^2 hybridized carbon atoms (**Figure 2.1**b), is the thermodynamically stable form at atmospheric conditions which features the opaqueness, high electrical conductivity, and softness (Mohs scale hardness 1-2). In contrast, diamond is a sp^3 hybridized carbon framework (**Figure 2.1**a) with the opposite characteristics including transparency, wide band-gap semiconductivity, and the highest known hardness (Mohs scale hardness ~10). Recently, carbon nanomaterials, with their nanometer scale structural units, have aroused considerable attention in both academia and industry due to their

extraordinary properties. Typical examples contributing to the "the new carbon age" are nanodiamonds, carbon nanofibers, graphene, carbon nanotubes, and fullerenes. Graphene is a single layer composed of sp^2 hybridized carbon atoms, forming a two-dimensional carbon nanomaterial (**Figure 2.1**c). This specific structure gives rise to the outstanding electrical conductivity, the highest tensile strength, and the ultra-high theoretical external specific surface area up to 2630 m^2 g^{-1}.[19] Carbon nanotubes are formed by the rolling of the graphene layer(s) (**Figure 2.1**d),[20] and fullerene is the carbon-atom cage composed of a specific number of carbon six rings and five rings, such as the well-known "football molecule" C_{60} (**Figure 2.1**e).[21] Moreover, graphene is regarded as the basic building blocks of intrinsically porous carbon materials, which can be simplified as highly disordered and defective graphite (**Figure 2.1**f). In contrast to the aforementioned carbon materials, porous carbons feature the large internal surface area and an amorphous state with rather defective microstructures and less well defined local atomic construction.[22]
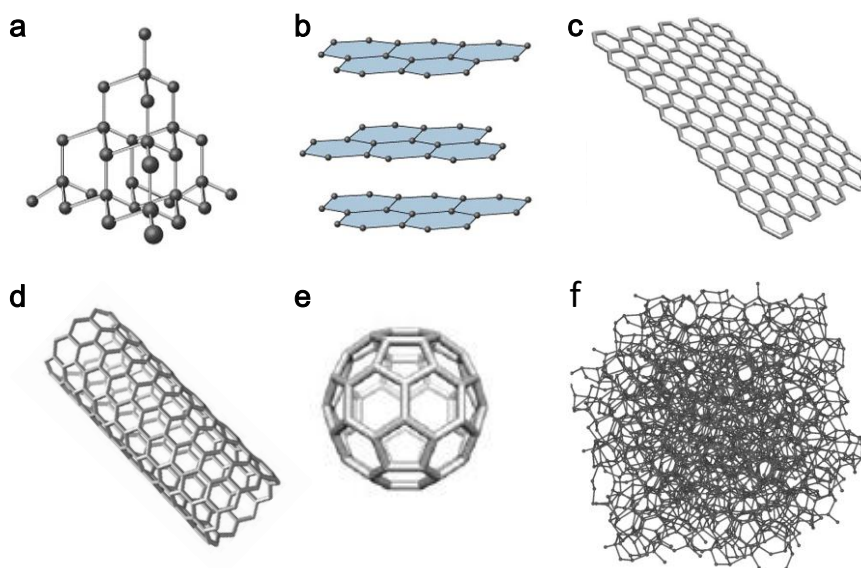
Figure 2.1. Structure of different carbon allotropes: (a) diamond, (b) graphite, (c) graphene, (d) carbon nanotube, e) fullerene, and (f) porous amorphous carbon.[22]

Amorphous porous carbons are a vital branch of the carbon materials, on account of their high specific surface area, inexpensive synthetic approach, and easily adjustable properties.[23] Together with their high thermal, chemical, and mechanical stability, abundant reserves, they provide versatility in various applications like electrochemical energy storage, catalysis, gas adsorption, pollutants removal, just to name a few.[24-27] Besides, the pore size and pore geometry of porous carbons are of great importance for all the applications. Thus achieving optimal pore structures in these materials is an important research area. Generally, in spite of the low cost, commercial porous carbons are often depreciated because of the wormlike or bottleneck-structured pores, which impede efficient mass transport that is very crucial in many applications.[28] This justifies the intensive studies in the optimal design and precise adjustment of the pore structures. From a geometrical perspective, a pore is surface curvature that is deeper than it is wide. According to the International Union of Pure and Applied Chemistry (IUPAC) conventions, nanopores are those with the width below 100 nm. Pores are categorized by their diameters into three types, namely micropores (< 2 nm), mesopores (2-50 nm), and macropores (> 50 nm).[29] There is no universal optimal design of porosity for porous carbons, where different applications require different porosity characteristics. Parameters derived from physisorption experiments, namely the specific surface area (SSA), total pore volume (TPV), and pore size distribution (PSD), are the main indicators to characterize the porosity properties. The significance of each parameter varies with specific applications. The SSA are crucial to some surface-dependent applications such as catalysis, adsorption, and supercapacitors.[11] The high TPV is beneficial to the high loading amounts of active materials when employing porous carbons as their conductive hosts (such as sulfur cathodes in lithium-sulfur battery), while it shows negative effects on the volumetric capacitance when employing as the electrodes for supercapacitors.[28] The PSD has significant influence on applications related to mass transport properties, such as

the rate capability in all kinds of electrochemical energy storage devices and the accessibility of active sites in catalysis.[30] All these requirements have to be taken into consideration and must be carefully balanced. Hence, it is of great importance to investigate different synthetic approaches for porous carbons with tailored porosity, and to reveal the performance-structure relationships for specific applications.

2.1.1. Activation approaches for synthesis of porous carbon materials

The porosity of carbon materials can be generated through various approaches. One important method to produce microporous carbons on an industrial scale is activation. About half a million tons of such "activated carbons" are produced per year. Activation can be divided into physical and chemical activation.[31] Physical activation is a two-step procedure. First, the raw carbon material is transformed into char with rudimentary porosity by pyrolysis under inert gas atmosphere, and, second, the char is treated with the activation agent at high temperatures. CO_2 and steam are the most employed physical activation agents.[32] In principle, physical activation leads to etching of carbon atoms from the amorphous carbon framework giving rise to porosity. The CO_2 activation is based on the well-known Boudouard equilibrium (Equation (2.1)). At high temperatures, the equilibrium is enthalpically and entropically shifted towards gaseous carbon monoxide (CO) causing carbon etching. In terms of the steam activation, water can etch carbon atoms through the formation of CO and hydrogen (Equation (2.2)).

$$(1+x)\ C(s) + CO_2(g) \rightleftarrows 2\ CO(g) + x\ C(s) \tag{2.1}$$

$$(1+x)\ C(s) + H_2O(g) \rightleftarrows H_2(g) + CO(g) + x\ C(s) \tag{2.2}$$
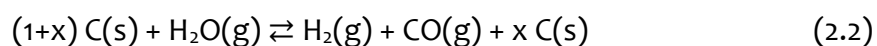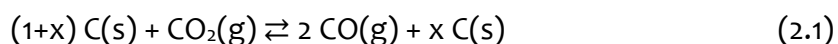
Due to its simplicity and broad applicability, physical activation is regarded as a rather economically friendly and benign process. However, its drawbacks include the large energy consumption, and more importantly the very low yield.[31]

In contrast, chemical activation is featured by the reaction of a carbon precursor with a chemical agent, such as potassium hydroxide, phosphoric acid, and zinc

chloride.[33] Typically, the precursor is impregnated with a highly concentrated, aqueous solution of the activation agent. Afterwards, the resulting composite is calcinated under an inert gas atmosphere. During calcination, carbon atoms are partially etched through chemical reactions with the activation agent, generating the porosity. Finally, the redundant activation agent and reaction product are removed by washing to yield the porous carbon material.[34] Compared with physical activation process, although the porous carbons synthesized by chemical activation show a relatively more well-defined porosity, they generally contain a larger amount of functional groups, and require additional synthesis steps (washing and drying).[31]

Nevertheless, the activated carbons mainly feature a microporous character, which is often coupled with a worm-like or bottleneck pore structure. This can inhibit the mass transport of the guest species, and impede the accessibility of the surface for large molecules.[28] Such pore system is also generally not applicable for size-selective applications. On the other hand, activation approaches can hardly provide control over the carbon morphology.[35] One way to solve these problems is templating method, which allows precise control over (meso- and macro-)pores and morphology.[28]

2.1.2. Templating approach for synthesis of porous carbon materials

In general, the templating approach can be defined as the synthesis of a substance in the presence of a structure-directing agent (denoted as a template). The removal of the template leads to voids, giving rise to a porous structure. Thus, the pore size and pore structure are determined by the employed template. According to the templating mechanism, templating methods can be classified into exotemplating and endotemplating, where the materials are synthesized either inside or around the template, respectively. Endotemplated structures always generate a continuous phase of the porous material, while exotemplating can lead to separated structures, e.g., particles or rods. More importantly, the most common

classification concerns the nature of the template, which leads to two categories, namely hard templating and soft templating.[36-38]

Hard templating is comparable to a casting process on the nanoscale, giving rise to the expression "nanocasting".[39] Typically, carbon precursors are infiltrated into a porous solid template which acts as a space confinement ("casting mold"), followed by heat treatment and subsequent template removal. This procedure yields carbons ideally representing the inverse replica of the void space of the template. Therefore the pore size, pore structure, and pore connectivity are directly dictated by the template used, and therefore, can be easily adjusted. For example, the probably most prominent hard templated carbon material is the hexagonal ordered mesoporous CMK-3 representing the inverse replica of ordered mesoporous silica SBA-15 (**Figure 2.2**).[40-41] The major drawback lies in the harsh conditions needed for the silica removal (by washing with highly toxic hydrofluoric acid or hot concentrated sodium hydroxide aqueous solution).

Another example are the ZnO-templated carbons, where zinc oxide nanoparticles are employed as the hard template. During carbonization, ZnO reacts with carbon through carbothermal reduction according to the following reaction (Equation (2.3)).[42]

$$ZnO(s) + C(s) \ \rightarrow \ Zn(g) + CO(g) \tag{2.3}$$
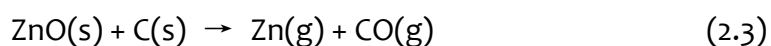
The pyrolysis temperature above the boiling point of Zn leads to its removal through evaporation. Together with the release of CO gas, it also gives rise to the generation of micropores interconnected with the mesopores generated from the ZnO template.[42] In spite of its great control over the pore structure, hard templating can hardly be scaled up due to the high-cost and time-consuming process of the hard template synthesis prior to the whole process.
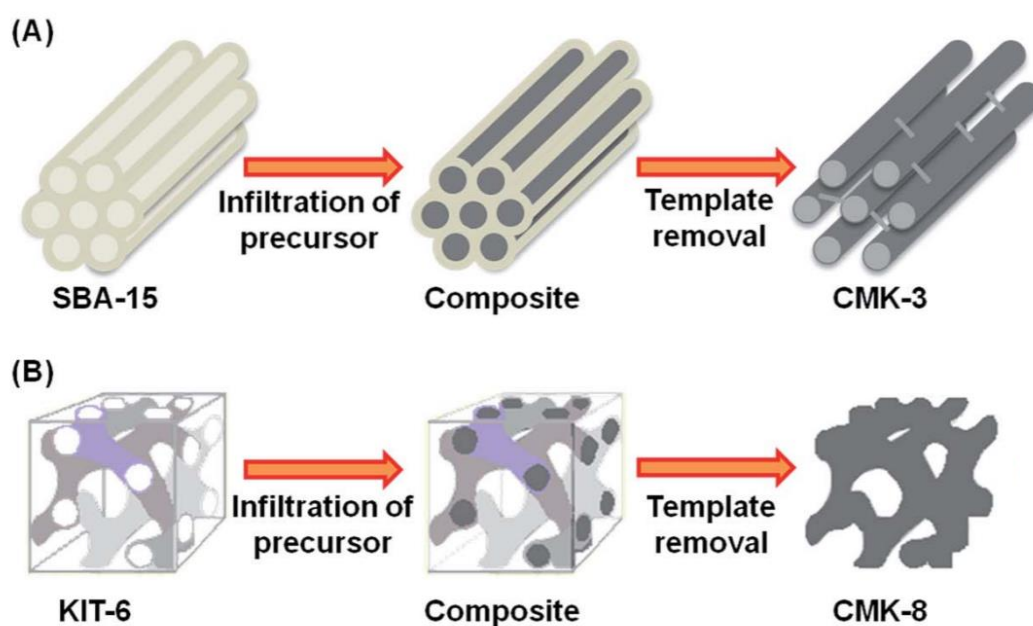
Figure 2.2. Synthesis of mesoporous carbon via hard templating employing silica templates.[41]

Soft templating employs the self-assembly of soluble, amphiphilic molecules into micelles or liquid crystals as templates. The molecules typically are surfactants, e.g., cetyltrimethylammonium bromide, or block co-polymers such as the poly(ethylene oxide)-based Pluronics®.[43] The self-assembly is driven by a combination of non-covalent, mostly weak interactions such as Coulomb and van-der-Waals forces. The desired porous material is obtained by polymerization of precursor molecules, which self-assemble around the building blocks, i.e., micelles or liquid crystals (**Figure 2.3**).[44] The direct synthesis of soft templated carbon materials was reported by Zhao et al., where he used the co-assembly of block co-polymers as structure-directing agents and phenolic resin as the carbon precursor, followed by carbonization and in-situ template removal.[45] Carbons with various pore geometries from hexagonal to cubic and lamellar structures can be achieved through changing constituents of the block co-polymers and adjusting the ratio of the precursor to the block co-polymers. However, the obtained SSAs are usually lower than 1000 m² g⁻¹, obstructing the performance of soft templated carbons.[38]
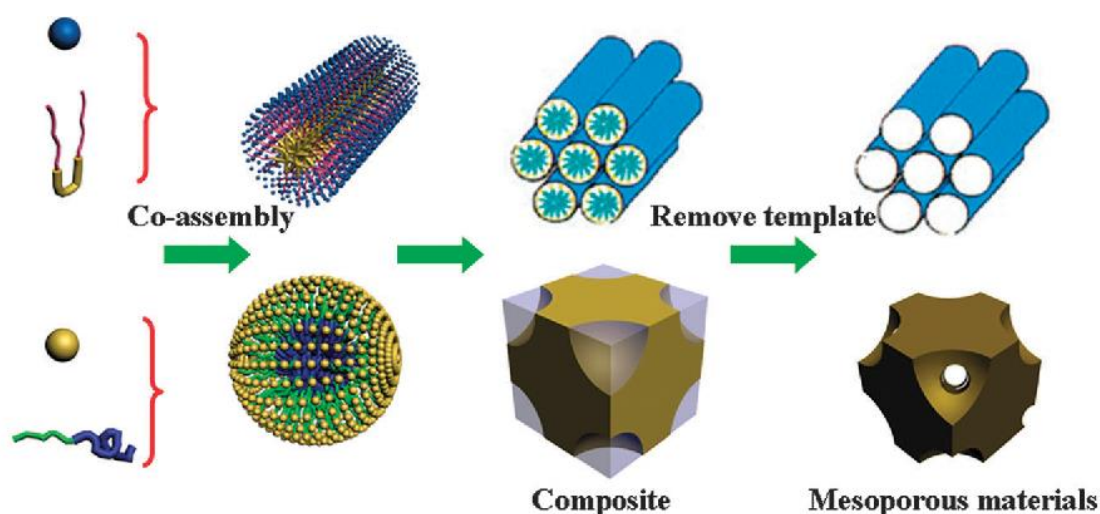
Figure 2.3. Synthesis of ordered mesoporous materials via soft templating.[44]

Salt templating employs salt melts as reaction mediums to synthesize highly porous carbons. Hence, any reaction carried out in a molten salt (independent of the reaction temperature, such as ionic liquids or deep eutectic solvents) can be regarded as a salt templating process.[46] For instance, the pyrolysis of glucose inside a eutectic LiCl/KCl mixture can generate highly porous carbons. The two salts were simply mixed with the precursor, followed by heating under an inert gas atmosphere. The salt, which is still present in the obtained composite, is removed by aqueous washing, yielding the porous carbon. Through this method, porous carbon or graphene can be synthesized by adjusting the amount of salts (**Figure 2.4**), indicating the clear influence of salt amounts on the resulting carbon structure/porosity.[47] Besides, the morphology/pore structure of the porous carbon is also highly dependent on the components of the eutectic salt mixture, where LiCl/ZnCl$_2$, NaCl/ZnCl$_2$, and KCl/ZnCl$_2$ lead to distinctly different pore structures (**Figure 2.5**).[48]
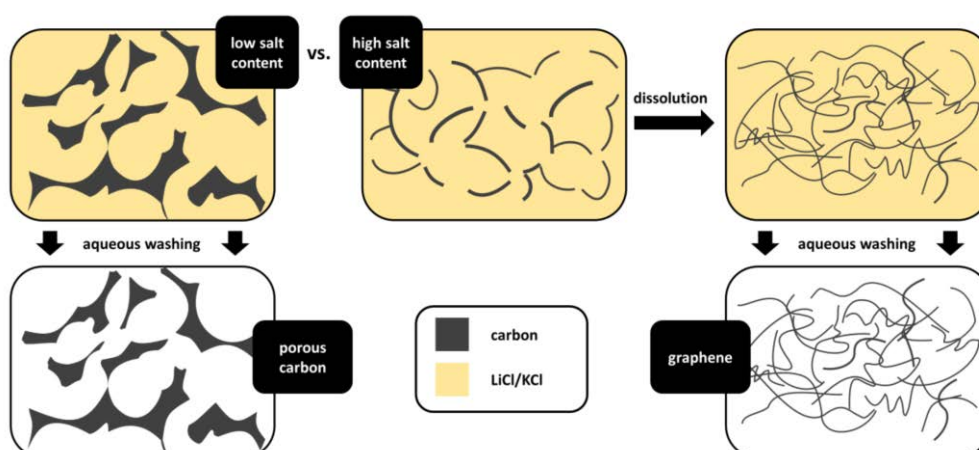
Figure 2.4. Schematic illustration of the formation of porous glucose derived carbon in molten LiCl/KCl at low salt content and the formation of graphene at high salt content.[47]
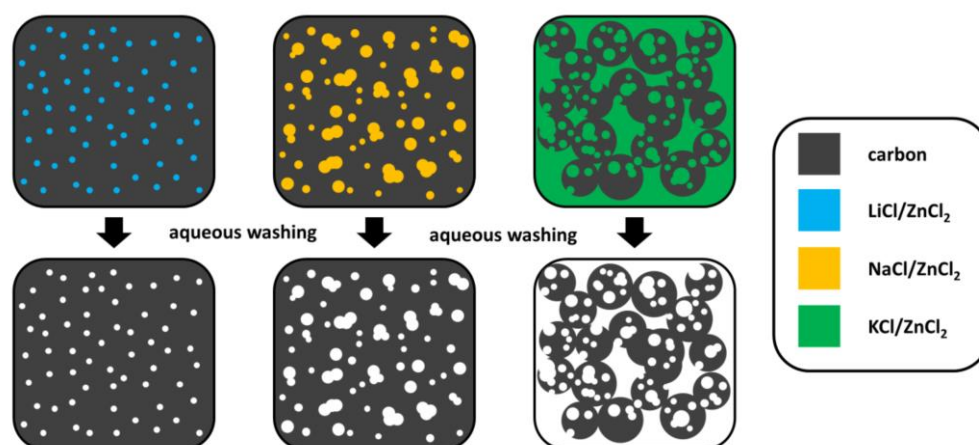
Figure 2.5. Schematic illustration of the obtained carbon morphology/porosity depending on the used salt mixture during the ionothermal synthesis of ionic liquid derived carbon materials.[48]

2.1.3.   Porous nitrogen-doped carbons

The introduction of nitrogen atoms into a carbon framework not only alters surface properties but also the electronic structure of the material. Nitrogen doping can greatly influence the performance of the carbon materials in different applications, like gas adsorption, supercapacitors, batteries, and electrocatalysis, when compared to the non-doped counterpart with similar pore structure. In nitrogen-doped carbons (NDCs), single carbon atoms in the graphitic lattice are replaced by nitrogen atoms (**Figure 2.6**). Hence, the graphitic structure is retained in large parts

of the material. Through nitrogen doping, properties of the corresponding carbon materials (like porosity, conductivity, basicity, stability against oxidation and catalytic activity) can be changed to varying degrees according to the nitrogen content and nitrogen species.[49]

There are mainly two approaches for the synthesis of NDCs: a) post-treatment of carbon materials, which is typically accomplished by heat treatment in reactive nitrogen containing reagents (NH_3, CH_3CN, CH_2N_2); b) directly employing nitrogen-containing precursors to incorporate nitrogen into the porous carbon framework upon pyrolysis. The latter pathway usually leads to structurally incorporated nitrogen-sites and simplifies the process because treatment under nitrogen containing reagents is not necessary.[49] It generally results in a much higher nitrogen content than the post-treatment approach. Typical examples include graphitic carbon nitride (g-C_3N_4)[50] and nitrogen-rich carbon (C_2N),[51] which exhibit some special characteristics like semiconductivity and high polarity.
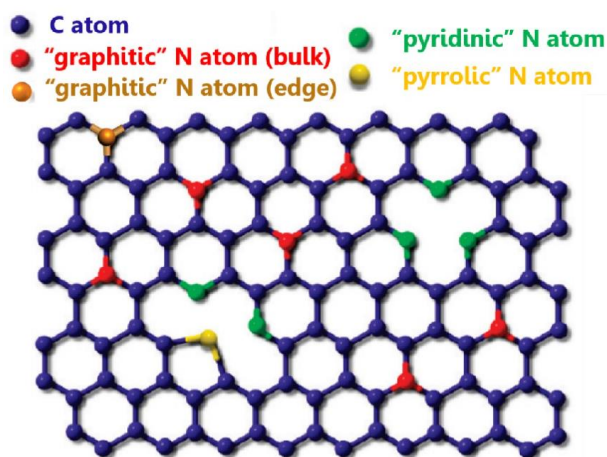
Figure 2.6. Examples for possible nitrogen functionalities present in nitrogen doped carbons.[52]

2.2.   Electrochemical double layer capacitors

Due to the increasing environmental pollution and the depletion of fossil fuels, it is an urgent task for human beings to search for alternatives to the established energy conversion and storage systems. Consequently, exploiting sustainable and clean energy as well as efficient energy conversion and storage technologies is

urgently required. Many countries and multinational associations have put forward plans to meet the rigorous challenge, paying great attention to the utilization of energy from renewable sources, such as solar or wind energy. However, the large fluctuations of such renewable energy sources impose paramount challenges to power grid management owing to the mismatch between the electricity supply and the actual energy demand. To tackle this problem, various approaches have been developed including mechanical, physical, thermal, chemical, and electrochemical energy storage systems. The significance for energy and power supply is substantial and will significantly increase in the future. Electrochemical energy storage is a key element in that context. Therefore, as electrochemical energy storage devices, rechargeable batteries and/or supercapacitors have raised more and more attention in recent years not only because of their reliability, stability, sustainability, but also due to the flourishing prosperity of electric vehicles all over the world.

As one category of supercapacitors, electrochemical double layer capacitors (EDLCs) with capacitance values much higher than the traditional electrolytic capacitors can bridge the gap between electrolytic capacitors and rechargeable batteries. They typically store 10 to 100 times more energy per unit volume or mass than electrolytic capacitors and can accept and deliver charge much faster than batteries. They can also tolerate many more charge and discharge cycles than rechargeable batteries (**Figure 2.7**a).[53]
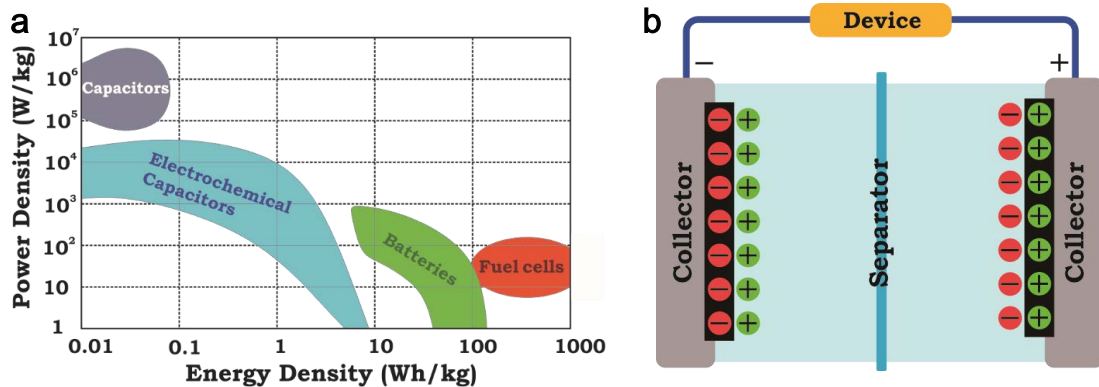
Figure 2.7. (a) Specific power plotted against specific energy, also called the Ragone plot, for various electrochemical energy storage devices. (b) Schematic illustration of the ion adsorption process which is the main energy storage mechanism in EDLCs.

Historically, capacitors were evolved from Leiden jars, which were made by coating the inside and outside of jars with metal foil, leaving a space at the mouth to prevent arcing between the foils. The metal foils and the jar acted as the electrodes and dielectric, respectively. During the charging process, positive charges gradually accumulate on one metal foil while negative charges accumulate on the other. The discharging process takes place through connecting these two electrodes by a conductive wire with or without a load. Dielectrics are the materials that can be polarized by applying an electric field. In general, the dielectric is electrically insulated, including a vacuum, a non-ionized gas, a solid such as a ceramic or polymer, and a liquid (aqueous or non-aqueous electrolyte). Early capacitors were fabricated as primary circuit elements for radio receivers, which were mainly utilized to hold microfarad to picofarad charges of direct current or to filter the frequencies for alternating current circuits.[54-55] Solid insulators like glass, porcelain, paper, and mica were employed as the dielectrics for the early capacitors. In 1890s, Charles Pollak invented the first electrolytic capacitors with liquid electrolytes as dielectrics, which was granted as the U.S. Patent "Electric liquid capacitor with aluminum electrodes". In 1957, H. Becker developed a low voltage electrolytic capacitor with porous carbon electrodes, which was the earliest EDLC prototype. Early EDLCs used two aluminum foils covered with activated carbon as the

electrodes, which were soaked in an electrolyte and separated by a thin porous insulator. This design gave the EDLC with a capacitance on the order of one Farad, significantly higher than electrolytic capacitors of the same dimensions. This fundemental mechanical design remains the basis of most EDLCs.[56]

Unlike secondary batteries which store energy by time-consuming redox-reactions, charge storage in EDLCs is mainly achieved by reversible adsorption of electrolyte ions on the surface of charged electrode materials through electrostatic forces (**Figure 2.7**b).[57] Thus, EDLCs stand out by the high specific power, the long cycle life, and the broad range of operating temperatures,[58-59] and are attractive for applications requiring many rapid charge/discharge cycles rather than long term compact energy storage.[60] For instance, they are applied in cars, buses, trains, cranes and elevators, for regenerative braking, short-term energy storage or burst-mode power delivery.[61-62] However, the energy density of EDLCs (lower than 10 Wh kg^{-1} for commercial devices) is still far from being satisfactory.[63] It remains an enormous challenge to increase the energy density of EDLCs without sacrificing their most valuable characteristics, the distinguished power density and superior cycling stability.

Carbonaceous materials are a type of prospective electrode material for EDLCs, due to their abundance, easy processing, non-toxicity, high specific surface area, good electronic conductivity, high chemical stability, and wide operating temperature range. Various carbonaceous materials, including porous carbons, carbon nanotubes, graphene, and heteroatom-doped carbons, have been applied as electrode materials for supercapacitors over the past years. Their porosity (the size, geometry, and distribution of the nanopores) plays a vital role for the EDLC performance.[28, 30] This justifies the current tremendous attempts to tune the porosity of porous carbons on both the micropore and mesopore scale. Theoretically, the porosity influences the specific capacitance and rate capability through two major aspects: (1) narrow micropores with diameters in the range of

the size of the electrolyte ions result in high capacitance because the solvation shell can be partially "stripped off" and the ions experience strong adsorption due to simultaneous electronic interaction with both sides of pore walls (**Figure 2.8**a).[30, 64-66] The "stripped off" processes when the ions enter or leave the pores can lead to the additional stored energy; (2) "Transport highways" such as ordered mesopores (i.e., pores of 2-50 nm in size of uniform geometry and orientation) enable rapid diffusion of electrolyte ions onto the inner surface of the porous electrode (**Figure 2.8**b).[67-69] These additional transport paths will decrease the volumetric efficiency of the EDLC device but can give rise to outstanding rate capability because the high storage capacity of the micropores can only be utilized under high-power conditions if the ions have rapid access to these adsorption sites.[28, 63] In this regard, it is quite promising to develop hierarchical porous carbon materials, which exhibit both narrow micropores providing high surface areas and larger mesopores for efficient ion transport.[28] Therefore, great efforts have been devoted to introducing secondary mesopores into microporous carbons through templating approaches. Likewise, micropores were created in mesoporous carbons by activating or etching methods.[70] Besides the pore structure design, surface functionalization is another effective approach to improve the capacitive performance of carbon materials. The most popular heteroatoms introduced into the carbon frameworks are nitrogen, oxygen, boron and sulfur.[71] Among these, nitrogen-containing carbon materials have been widely investigated as electrode materials for EDLCs. The capacitance of nitrogen-doped carbons has been promoted to over 300 F g^{-1} (voltage window of ~1 V in aqueous electrolytes) due to the introduction of pseudocapacitance effects and stronger ion adsortion on such polar sites.[72-74]
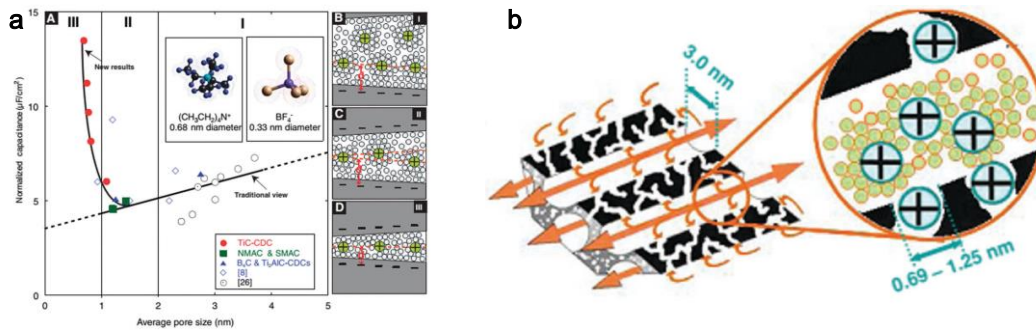
Figure 2.8. (a) Plot of specific capacitance normalized by BET SSA and average pore size for carbons. (b) Schematic of the porous structure characteristic and the ion transport process inside ordered hierarchical mesoporous/microporous carbon.[75]

The liquid electrolytes can be classified as aqueous electrolytes, organic electrolytes and ionic liquids (ILs). Three representative aqueous electrolytes are based on acid, alkaline, and neutral solutions, possessing high ionic conductivities but narrow operating voltage windows. Most commercial EDLCs use organic electrolytes owing to their wider operation potential windows, but are sometimes associated with safety risks because of the flammability, volatility, and toxicity of the organic electrolytes and improper use such as overcharge or short-circuit.[76] Due to the square dependence of energy density on the applied voltages (Equation (2.4)), ionic liquids with the large electrochemical voltage window (up to 4 V) are very promising alternative electrolytes for EDLCs.[77]

$$E = 1/2 \ CU^2 \hspace{3cm} (2.4)$$

They stand out also because of the negligible volatility, non-flammability, and large operational temperature ranges. However, their high viscosity and high cost limit their practical application. The ion transport in ILs is slow in the bulk and could be even slower in carbon nanopores, leading to sluggish charging dynamics and lowered power density. Resolving these issues necessitates the fundamental understanding of transport dynamics in nanopores filled with ILs. Besides, ILs are solely composed of ions without slovents. Thus they can hardly be compressed into a compression double-layer on the electrode surface,[78] where the traditional electric double-layer theory is not applicable. Therefore, their energy storage

mechanism remains unclear. Hence, on one hand, many efforts have been devoted to developing novel carbon electrode materials with elaborate pore structures and surface functionalities. On the other hand, it is essentially significant to implement IL electrolytes with large voltage windows and unclose the fundamentals of the energy storage mechanism.

2.3. Sodium-ion capacitors

As a recently developed kind of supercapacitors, hybrid ion capacitors (HICs), including Li-ion capacitors (LICs) and Na-ion capacitors (NICs) are another promising tactic to tackle the challenge of the inferior energy density of EDLCs. HICs contain a high-energy battery-type anode and a high-power capacitive-type cathode (**Figure 2.7**a).[79] From the mechanistic point of view, charges are simultaneously stored in the HIC by anion adsorption on the capacitive-type cathode surface and via faradic cation intercalation/reaction in the battery-type anode, respectively (**Figure 2.7**a).[80] Combining the working mechanisms of high power EDLCs and high energy batteries, HICs provide the possibility to combine their individual advantages. Moreover, the charge-discharge processes of these two electrodes are performed in different potential ranges (the anode at high negative working potentials where alkali metals are strong and the supercapacitor cathode at high positive potentials which are usually not accessible to battery set-ups), thus enlarging the operating voltage window (**Figure 2.7**b), which is among the most efficient methods to enhance the energy density.[77-78]
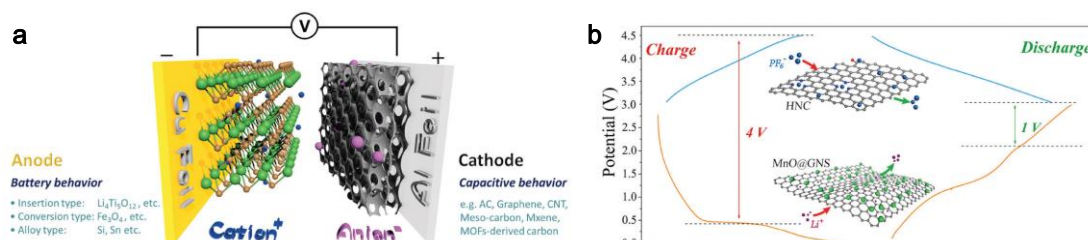
Figure 2.7. (a) Typical cell structure and electrode materials of a metal-ion capacitor. (b) Charge-discharge voltage profile of a typical LIC device.[80]

In contrast to LICs, NICs do not suffer from the limited abundance of lithium. The reserves of sodium (2.36 wt%) on our planet are 3 orders of magnitude higher than those of lithium (0.002 wt%). However, the weight and size of sodium ions are significantly larger than that of lithium, which generally leads to the inferior capacity and rate capability of sodium-ion based energy storage devices. This problem escalates in the anode for NICs, as the biggest obstacle in the development of high-performance NICs lies in the kinetic imbalance between the capacitor-type cathode and battery-type anode. That is, the redox process in the anode is much slower than the physical ion adsorption process in the cathode (usually nanoporous carbon).[80] This causes intensive efforts to develop faradic anodes with sufficient dynamics to match the non-faradic cathode.

Promising candidates for anode materials include various carbonaceous materials,[81-84] metal/alloys,[85] metal oxides,[86-87] and metal sulfides (**Figure 2.7**a).[88-90] Among them, carbon materials have attracted considerable attention due to their high storage capacity for sodium, high electrical conductivity, abundant resources, excellent stability, and low cost. Great efforts have been devoted to tailoring the atomic construction and porosity of carbons[91-93] which can contribute to sodium storage and promote rapid ion transport, thus facilitating the rate capability of the anodes. The introduction of heteroatoms, especially nitrogen, has been regarded as another promising approach in terms of providing additional charge storage capacity through reversible binding of sodium to the nitrogen-based functional groups.[81]

In addition to the development of advanced materials for NIC anodes, the mechanism of sodium storage in carbon materials is still not completely understood. Generally, the main contribution for sodium storage originates from the deposition of sodium species on the surface of carbon materials including defective sites and functional groups, plus the intercalation of sodium into the expanded graphene layers of the carbons. It is believed that these two processes proceed in different

voltage ranges, leading to the distinctly different charging/discharging behaviors in galvanostatic charge-discharge and cyclic voltammetry profiles. Nevertheless, it remains ambiguous which voltage range corresponds to each process. The traditional model proposed by Stevens and Dahn[35, 94-95] shows a strong discrepancy with other recent reports which propose a diametrically opposed model.[96-98] Typically, in the high and low voltage regions, the shape of the galvanostatic charge-discharge curve for carbon materials presents slope and plateau, respectively. The traditional model supposes that the capacity in the slope region is attributed to the insertion/extraction of Na^+ between the graphene layers, while the plateau area arises from the adsorption of the Na^+ into the voids between randomly stacked layers.[35, 94-95] On the contrary, the complete opposite process has also been verified by several studies, with the high and low voltage regions corresponding to surface absorption of Na^+ and insertion/extraction of Na^+ between the carbon interlayers, respectively.[96-98] Therefore, there is still a lack of systematic studies and comprehensive interpretation of the mechanism of sodium storage in carbon (and especially in nitrogen-doped carbon) materials.

2.4. Outline

To tackle the problem of the inferior energy density of supercapacitors, advanced electrode materials and new energy storage mechanisms have to be developed, optimized and employed. Porous carbons used as electrodes in EDLCs and NICs are of great importance in these concepts. Intensive efforts all over the world have been devoted to the development of new synthesis routes for porous carbon materials. The tailoring of the porosity features is especially promising due to the direct relation between porosity characteristics and the supercapacitor performance. Moreover, nitrogen doping tends to be quite promising for anodes in the NICs, rating them as alternatives to the hard carbon materials commonly employed. However, in respect of carbon electrodes optimization, several

challenges to overcome are the facile synthetic routes and the pending fundamental understanding of the energy storage mechanisms. Therefore, the aim of the present dissertation is to develop novel synthetic methods for (nitrogen-doped) porous carbon materials with superior performance, and to reveal a deeper understanding of some open questions regarding energy storage mechanisms of supercapacitors.

In chapter 3, a novel synthetic method towards advanced carbon electrode materials for traditional EDLCs will be introduced with precisely tunable porosity. The electrode materials give rise to superior EDLC performance in all kinds of electrolytes. Even more importantly, the controversial energy storage mechanism of EDLCs employing IL electrolytes is investigated by employing a series of hierarchical salt-templated model carbons as electrodes. The materials show a promising potential for large-scale production in terms of the admirable performance as well as the facile and low-cost synthetic route. The results will not only allow to conclude on the relations between the porosity and ion transport dynamics, but also deliver the deeper insights into the new energy storage mechanism of IL-based EDLCs.

Chapter 4 is reporting synthesis of nitrogen-rich carbon electrode materials as anodes for NICs and the study of their sodium storage mechanism, in order to promote the relatively inferior rate capability of NIC anodes, which is the biggest challenge in this area. Firstly, Free-standing fibrous nitrogen-doped carbon materials (HAT-CNFs) are synthesized by electrospinning with superior capacity and desirable rate capability. This work also provides a systematic study of the sodium storage mechanism in nitrogen-doped carbons. Afterwards, for further optimization of the architecture, a composite material composed of nitrogen-rich carbon nanoparticles embedded in conductive mesoporous carbon matrix (HAT550@ZTC) is fabricated. The composite material stands out by a higher nitrogen content and a better rate capability than that of the HAT-CNFs. Full-cell

devices of NIC employing HAT-CNFs and HAT550@ZTC as anodes and salt-templated carbons as the cathode provide remarkable energy and power density. Their energy density significantly prevails that of common EDLCs while maintaining the high power density and long cycle life.

3.   Carbon Electrodes and Energy Storage Mechanism of EDLCs

As mentioned in section 2.2, ordered mesoporous-microporous carbon materials (OMMCs) are one of the ideal electrode materials for EDLCs. However, there is a lack of facile synthetic approaches to synthesize OMMCs with controllable size, geometry, ratio, and connectivity of the pores in each single and between the different pore systems. Typically, OMMCs are accessible via hard-/soft-templating approaches for mesopore formation, followed by subsequent introduction of smaller pores by etching silica co-templates,[99] chemical activation,[33, 100-101] or metal extraction from mesoporous carbides.[67-69, 102] Especially the former methods can result in bottleneck- or torturous pores with broad size distribution, and the size and volume of micropores can hardly be regulated. This limits the high power performance of EDLCs based on such materials and hinders a systematic understanding of the synergistic effects of ordered mesopores and micropores in charge storage. Furthermore, silica etching, chemical activation, or high temperature chlorine treatment of carbides are all dangerous and toxic processes, and a more facile route which minimizes use of such tools for synthesizing OMMCs with precise control over the pore structure in both systems over a wide range is still required. Recently, eutectic salt mixtures composed of $ZnCl_2$ and other

3. Carbon Electrodes and Energy Storage Mechanism of EDLCs

chlorides were found to be suitable as templates to develop micro- or small mesopores in carbons. This method is known as salt-templating.[103-104] Compared to other strategies for generating micropores, such as activation or metal extraction from carbides, salt-templating eliminates the need for harsh conditions either by evaporating salts during carbonization or removing salts with water, which could then be used repeatedly. In consequence, this method is more sustainable, more environmentally-friendly, and potentially favorable to large scale production. Furthermore, the pore size can be regulated by using different salt mixtures (including $LiCl/ZnCl_2$, $NaCl/ZnCl_2$, or $KCl/ZnCl_2$) and by adjusting the component ratios and the amount of salt in relation to the carbon precursor.[103] However, mesopores generated by salt-templating remain disordered often with a wide size distribution. Therefore, in section 3.1, a novel synthetic method for OMMCs with tunable porosity is put forward, which combines hard-templating and salt-templating approach. Their applications in EDLCs with different electrolytes and the detailed insights into fundamental structure-performance relationships are discussed.

Besides, ILs display promising alternatives to the established solvent-based systems due to their wide operation voltage. An issue of such electrolytes, however, is that they tend to lower the power density of EDLCs. Typically, ion transport in ILs is slow in the bulk and could be even slower in carbon nanopores, leading to sluggish charging dynamics and lowered power density. Resolving these issues necessitates the fundamental understanding of transport dynamics in nanopores filled with ILs. For example, while most studies demonstrate better IL dynamics in larger pores,[105-107] molecular simulation disclosed an ultrahigh transport coefficient in charged micropores as well.[108] The ion dynamics also depend on the surface chemistry where both ionophobic carbon micropores and hydrophobic silica mesopores provide surprisingly high migration coefficients of IL ions.[109-111] Molecular dynamics simulation has revealed the dynamic heterogeneity of IL ions

confined inside uncharged mesopores where the dynamics slow down appreciably as the ions approach the pore walls,[112-114] as well as the great variation of the ion occupancy (total ion density) inside pores with different charging rates.[115] These works attracted much attention and have contributed significantly to the progress toward the elucidation of how the size, surface chemistry, charging state, ion-packing density,[116] and other physicochemical properties of the pores, affect the charge storage mechanism and charge transport dynamics in IL-filled supercapacitors. However, the nanopores in all these theoretic studies are monodisperse in pore size without hierarchy, while hierarchical pore structure with both micro- and mesopores have been proven experimentally to provide efficient ion transport for a high power density while maintaining the high energy density.[102, 117-119] There is still a lack of systematic studies and comprehensive interpretation of the dynamics of electrolyte ions in such complex electrode structures during the charging/discharging process. Understanding requires a combination of computational simulation and experiments, whereas the inadequate characterization of the intricate structure of hierarchical porous carbons without long-range order poses a significant challenge to the modelling and thus the simulation.[120] On the other side, the great difficulty in fabricating nearly ideal carbon models with well-defined hierarchical porosity as well as precisely controlling their pore structures impedes an experimental probing of the sophisticated hierarchical pore structure-property relationships. From the experimental and material perspective, heteroatom (especially nitrogen) doping of the carbon atom framework has been acknowledged as another efficient approach to improve both the capacitance and rate capability of supercapacitors.[121-122] Nevertheless, all the above fundamental research on charge storage mechanisms has been devoted exclusively to pure carbon materials. A deep comprehension of a potential change of mechanisms after nitrogen doping remains missing.

3. Carbon Electrodes and Energy Storage Mechanism of EDLCs

Numerous pioneering experimental and theoretical studies have been devoted to explore the underlying physics for IL charge storage under equilibrium conditions in carbon nanopores, which have led to an improved understanding of the molecular mechanisms. For instance, powerful techniques such as computer simulations,[123] electrochemical quartz crystal microbalance,[124-125] nuclear magnetic resonance (NMR) spectroscopy,[7] and infrared spectroelectrochemical techniques[126] have provided molecular information about the dynamic charge storage, where the ion exchange (swapping of co-ions for counter-ions) seems to play a vital role.[57, 127] Great efforts have been devoted to investigating the dependence of capacitance on the pore size for an ionic liquid electrolyte, especially the anomalous increase of capacitance when the pore size decreases to the ion size.[128-132] Using molecular dynamics simulations, the capacitance is found to depend on the applied voltage as well, where the capacitance reaches a maximum when all co-ions are expelled from the pores.[123] These reports emphasize the significance of the charging process, applied voltage, pore sizes, ion-wall/ion-ion interactions, and physico-chemical properties of the IL, just to name a few. Up to now, the mechanisms for charge storage revealed in these studies neglect possible conformation variations and phase changes in the bulk of the rather large IL ions during charging/discharging.   Simulation studies only employ coarse-grained, rigid models of IL ions, and experimental studies have not taken the influence of such structural changes into consideration, although they are very likely to occur as a function of the electric potential. A limited number of simulation studies have revealed that the ion-wall interactions can significantly affect the ordering of IL ions.[108, 113] Nevertheless, no experimental results confirming this prediction have been reported, and its importance for the energy storage mechanism as well as the origin remains ambiguous.

Thus, section 3.2 aims at providing detailed insights into the influence of the carbon pore structure and heteroatom doping on the energy storage mechanism in IL-

based EDLCs. The relationship between hierarchical pore structure/surface functionalization and ion dynamics is revealed. More importantly, ordering transitions in the bulk of the IL confined in the carbon mesopores is unclosed to contribute to the actual energy storage mechanism for IL-based supercapacitors.

3.1.   Combined hard-salt-templating synthesis of ordered mesoporous carbons with high micropore content as electrode materials for EDLCs

A combined synthetic approach towards OMMCs is put forward, which employs ordered mesoporous silica SBA-15 hard-template and $ZnCl_2$ salt-template as porogens for ordered mesopores and narrow micropores, respectively. Resulting ordered mesoporous hard-salt-templated carbons (OM-HSTCs) offer high specific surface area and total pore volumes. More importantly, the ratio of micropores to ordered mesopores and their respective sizes can be regulated by adjusting the amount of the salt template. Owing to their high surface area and efficient electrolyte transport in the hierarchical pore system, the OM-HSTCs show high specific capacitance and excellent rate capability as electrode materials in EDLCs with aqueous, organic, and IL electrolytes. Detailed insights into fundamental structure-performance relationships are achieved by changing the structural parameters and by comparison with purely microporous or purely mesoporous reference carbons.

3.1.1.   Synthesis and characterization of OMMCs

OM-HSTC is prepared by employing the SBA-15 hard-template and $ZnCl_2$ salt-template as porogens for ordered mesopores and micropores, respectively (**Scheme 3.1**). An aqueous solution containing sucrose as a renewable carbon precursor and $ZnCl_2$ is infiltrated into the mesopores of SBA-15 and the sucrose is polycondensed within the $ZnCl_2$ inside. The salt-template is evaporated during carbonization at 900 ℃, leading to th e formation of a microporous material (micropore volume $0.17\ cm^3\ g^{-1}$) with a notable contribution of mesopores

3. Carbon Electrodes and Energy Storage Mechanism of EDLCs

(mesopore volume ~0.26 cm^3 g^{-1}) (**Figure 3.1**). Finally, OM-HSTC is obtained by the removal of the SBA-15. Although a separate step for the removal of the hard-template is still necessary, this synthesis scheme stands out due to the combination of carbonization and micropore formation by a potentially reusable template without additional activation thus leading to a high yield of carbon from a renewable precursor.

Scheme 3.1. Preparation of ordered mesoporous hard-salt-templated carbon (OM-HSTC).
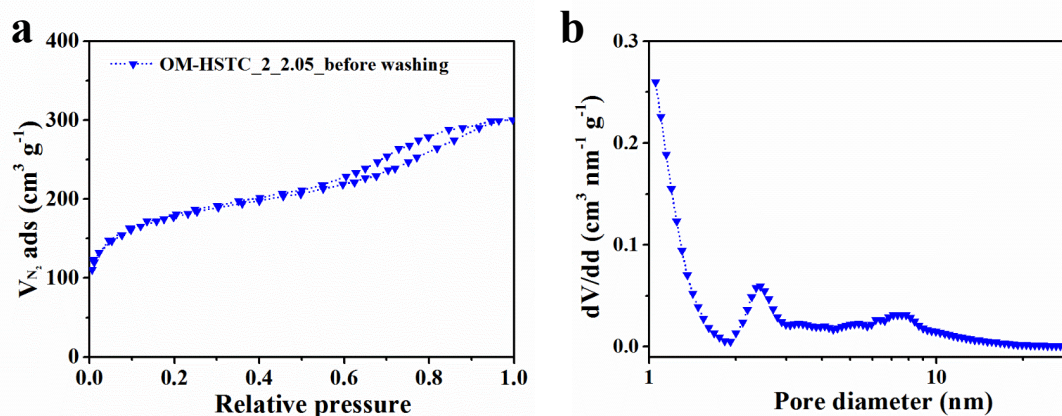
Figure 3.1. (a) N_2 physisorption (-196 ℃) isotherms with corresponding (b) differential QSDFT pore size distributions of carbonized OM-HSTC_2_2.05 prior to removal of the hard-template with NaOH.

A series of OM-HSTCs is prepared by varying the amount of $ZnCl_2$ to explore possible variations of the pore structure. The final product is named as OM-HSTC_X_Y, where X and Y represent the mass ratio of $ZnCl_2$/sucrose and sucrose/SBA-15, respectively (**Appendix, Table 6.2**). In small-angle X-ray scattering (SAXS) measurements (**Figure 3.2**a), OM-HTC_0_2.05, OM-HSTC_1_2.05, and OM-HSTC_2_2.05 all show a well-resolved peak assigned to (100) diffractions of the 2-d hexagonal space group (p6mm), which locate at 2θ = 1.08, 1.04 and 0.96°, respectively. This indicates a larger distance between the centers of the carbon nanorods with increasing amounts of $ZnCl_2$. This is likely because $ZnCl2$ (until its evaporation) stabilizes the hard-template SBA-15 and provides resistance against shrinkage of during high-temperature treatment, a known effect for sol-gel derived silicas. No diffraction peak at low angle is present for HSTC_3_2.05, suggesting the absence of mesopore ordering because the infiltration solution contains too much of the salt and too little carbon-forming sucrose to stabilize a continuous carbonaceous system. As expected, the purely salt-templated sample STC_2 does not have ordered mesopores, either.
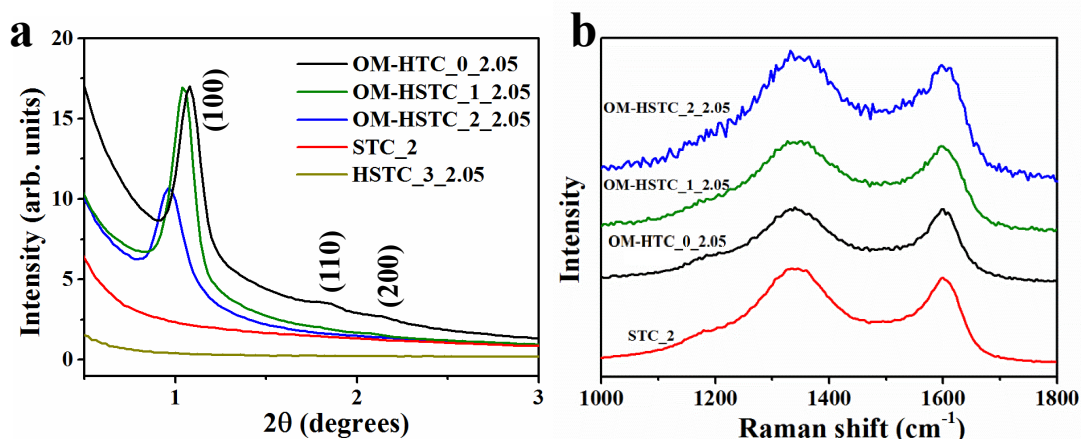
Figure 3.2. (a) SAXS patterns and (b) Raman spectra of OM-HSTCs and the OM-HTC_0_2.05/STC_2 references.

In the Raman spectra (**Figure 3.2**b and **Figure 3.3**), the D-band near 1340 cm^{-1} originates from the breathing modes of the six-fold sp^2-hybridized carbon rings in the presence of defects and disorder.[133-134] The width of the D-band reflects the degree of structural ordering and size distribution of sp^2 rings (i.e., 5-, 6-, 7-, and 8-fold rings). The wide (154-159 cm^{-1} for the OM-HSTCs) D-bands (**Table 3.1**) in all samples reveal the existence of abundant disordered sections as it is typical for highly microporous carbons.[133] The G-band near 1580 cm^{-1} is caused by bond stretching of sp^2 carbon in either rings or chains. The peak height ratio of the D- and G-band (I_D/I_G) is proportional to the amount of six-membered sp^2 carbon rings, which is commonly employed to evaluate the level of carbon ordering in porous carbons.[133-135] The I_D/I_G value (**Table 3.1**) shows a slight rise with the increase of salt-templates (the values of OM-HTC_0_2.05, OM-HSTC_1_2.05, OM-HSTC_2_2.05, and STC_2 equal 1.11, 1.19, 1.24, and 1.28, respectively). This indicates that adding the salt-template improves the degree of aromatization and thereby the number of six-membered rings at the same carbonization temperature. This, in turn, causes a slightly higher electric conductivity for the OM-HSTCs obtained with a higher amount of ZnCl$_2$.
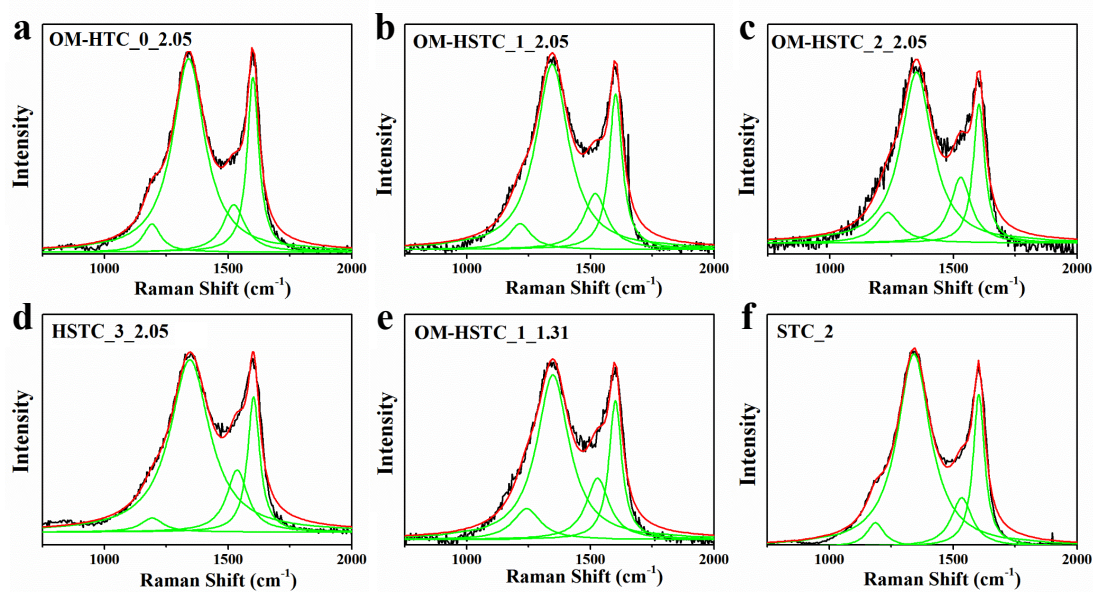
Figure 3.3. Raman spectra with the corresponding fitting curves of (a) OM-HTC_0_2.05, (b) OM-HSTC_1_2.05, (c) OM-HSTC_2_2.05, (d) HSTC_3_2.05, (e) OM-HSTC_1_1.31, and (f) STC_2.

Table 3.1. BET SSA, total pore volume (V_t), micropore volume (V_{mic}), and ultramicropore volume ($V_{ultramicro}$, calculated from CO_2 physisorption), I_D/I_G ratio, and full-width at half maximum (FWHM) of the D-band of the carbon materials obtained by Raman spectroscopy and N_2 physisorption at -196 ℃.

Sample	SSA ($m^2\,g^{-1}$)	V_t ($cm^3\,g^{-1}$)	V_{mic} ($cm^3\,g^{-1}$)	$V_{ultramicro}$ ($cm^3\,g^{-1}$)	I_D/I_G	FWHM of D band (cm^{-1})
OM-HSTC_2_2.05	2649	2.22	0.53	0.15	1.24	154
OM-HSTC_1_2.05	1439	1.43	0.24	0.18	1.19	159
OM-HSTC_1_1.31	1460	1.99	0.16	0.18	1.19	158
HSTC_3_2.05	2131	1.80	0.51	n.d.	1.27	194
OM-HTC_0_2.05	1263	1.26	0.11	0.14	1.11	158
STC_2	1557	0.85	0.47	0.15	1.28	161

Thermogravimetric analysis (TGA) of the materials is carried out under air atmosphere (**Figure 3.4**). OM-HTC_0_2.05 and OM-HSTC_2_2.05 show a completely burn off indicating the absence of any residual template in these samples. The other hard-templated carbon samples show a small amount of minor residual mass (less

than 5 wt%) above 600 ℃, verifying the nearly complete removal of $ZnCl_2$ and SBA-15 after carbonization and washing with NaOH. The onset temperatures of the decomposition of OM-HSTCs is larger than for OM-HTC_0_2.05, which can be ascribed to their higher degree of aromatization as revealed by Raman spectroscopy. The STC_2 carbon obtained by salt-templating without hard-template shows a higher residual mass and therefore the presence of zinc species in this sample, presumably trapped in small or isolated pores, cannot be ruled out. In case of OM-HSTC_2_2.05, on the contrary, ordered mesopores are present after carbonization which allow for efficient removal of zinc species from the carbon framework (**Figure 3.1**). In accordance, the residual zinc in this material detected by electron dispersive X-ray spectroscopy (EDX) after washing is below 1 wt% in both SEM and TEM mode.
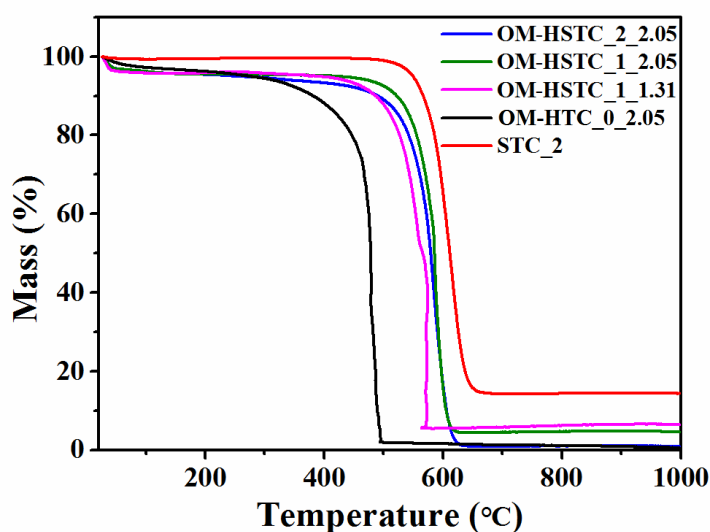
Figure 3.4. TGA of OM-HSTCs and the CMK-3/STC references measured under air with a heating rate of 10 ℃ min^{-1}.

N_2 (-196 ℃) and CO_2 (0 ℃) physisorption experiments are carried out to analyze the OM-HSTCs pore structures (**Figure 3.5, Figure 3.6, Table 3.1**). OM-HTC_0_2.05, OM-HSTC_1_2.05 and OM-HSTC_2_2.05 exhibit type IV(a) isotherms with a continuous slope above a relative pressure of 0.2, and a narrow hysteresis loop with near-parallel shape in the relative pressure range between 0.4 and 0.9 (**Figure 3.5**a).

3. Carbon Electrodes and Energy Storage Mechanism of EDLCs

These data support the existence of well-defined mesopores in these carbons. To study the transformation of pore structure from CMK-3 to OM-HSTC_1_2.05 and OM-HSTC_2_2.05, the PSD is further analyzed by recording low-pressure isotherms (**Figure 3.6**) and applying the quenched-solid density functional theory (QSDFT) for N_2 adsorbed on carbon with slit/cylindrical pore shape (**Figure 3.5**b). For all OM-HSTC samples, the amount of micropores (with diameters mainly around 0.9-1.0 nm) is drastically increased after the addition of $ZnCl_2$ in comparison to OM-HTC_0_2.05. Due to its small micropore content (0.11 $cm^3 \, g^{-1}$), OM-HTC_0_2.05 has the lowest specific surface area (SSA) of 1263 $m^2 \, g^{-1}$, while the larger mesopores contribute only little to the surface area. With increasing the salt loading, SSAs and micropore volumes increase significantly to 2649 $m^2 \, g^{-1}$ and 0.53 $cm^3 \, g^{-1}$, respectively, in OM-HSTC_2_2.05. OM-HSTC_2_2.05 and STC_2 contain in addition small mesopores with an average diameter of 2.4 nm and 3.2 nm, respectively. These pores likely originate from the formation of larger clusters of salt-templates and are absent in OM-HSTC_1_2.05 prepared with a lower ratio of $ZnCl_2$/sucrose. The cumulative PSD plots (**Figure 3.5**c) indicate that the micropores only contribute a small fraction of the total pore volume in the OM-HSTCs. The STC_2 reference shows a type I(b) isotherm,[29] indicating its typical structure containing micropores centered at 0.9 nm with small amount of narrow mesopores. The disordered HSTC_3_2.05 has a high surface area (2131 $m^2 \, g^{-1}$) and micropore volume (0.51 $cm^3 \, g^{-1}$) but a broader hysteresis loop and a less defined pore size than the OM-HSTCs (**Figure 3.7**).
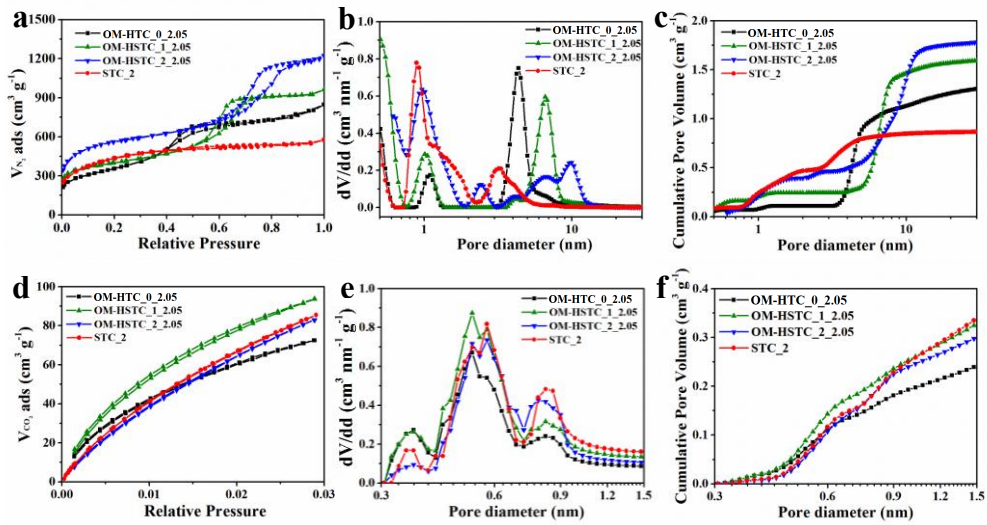
Figure 3.5. (a) N_2 physisorption (at -196 ℃) isotherms with corresponding (b) differential and (c) cumulative QSDFT PSDs as well as (d) CO_2 physisorption (at 0 ℃) isotherms with corresponding (e) differential and (f) cumulative non-local density functional theory PSDs of OM-HSTCs and the OM-HTC_0_2.05/STC_2 references.
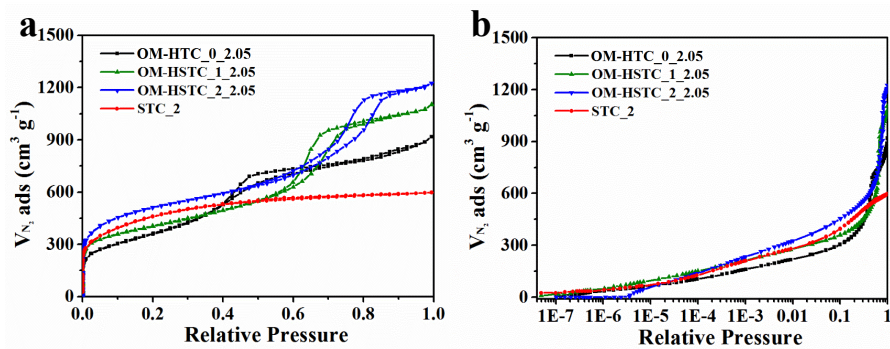
Figure 3.6. (a) Linear (b) semi-logarithmic plots of low pressure N_2 physisorption isotherms (at -196 ℃) of OM -HSTCs and the OM-HTC_0_2.05/STC references.
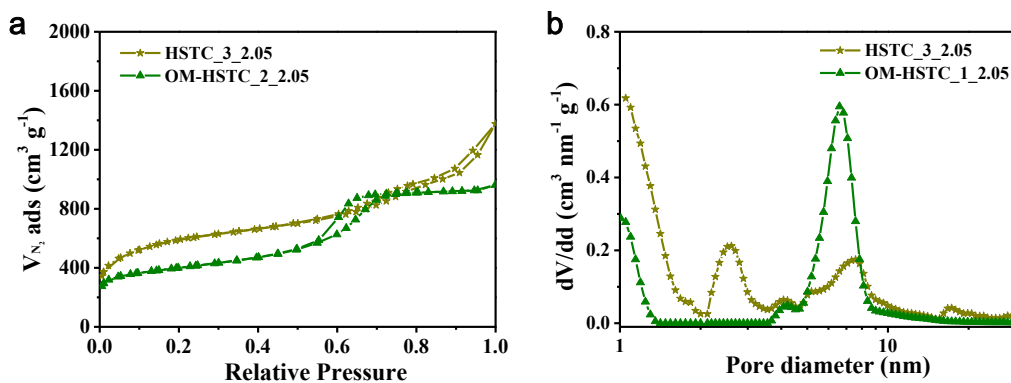
Figure 3.7. (a) N_2 physisorption (-196 ℃) isotherm with corresponding (b) differential QSDFT pore size distribution of disordered HSTC_3_2.05, in comparison with those of OM-HSTC_1_2.05.

3. Carbon Electrodes and Energy Storage Mechanism of EDLCs

The distributions of pores with diameters of 1.5 nm and below have been further analyzed by non-local density functional theory (NLDFT) analysis of CO_2 physisorption measurements (**Figure 3.5**d-f). All samples contain even more narrow micropores with a main diameter of ~0.6 nm in addition to the micropores centered at 0.9-1.0 nm detected by N_2 physisorption. A smaller $ZnCl_2$/sucrose ratio leads to a larger volume of ultramicropores,[29] that is, pores with diameters of 0.7 nm and below. Hence, OM-HSTC_1_2.05 shows the highest ultramicropore volume among all samples. OM-HSTC_2_2.05 and STC_2 have a higher total micropore volume but smaller ultramicropore volume. This shows that the precise control over the micropore size (a general advantage of salt-templated carbons) is not perturbed by the presence of an additional hard-template.

With the increase of $ZnCl_2$ content, the average mesopore diameter increases from 4.4 nm (OM-HTC_0_2.05) to 6.6 nm (OM-HSTC_1_2.05) and to 9.9 nm (OM-HSTC_2_2.05) accompanied by a broader distribution. This can be ascribed (in addition to the less pronounced shrinking discussed above) to formation of a surface layer of liquid $ZnCl_2$ on the surface of the nanochannel pore walls of SBA-15 (**Scheme 3.2**). The positively charged-Lewis acidic Zn^{2+} ions are prone to coordinated by oxygen atoms on the SBA-15 pore walls during the impregnation step. Therefore, the salt-template distributes partly along the walls of the channel and partly inside the carbon precursor into the channels of the silica. This causes the growth of the mesopores between the cylindrical carbon rods after the removal of SBA-15, that is, the mesopore size of the carbon is a sum of the size of the pore walls of SBA-15 and two times the thickness of the salt layer. The precise control of the mesopore sizes can be used to tailor the size of ordered mesopores at a given hard-template and is a unique feature of the salt-templating approach if compared to previously reported synthesis methods for OMMCs.

3. Carbon Electrodes and Energy Storage Mechanism of EDLCs
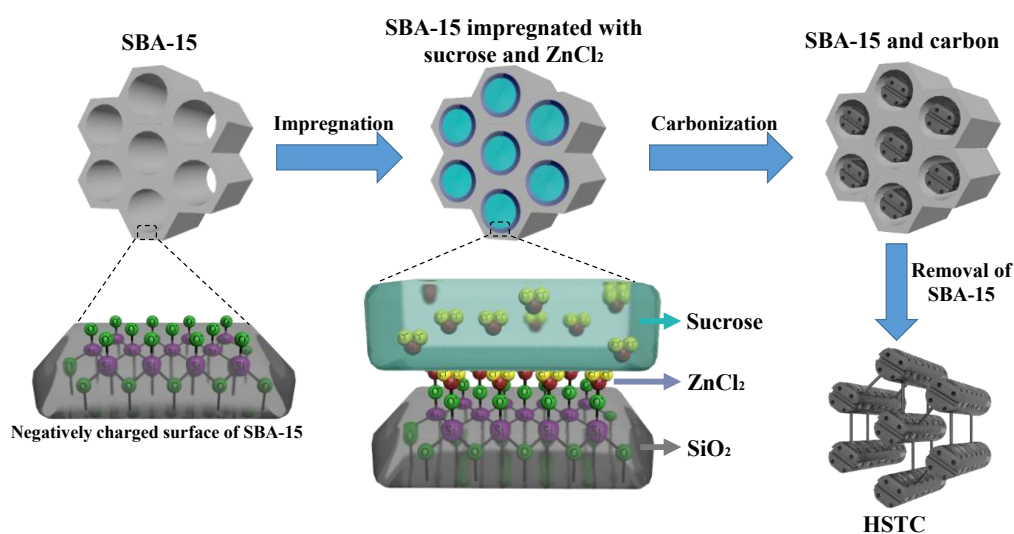
Scheme 3.2. Possible mechanism of enlargement of mesopore size caused by salt templating.

Scanning electron microscopy (SEM) shows that OM-HTC_0_2.05 (**Figure 3.8**a) and OM-HSTC samples (**Figure 3.8**c,e) have the typical particle morphology of hexagonally ordered mesoporous materials like the SBA-15 template. In line with SAXS and physisorption measurements, transmission electron microscopy (TEM) images (**Figure 3.8**b,d,f) further evidence the ordered mesoporous structure of all hard-templated samples. The mean distances between the carbon rods equal 4.9, 7.6, and 8.8 nm for OM-HTC_0_2.05, OM-HSTC_1_2.05, and OM-HSTC_2_2.05, respectively. This enlargement of mesopores with increasing content of salt-template is in good agreement with SAXS and physisorption experiments.
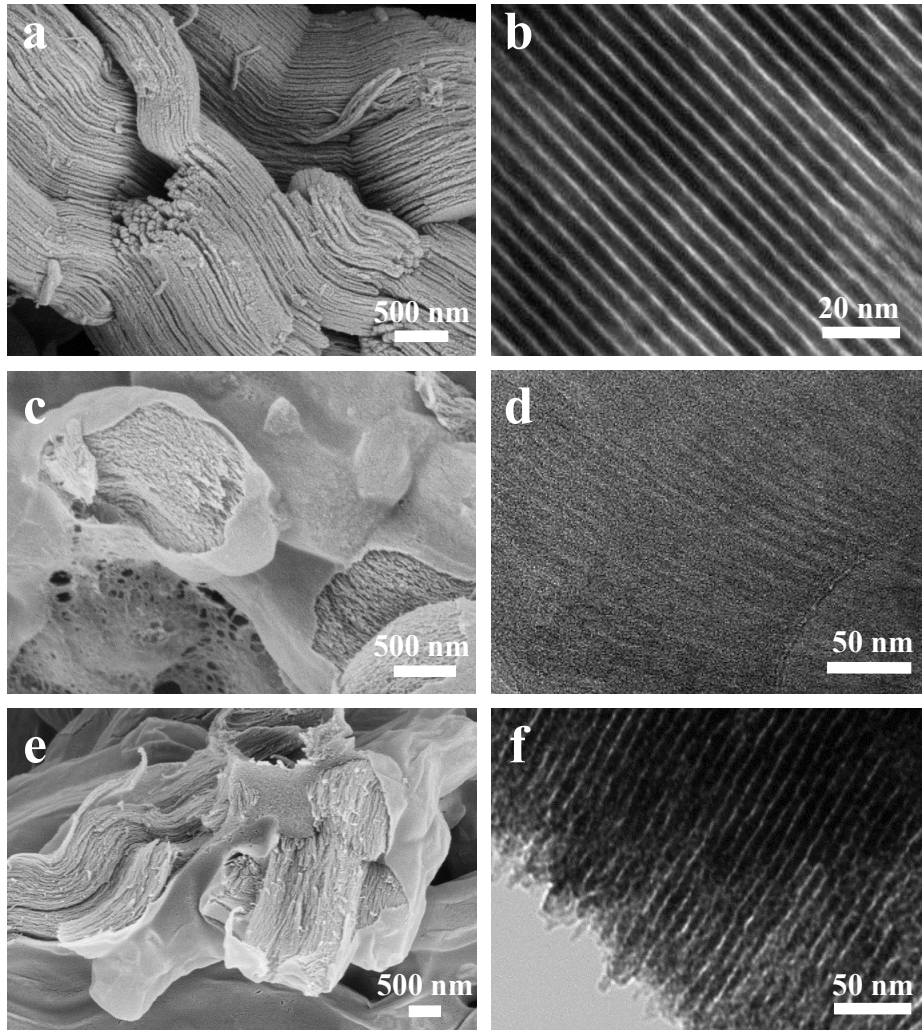
Figure 3.8. SEM and TEM images of (a, b) OM-HTC_0_2.05, (c, d) OM-HSTC_1_2.05, (e, f) OM-HSTC_2_2.05.

A microporous shell is present around the individual particles in both OM-HSTC_1_2.05 and OM-HSTC_2_2.05 (**Figure 3.8**c,e), which partly encompasses the ordered carbon rods. OM-HSTC particles thus exhibit a core-shell structure built up by an ordered mesoporous and microporous core with a purely microporous shell. This may be caused by an excess of salt/ precursor mixture surpassing the pore volume of SBA-15 templates. As OM-HTC_0_2.05 without shell is synthesized with the exact amount of sucrose to fill the pore volume of SBA-15, the mesopores are potentially overfilled with additional $ZnCl_2$. As a result, in the case of OM-HSTCs, a certain amount of the mixed precursor remains outside the SBA-15 particles after

impregnation, which turns into the microporous shell after carbonization. In contrast to the ordered materials, STC_2 presents a rather disordered and macroporous morphology without regular particle architecture (**Figure 3.9**).
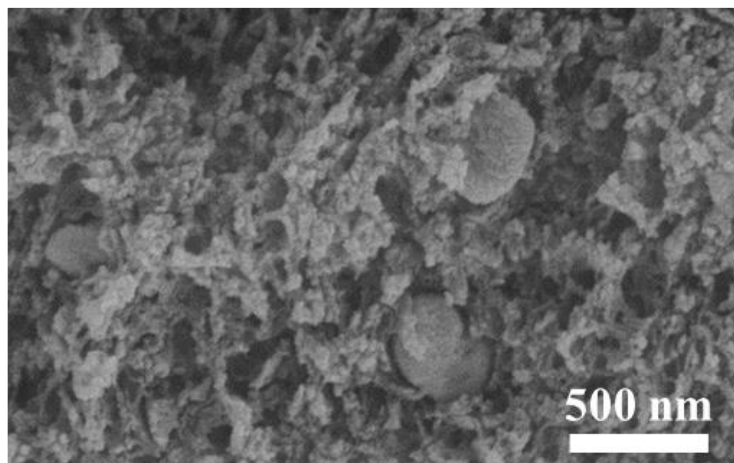
Figure 3.9. SEM image of STC_2.

3.1.2.   EDLC performance in different electrolytes

To establish structure-performance relationships of OM-HSTCS for electrochemical energy storage with supercapacitors, the samples are fabricated into electrodes and characterized with cyclic voltammetry (CV) tests, galvanostatic charging/discharging with potential limitation (GCPL), and electrochemical impedance spectroscopy (EIS) in a common organic electrolyte (1 M tetraethylammonium tetrafluoroborate in acetonitrile ($TEABF_4$/AN)), a typical aqueous electrolyte (1 M Na_2SO_4 in H_2O), and solvent-free ionic liquid (1-Ethyl-3-methylimidazolium tetrafluoroborate ($EMImBF_4$)).

In $TEABF_4$/AN, OM-HSTCs present rectangle-like CV curves (0-2.5 V) without an obvious distortion even at a scan rate as high as 500 mV s^{-1}, indicating pronouncedly capacitive behavior with a high rate capability (**Figure 3.10**a, **Figure 3.11**). The specific capacitance of OM-HSTC_2_2.05 (calculated from GCPL) reaches 133 F g^{-1} at a specific current of 0.1 A g^{-1}, which is 34%, 56%, and 39% higher than that of OM-HSTC_1_2.05 (99 F g^{-1}), OM-HTC_0_2.05 (85 F g^{-1}) and STC (96 F g^{-1}; **Figure 3.10**c). At a specific current of 40 A g^{-1}, the specific capacitance of OM-HSTC_2_2.05 still

reaches 126 F g⁻¹ (about 95% of its initial capacitance). The galvanostatic charging/discharging curves (**Figure 3.10**b) of OM-HSTCs show high symmetry and linear slopes with a small voltage drop of 0.22 V for OM-HSTC_2_2.05. This excellent rate handling ability suggests a very low resistance in the materials. The voltage drops of OM-HTC_0_2.05 and STC_2 are much higher: 0.80 V at 40 A g⁻¹ and 1.41 V at 25 A g⁻¹, respectively, indicating in both cases surface polarization and thereby contact resistance effects.
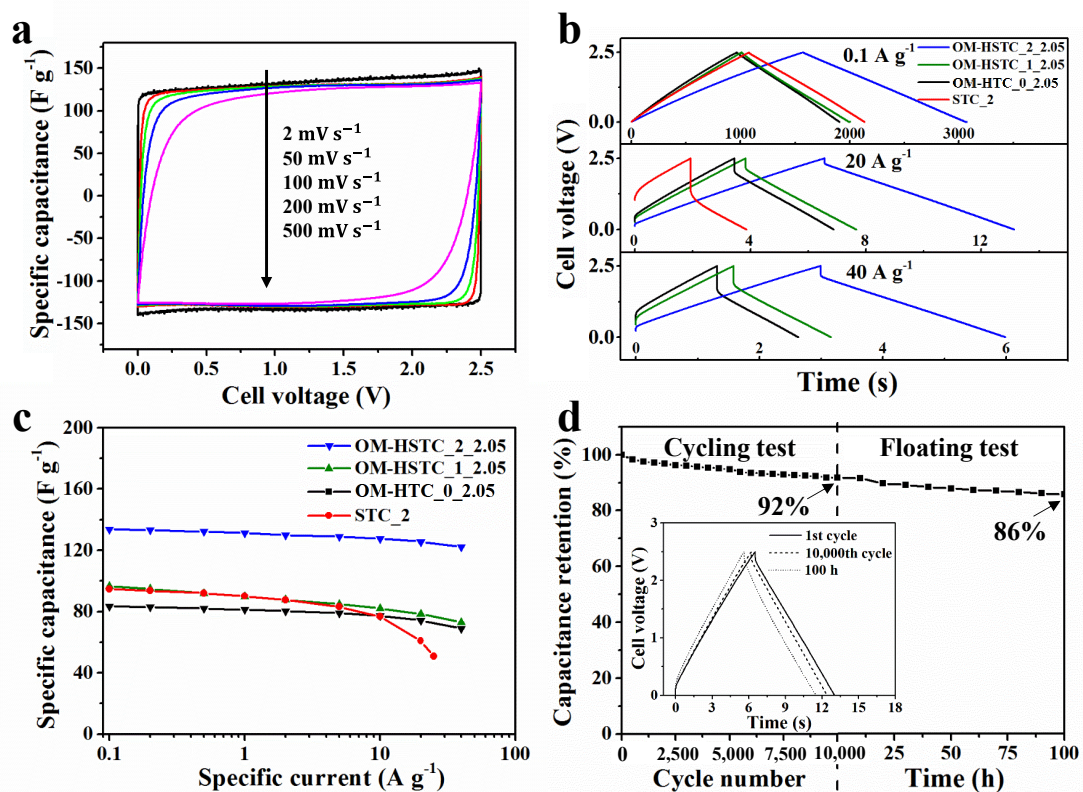
Figure 3.10. (a) Cyclic voltammograms of OM-HSTC_2_2.05 at different scan rates, (b) charge/discharge profiles at different current densities, (c) capacitance retention of different carbon materials with current density increase, and (d) cycle and floating stability of OM-HSTC_2_2.05 at a specific current of 20 A g⁻¹ for 10,000 cycles and 100 h floating at 2.5 V. The inset in (d) shows the charge/discharge profiles of the initial test, after the 10,000th cycling test, and after 100 h floating test. All measurements were conducted in 1 M TEABF₄/AN as electrolyte.
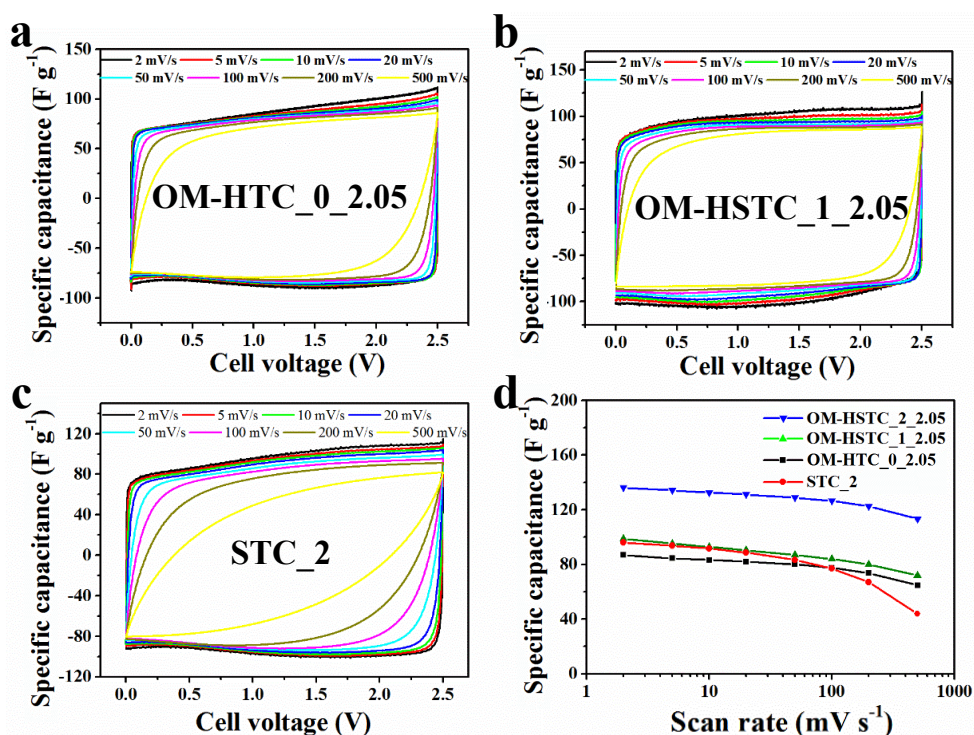
Figure 3.11. Cyclic voltammograms of (a) OM-HTC_0_2.05, (b) OM-HSTC_1_2.05, and (c) STC_2 at different scan rates. (d) Capacitance retention of different carbon materials with scan rates increase. All measurements were conducted in 1 M TEABF$_4$/AN.

Cycling stability tests are performed by charging and discharging (0-2.5 V) at a specific current of 20 A g^{-1} for 10,000 cycles followed by holding the cell voltage of 2.5 V for 100 h (interrupted by cycling at 20 A g^{-1} after every 10 h). OM-HSTC_2_2.05 shows excellent stability with 86% capacitance retention, after continued cycling and voltage holding (**Figure 3.10**d). The 14% capacitance loss might be caused by the large voltage window that leads to some irreversible reactions between the electrolyte and carbon surface groups.

The carbon samples show comparable EDLC performance when tested in 1 M Na$_2$SO$_4$/H$_2$O neutral aqueous electrolyte (**Figure 3.12, Figure 3.13**). CV curves (-0.5 V ~ 0.5 V) of OM-HSTC_2_2.05 (**Figure 3.12**a) exhibit a rectangular shape and GPCL measurements show a specific capacitance of 125 F g^{-1} at 0.1 A g^{-1} (**Figure 3.12**c), considerably exceeding that of OM-HSTC_1_2.05 (95 F g^{-1}), OM-HTC_0_2.05 (77 F g^{-1}) and STC_2 (78 F g^{-1}). At an ultrahigh specific current of 40 A g^{-1}, the specific

3. Carbon Electrodes and Energy Storage Mechanism of EDLCs

capacitance of OM-HSTC_2_2.05 still reaches 117 F g^{-1}. The corresponding GCPL curves are highly symmetric triangle with only a small voltage drop of 0.17 V at 40 A g^{-1} (**Figure 3.12**b). In contrast, OM-HTC_0_2.05 shows a moderate rate capability (67% capacitance remaining, and the purely microporous STC_2 shows the lowest performance (**Figure 3.12**b,c).

Figure 3.12. (a) Cyclic voltammograms of HSTC_2_2.05 at different scan rates, (b) charge/discharge profiles at different specific currents, and (c) capacitance retention of different carbon materials with current density increase. All measurements were conducted in 1 M Na$_2$SO$_4$/H$_2$O electrolyte.
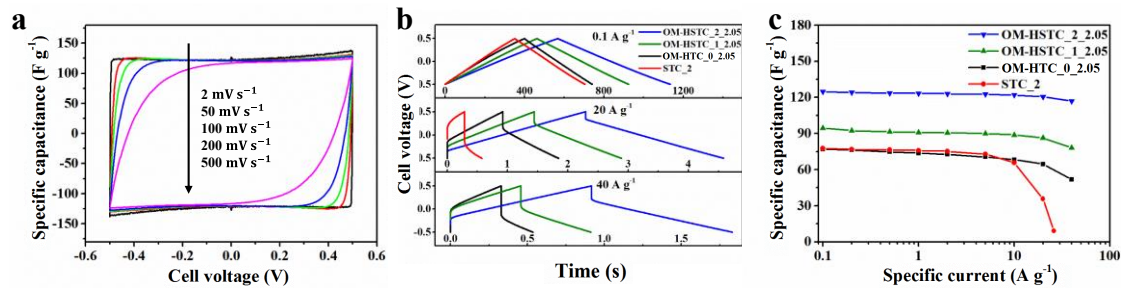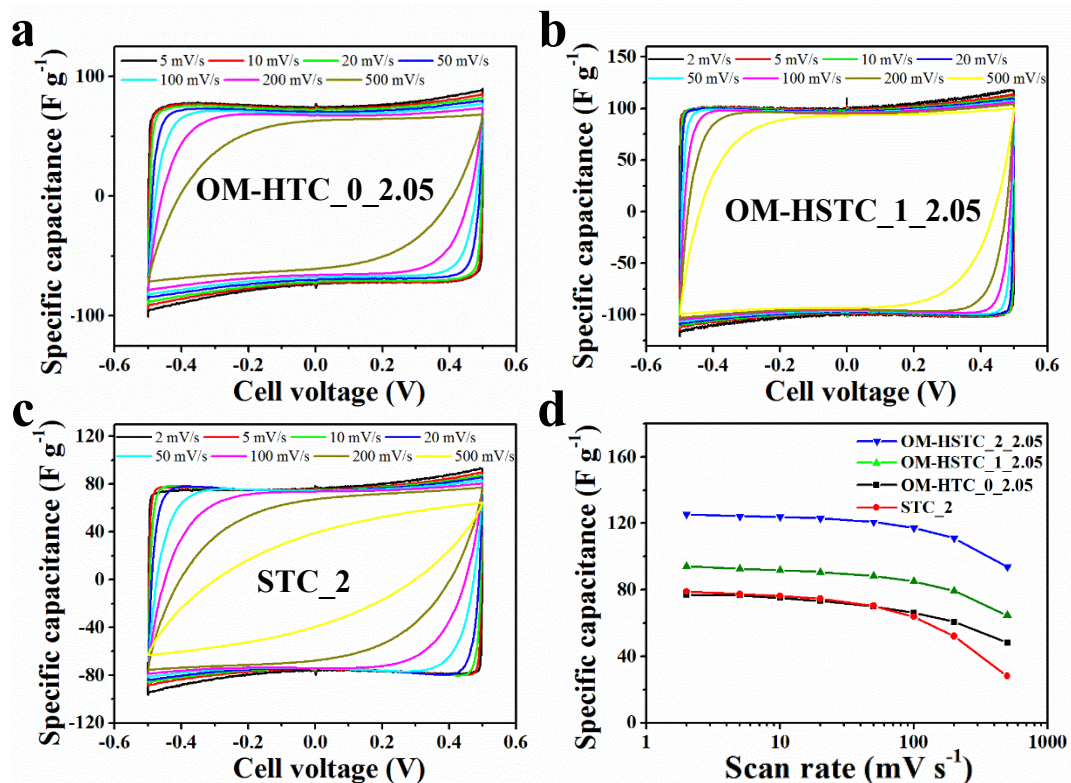

Figure 3.13. Cyclic voltammograms of (a) OM-HTC_0_2.05, (b) OM-HSTC_1_2.05, and (c) STC_2 at different scan rates. (d) Capacitance retention of different carbon materials with scan rates increase. All measurements were conducted in 1 M Na$_2$SO$_4$/H$_2$O.

3. Carbon Electrodes and Energy Storage Mechanism of EDLCs

The EDLC performance shows that the OM-HSTCs provide not only higher specific capacitance, but also a rate capability which is slightly better than that of OM-HTC_0_2.05. The observed excellent capacitance of OM-HSTCs could be attributed to their high specific surface area and micropore volume (**Table 3.1**) which offers many active sites for ion adsorption with optimum size to distort solvation shells and provide close approach of the ions to the pore walls. The increase of salt-templates further enhances these two positive factors by increasing the size of ordered mesopores and the micropore volume, leading to the higher capacitance and rate capability of OM-HSTC_2_2.05 compared to OM-HSTC_1_2.05. The inferior rate capability of STC-2 is attributed to the absence of ordered mesopores as fast transport channels.

To further understand the difference of rate capabilities between the carbon samples, EIS is employed to investigate the impedance behaviors of EDLCs based on different carbon electrode materials (**Figure 3.14**a,c). The frequency responses in organic and aqueous electrolytes (**Figure 3.14**b,d) confirm the excellent rate capability of OM-HSTCs. The capacitances of OM-HSTCs show saturation in organic and aqueous electrolytes at a frequency around ~0.3 Hz, suggesting that near-equilibrium ion adsorption could be achieved within several seconds, which is much faster than that in OM-HTC_0_2.05 and STC_2. Quantified by the frequency f_0 at which the capacitance drops to the half of its maximum value, OM-HSTC_2_2.05 and OM-HSTC_1_2.05 display fast frequency responses with f_0 of 0.85 Hz and 0.73 Hz in organic electrolyte, significantly surpassing that of OM-HTC_0_2.05 (0.46 Hz) and STC_2 (0.14 Hz), indicating the faster charge/discharge rate of hierarchical OM-HSTCs. The frequency responses in the aqueous electrolyte show the same trend. The f_0 of OM-HSTC_2_2.05, OM-HSTC_1_2.05, OM-HTC_0_2.05, and STC_2 equals 0.85 Hz, 0.74 Hz, 0.55 Hz, and 0.21 Hz, respectively. The nearly vertical curves in the low-frequency region of the Nyquist plots in organic (**Figure 3.14**a) and aqueous electrolytes (**Figure 3.14**c) demonstrate the near-ideal capacitive behavior

of all EDLCs. By extrapolating the vertical portion of the curves to the real axis, the equivalent series resistance (R_{ESR}) in organic electrolyte is calculated to be 1.53 Ω cm^{-2} and 1.57 Ω cm^{-2} (1.20 Ω cm^{-2}, and 1.38 Ω cm^{-2} in aqueous electrolyte) for OM-HSTC_2_2.05, and OM-HSTC_1_2.05, respectively. In both electrolytes, this is much lower than for OM-HTC_0_2.05 and STC_2 and consistent with the low voltage drops of OM-HSTCs in GCPL measurements. In the middle-frequency region, the 45° sloped curve known as the Warburg portion is related to the transport of electrolyte ions into the carbon pores. Compared with STC_2, the very short Warburg lengths observed for the OM-HSTCs and OM-HTC_0_2.05 electrode suggest their low resistance for ion transport due to the rapid ion transport through ordered mesopores. Moreover, the thin microporous shells of the OM-HSTCs (**Figure 3.14**b,c) provide a short transport distance for ions to rapidly reach the surface of its inner micropores, while the defects on the shells enable the superb mobility of the ion flux between the ordered mesoporous cores and the outside electrolyte. In the high frequency region, the intercept along the real axis reveals the intrinsic resistances (R_s) of electrode material, electrolyte, current collector, as well as the contact resistances between them. In comparison with OM-HTC_0_2.05, OM-HSTCs present smaller R_s, suggesting the lowest electronic resistance in these electrode materials. Considering the similar ordered mesoporous core in OM-HSTCs and OM-HTC_0_2.05, it can be concluded that the difference in the carbon aromatization by $ZnCl_2$ catalysis is crucial to reduce the electronic resistance in the electrodes. Furthermore, the microporous shell can also have an influence on the resistance.
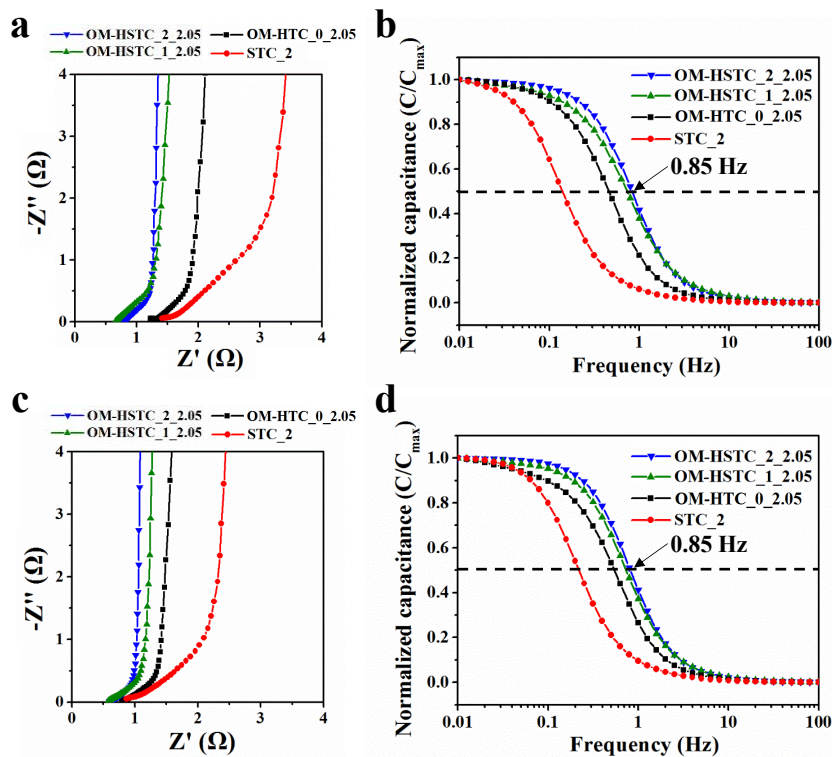
Figure 3.14. Nyquist plots and frequency responses of different carbon materials tested in (a, b) 1 M TEABF$_4$/AN, (c, d) 1 M Na$_2$SO$_4$/H$_2$O.

The mesoporous cores composed of carbon rods in OM-HTC_0_2.05 and OM-HSTCs differ in sizes, amount of micropores inside, and degree of carbon aromatization. For the sake of decoupling these effects from the possible influence of the microporous shell on the electrochemical properties, OM-HSTC without a shell (OM-HSTC_1_1.31) is prepared and compared with OM-HSTC_1_2.05. OM-HSTC_1_1.31 is synthesized by regulating the amount of sucrose and ZnCl$_2$ according to the pore volume of SBA-15 while keeping the same ratio of sucrose to ZnCl$_2$ as in OM-HSTC_1_2.05. In this manner, the micro-/mesoporous cores of OM-HSTC_1_1.31 should be comparable in structure to that of OM-HSTC_1_2.05, that is, the effects of the microporous shell are highlighted by the comparison of their EDLC performance (**Figure 3.15** and **Figure 3.16**). The SEM images of OM-HSTC_1_2.05 (**Figure 3.8**a,c) clearly show a shell around the particles which is absent in OM-HSTC_1_1.31 (**Figures 3.15**b,d); yet, both present the same ordered mesoporous cores as shown by SAXS (**Figure 3.15**e) and TEM images (**Figure 3.8**d, **Figure 3.17**).

3. Carbon Electrodes and Energy Storage Mechanism of EDLCs

From the N_2 and CO_2 physisorption measurements (**Figure 3.15**f and **Figure 3.18**) it can be seen that the major difference between the samples is the larger amount of mesopores in OM-HSTC_1_1.31 than in OM-HSTC_1_2.05 (**Table 3.1**). This is reasonable because the micro-/mesoporous core of OM-HSTC_1_2.05 coexists with the purely microporous shell, whereas OM-HSTC_1_1.31 only contains the core in which the mesopores are located. While the mesopores are similar in size and the SSA is comparable in both samples, a minor difference is the higher amount of micropores in OM-HSTC_1_2.05 because of the microporous shells (**Table 3.1**).
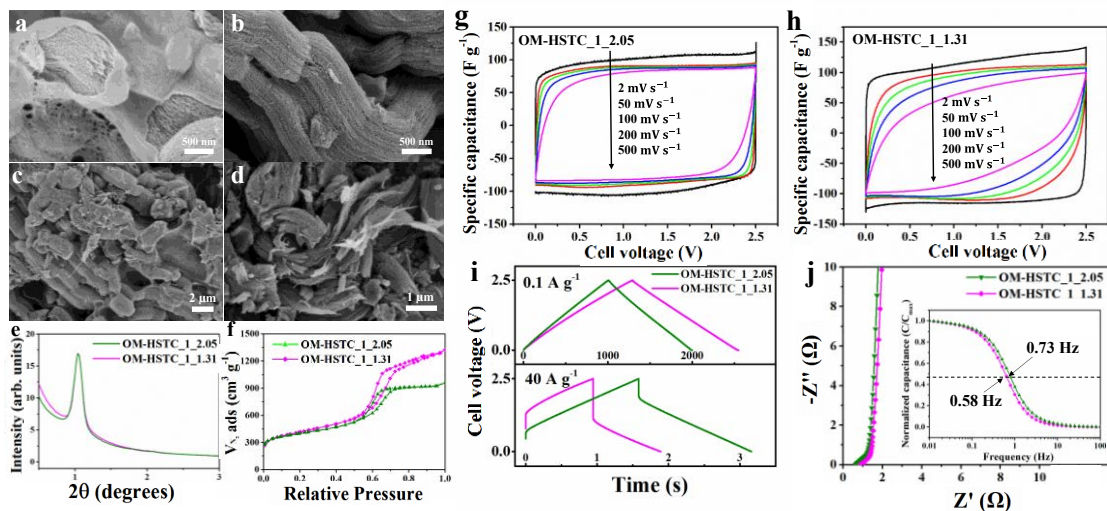
Figure 3.15. (a, b) SEM images of OM-HSTC_1_2.05 and OM-HSTC_1_1.31. (c, d) SEM images of electrodes prepared from OM-HSTC_1_2.05 and OM-HSTC_1_1.31. (e) SAXS patterns, (f) N_2 physisorption (-196 ℃) isotherms, (g, h) Cyclic voltammograms, (i) charge/discharge profiles at different specific currents, and (j) Nyquist plots of OM-HSTC_1_2.05 and OM-HSTC_1_1.31. The inset in (j) shows frequency responses. All electrochemical measurements were conducted in 1 M TEABF$_4$/AN.
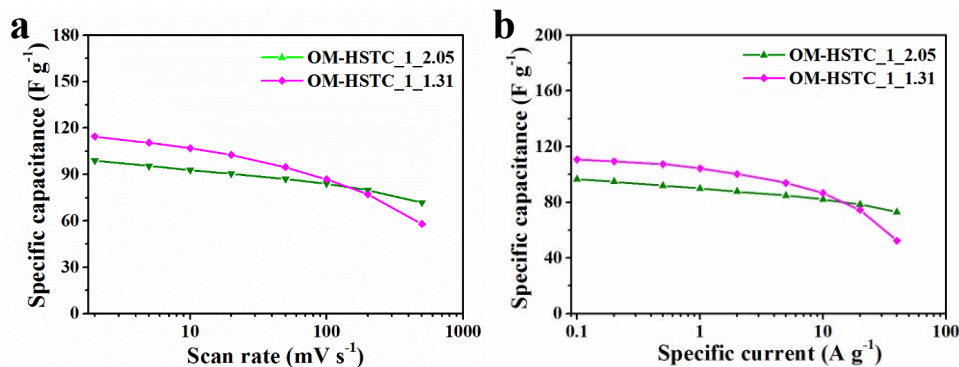
Figure 3.16. Capacitance retention of OM-HSTC_1_2.05 and OM-HSTC_1_1.31 with the increase of (a) scan rates, and (b) specific currents.
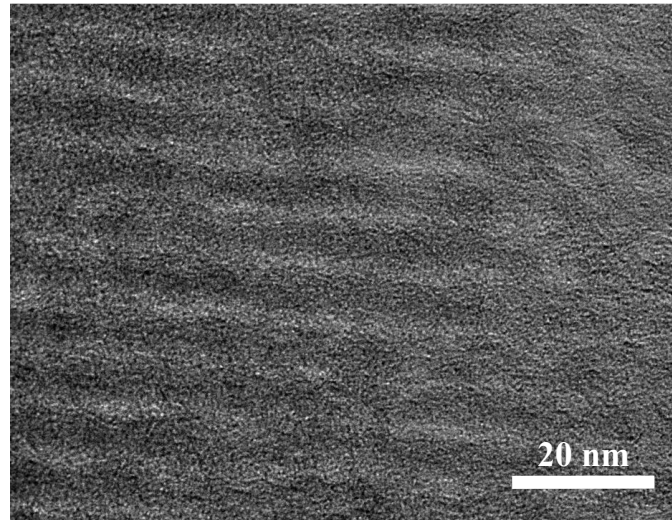
Figure 3.17. TEM image of OM-HSTC_1_1.31.
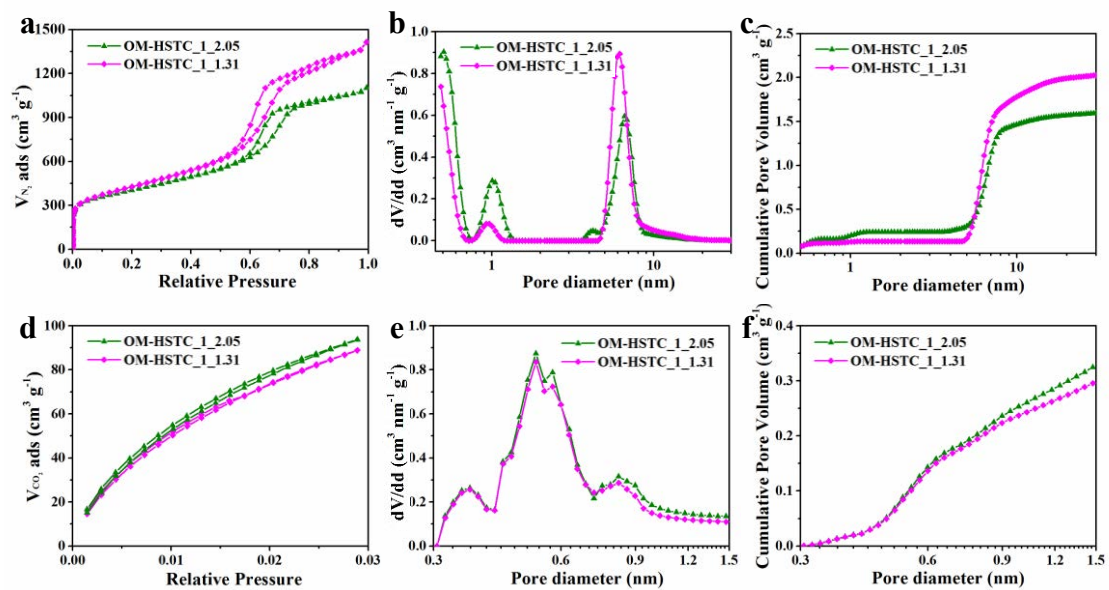
Figure 3.18. (a) Low-pressure N_2 physisorption (-196 ℃) isotherms with correspondin g (b) differential and (c) cumulative QSDFT pore size distributions as well as (d) CO_2 physisorption (0 ℃) isotherms with corresponding (e) differential and (f) cumulative NLDFT pore size distribution pattern of the OM-HSTC_1_2.05 and OM-HSTC_1_1.31.

The CV curves of OM-HSTC_1_1.31- and OM-HSTC_1_2.05-based EDLCs in organic electrolyte (**Figure 3.15**g,h) show typical quasi-rectangular shapes. But for OM-HSTC_1_1.31 without shells, the shape at 500 mV s^{-1} becomes significantly more elliptical as compared to OM-HSTC_1_2.05 indicating the lower rate capability of the

former. In the GCPL curves (**Figure 3.15**i), the voltage drop at 40 A g^{-1} of OM-HSTC_1_1.31 (0.89 V) is more than two times that of OM-HSTC_1_2.05 (0.42 V). According to that, the OM-HSTC_1_2.05 with shell shows lower polarization and thus higher capacitance retention under high power conditions in both CV and GCPL tests (**Figure 3.15**g,h,i). The differences caused by the presence of a microporous shell in the particles are further underlined by EIS (**Figure 3.15**j). The microporous shell around the carbon particles of OM-HSTC_1_2.05 apparently reduces the internal resistance of the EDLCs by facilitating transfer of charged species between the individual carbon particles into the electrodes.

Finally, the ionic liquid (IL) EMImBF$_4$ with a wide voltage window of 0-3.5 V was employed as the electrolyte to test the EDLC performance of OM-HSTC_2_2.05 (**Figure 3.19**). Since the energy storage capacity of an EDLC is proportional to the square of its operating voltage, ionic liquids (at similar capacity) are promising to address the main problem of current EDLCs, which is their low energy density.[136-137] Also in this electrolyte, CV curves show a nearly rectangular shape at different scan rates (5-200 mV s^{-1}). The GCPL curves are nearly symmetrical with small voltage drops at high current densities (0.64 V at 10 A g^{-1}), and the curves in the low-frequency region of Nyquist plots are nearly vertical (**Figures 3.19**a-c). A high specific capacitance of 138 F g^{-1} is obtained from the GCPL curve (**Figure 3.19**b) at 0.1 A g^{-1} in the IL electrolyte (0-3.5 V).

Even more fascinating, in the CV curves, an increase of the cathodic current at 3.0-3.5 V and a small peak at around 2.0 V (disappeared when increasing the scan rate over 50 mV s^{-1}) can always be observed, indicating deviation from the ideal capacitor-like behavior. Such kind of phenomenon also appears in many other literature regarding IL-based supercapacitors.[138-139] But there still lacks a systematic and thorough study of the fundamentals of such effects. Moreover, the capacitance (which corresponds to the charge divided by the voltage) and the voltage in IL electrolytes is higher than that in the aqueous and organic electrolytes,

indicating that more charges must be compressed on the surface of the electrodes on the basis of classical electrical double-layer theory. But the ILs can hardly be compressed as they are solely composed of ions without solvents, which contradicts the electrical double-layer theory. Hence, the study in the next section will focus on the pending energy storage mechanism of IL-based supercapacitors.
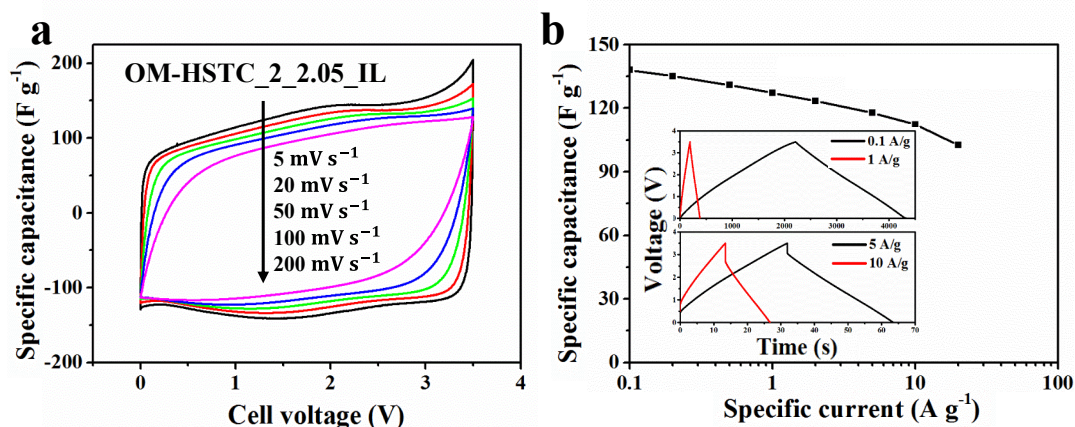
Figure 3.19. EDLC performance of OM-HSTC_2_2.05 tested in the ionic liquid electrolyte EMImBF$_4$. (a) Cyclic voltammograms at different scan rates, (b) capacitance retention with current density increase. The inset in (b) shows the charge/discharge voltage profiles at different specific currents).

The gravimetric and volumetric Ragone plots (**Figure 3.20**) of EDLCs using OM-HSTC_2_2.05 as electrodes show that the symmetric cells provide the highest specific energy of 29 Wh kg^{-1} at a specific power of 78 W kg^{-1}, and still maintain 23 Wh kg^{-1} at a specific power of 27 kW kg^{-1} in TEABF$_4$/AN electrolyte. In the IL electrolyte, the specific energy reaches 59 Wh kg^{-1} at a specific power of 1 kW kg^{-1}, and maintains 25 Wh kg^{-1} when the specific power increases to 18 kW kg^{-1}. This property is attributed to the high content of micropores for ion storage and the ordered mesopores for fast charge transfer, as well as the thin microporous shell for reduced electric resistance. Yet, the low density of the highly mesoporous OM-HSTC electrodes (~0.3 g cm^{-3}) leads to a moderate energy density (<10 Wh L^{-1} and < 20 Wh L^{-1} in organic and IL electrolyte, respectively).
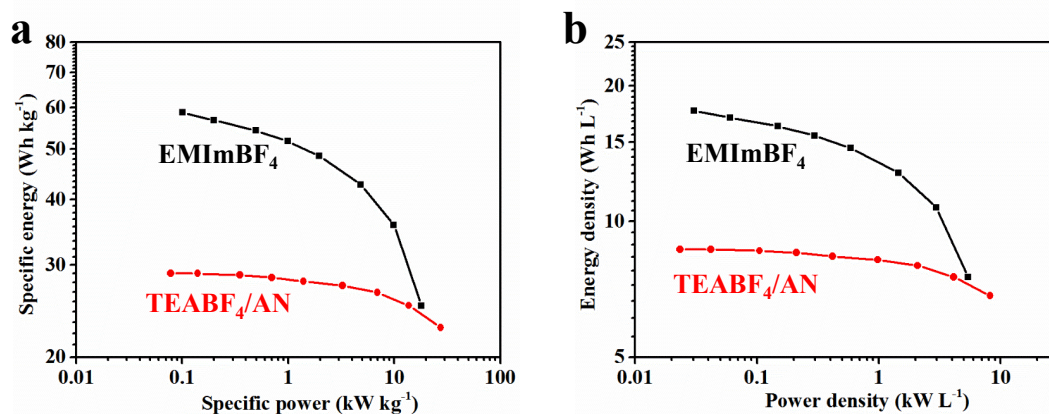
Figure 3.20. Gravimetric and volumetric Ragone plots of EDLCs using HSTC_2_2.05 as electrodes.

In summary, ordered mesoporous carbon with high content of micropores can be synthesized by a novel combined hard/salt-templating method, which is significantly simpler than established methods. Large specific surface area up to 2649 m^2 g^{-1} and high pore volume exceeding 2.2 cm^3 g^{-1} are obtained when applying optimized synthetic conditions. The synthetic process is highly versatile in terms of tailoring the pore morphology, diameter and micro-mesopore ratio in a wide range. This feature remains difficult to be achieved with established methods towards OMMCs and other nanoporous carbons. EDLCs based on OM-HSTC electrodes achieve high specific capacitance (133 F g^{-1} at 0.1 A g^{-1}) and excellent rate capability (126 F g^{-1} at 40 A g^{-1}) in 1 M TEABF$_4$/AN as the electrolyte (cell voltage up to 2.5 V). Accordingly, it achieves high specific energy of 29 Wh kg^{-1} at a specific power of 78 W kg^{-1}, and still maintains 23 Wh kg^{-1} at an ultrahigh specific power of 27 kW kg^{-1} in such organic electrolyte. When operated in IL electrolytes (cell voltage up to 3.5 V), the specific energy reaches up to 59 Wh kg^{-1} with a maximal specific power of 18 kW kg^{-1}. And they can also be employed as model materials for investigating transport phenomena in hierarchical pore systems, which is useful for many other fields where adsorption and transport in carbon materials play a role.

3. Carbon Electrodes and Energy Storage Mechanism of EDLCs

3.2. Towards the experimental understanding of the energy storage mechanism and ion dynamics in ionic liquid based supercapacitors by applying salt-templated carbon materials

To provide some detailed insights into the influence of the carbon pore structure and heteroatom doping on the energy storage mechanism in IL-based EDLCs, a series of salt-templated carbon materials and their corresponding nitrogen-doped counterparts with tunable pore structure and well-defined pore size dispersion are synthesized and used as model systems. When employing as EDLC electrodes in IL electrolytes, high energy density is achieved without compromising the admirable rate capability and stability. A quantitative model is proposed for the relationship between hierarchical pore structure/surface functionalization and ion dynamics. In terms of the energy storage itself, the possible phase transitions in the bulk of the IL confined in the carbon pores during charging/discharging lead to an unexpected deviation of the energy storage mechanism from the classical (compression) electrical double-layer theory.

3.2.1. Synthesis and characterization of STCs

A series of salt-templated carbons (STCs)[103, 140] with different pore structures are prepared by employing the salt template $ZnCl_2$ as porogen for well-defined micropores with or without additional disordered mesopores (**Scheme 3.3**). Sucrose and different amounts of $ZnCl_2$ are mixed in aqueous solution, followed by polycondensation of the carbohydrate at 160 ℃ with the salt template inside. Afterwards, the mixture is carbonized at 900 ℃ foll owed by thorough washing with HCl solution to remove the remaining $ZnCl_2$. TGA results of the materials indicate a small ash-content (less than 3 wt%) above 600 ℃ (**Figure 3.21**). X-ray diffraction (XRD) results (**Figure 3.22**) of all the samples show only broad (002) and (101) carbon peaks at 26° and 44° 2Theta, verifying the mainly amorphous carbon structure and the nearly complete absence of inorganic residuals after

carbonization and washing with HCl. Removal of the salt leads to the formation of micropores and mesopores at controllable ratio depending on the relative amounts of $ZnCl_2$ in different STCs (**Table 3.2**). This synthesis scheme stands out due to the tunable hierarchical pore structure formation with high surface area by a simple one-step salt-templating approach. Subsequently, nitrogen doping of STCs is carried out by dispersing the STCs in aqueous cyanamide solution followed by drying and cross-condensation at 800 ℃ under N_2 to obtain the corresponding nitrogen-doped STCs (NDSTCs, **Scheme 3.3**). No notable changes in the XRD (**Figure 3.22**) are observed after nitrogen-doping. The nitrogen content is 5-6 wt% for all these samples, as detected by elemental analysis (**Table 3.2**).
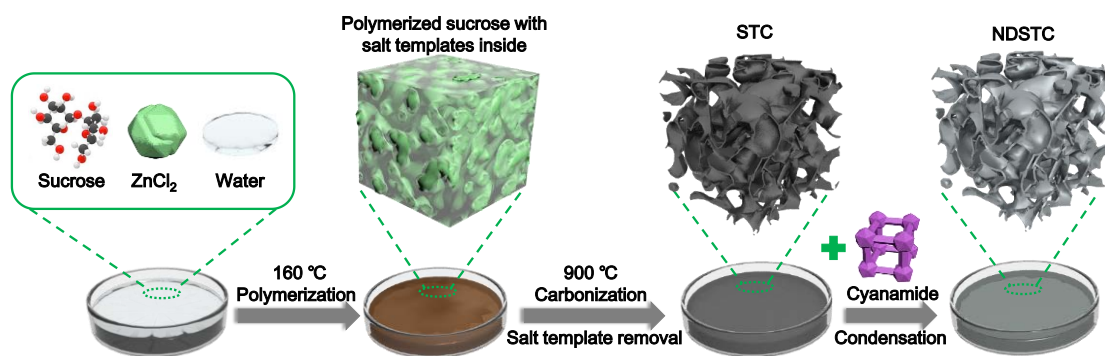
Scheme 3.3. Preparation of STCs and NDSTCs.
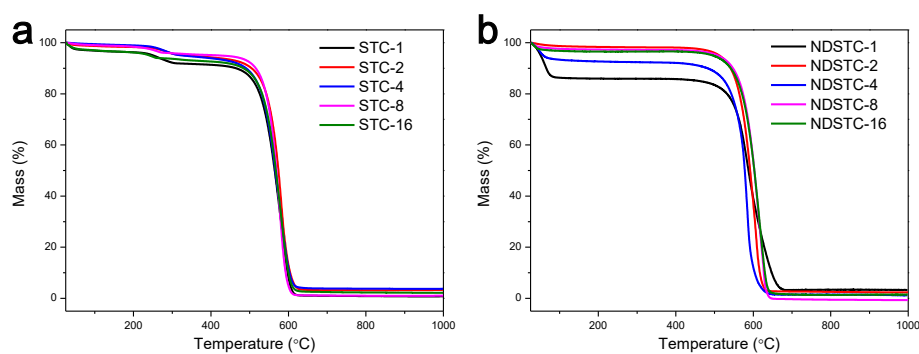
Figure 3.21. TGA results of (a) STCs and (b) NDSTCs measured under air flow with a heating rate of 5 ℃ min^{-1}.

3. Carbon Electrodes and Energy Storage Mechanism of EDLCs
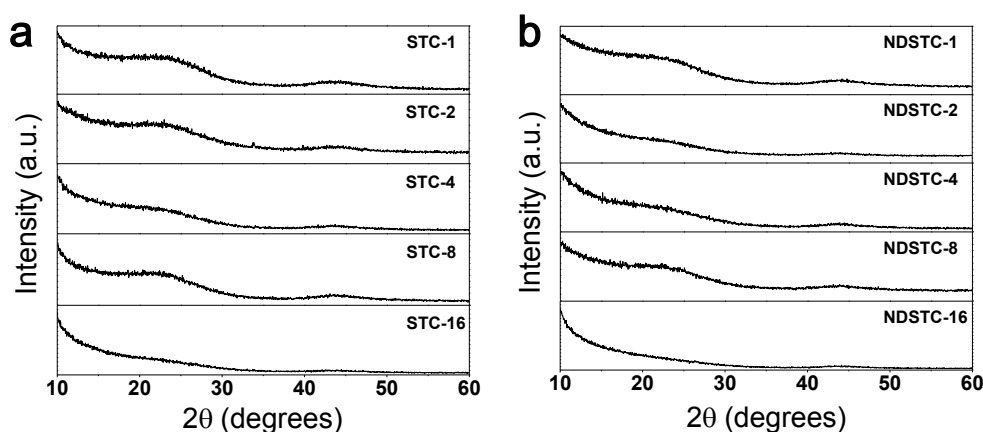
Figure 3.22. XRD patterns of (a) STCs and (b) NDSTCs.

Table 3.2. Mass ratio of $ZnCl_2$ to sucrose, BET SSA, total pore volume (V_t), DFT micropore volume (V_{mic}), DFT mesopore volume (V_{meso}), nitrogen content of the carbon materials by elemental analysis, as well as the thickness and mass loading of the corresponding electrodes.

	$ZnCl_2$:Sucrose (weight)	SSA (m^2/g)	V_t (cm^3/g)	DFT		Nitrogen content (wt%)	Thickness (µm)	Mass loading (mg cm^{-2})
				V_{mic} (cm^3/g)	V_{meso} (cm^3/g)			
STC-1	1	1138	0.51	0.39	0.11	/	126	9.6
STC-2	2	1430	0.81	0.33	0.42	/	122	7.6
STC-4	4	1739	1.08	0.36	0.67	/	125	5.7
STC-8	8	2203	1.48	0.36	1.08	/	118	5.0
STC-16	16	2324	1.66	0.41	1.25	/	123	4.8
NDSTC-1	1	1163	0.51	0.39	0.08	5.40	130	11.6
NDSTC-2	2	1468	0.80	0.37	0.38	5.52	123	6.9
NDSTC-4	4	1811	1.09	0.42	0.62	5.74	126	6.2
NDSTC-8	8	2181	1.42	0.36	1.02	6.09	119	5.0
NDSTC-16	16	2308	1.63	0.40	1.15	5.43	121	4.8
Ac-STC-1	1	1493	0.72	0.50	0.18	/	122	8.6
Ac-STC-16	16	2833	1.89	0.48	1.35	/	116	3.2

3. Carbon Electrodes and Energy Storage Mechanism of EDLCs

X-ray photoelectron spectroscopy (XPS) is employed to characterize the nitrogen/oxygen containing functional groups of nitrogen-doped samples (NDSTC-1 and NDSTC-16). The survey XPS spectra (**Figure 3.23**a and d) of the two samples reveal the presence of C, N, and O. Traces of residual zinc are also detected which is consistent with the results of TGA. The high-resolution N 1s spectra (**Figure 3.23**b and e) of both NDSTCs display four fitted peaks at 397.9, 398.5, 400.1, and 403.2 eV, which can be assigned to the pyridinic nitrogen, pyrrolic nitrogen, graphitic nitrogen, and N-O (oxidized nitrogen), respectively.[141] The high-resolution O 1s spectra (**Figure 3.23**c and f) can be deconvoluted into two peaks centered at 531.5, and 532.8 eV, corresponding to the carbonyl groups (C=O) and hydroxyl groups (C–OH), respectively.[142] The nitrogen contents of NDSTC-1 and NDSTC-16 are determined to be 6.01 and 3.68 at%, respectively, which suggests the success of nitrogen doping since negligible amount of nitrogen was detected in STC-1 and STC-16 by XPS in accordance with the results of elemental analysis (**Table 3.2**).
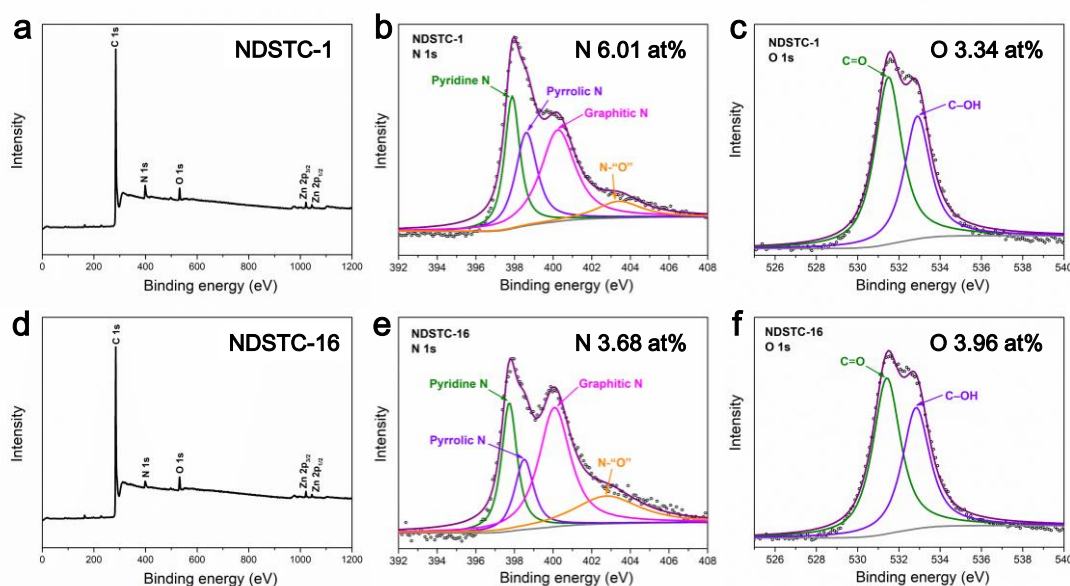
Figure 3.23. (a,d) XPS survey spectra and high-resolution (b,e) N 1s and (c,f) O 1s XPS spectra of (a-c) NDSTC-1 and (d-f) NDSTC-16.

N_2 (-196 ℃) and CO_2 (0 ℃) physisorption experiments are carried out to analyze the pore structures (**Figure 3.24**, **Figure 3.25** and **Table 3.2**). STC-1 shows a type I(a) isotherm, indicating its purely microporous structure, while STC-2 has the type I(b)

isotherm which suggests the presence of a small amount of narrow mesopores in addition to the micropores. STC-4, STC-8 and STC-16 exhibit type IV(a) isotherms with a continuous slope above a relative pressure of 0.2 with a hysteresis loop of H4 type in the relative pressure range between 0.4 and 0.9, indicating the existence of a significant mesopore volume (**Figure 3.24**a). To study the transformation of pore structure with the increase of the salt template, the PSD is further analyzed using the QSDFT for N_2 adsorbed on carbon with slit/cylindrical pore shape (**Figure 3.24**b). All the STC samples exhibit comparable micropore volumes around 0.4 cm^3 g^{-1} (**Table 3.2**). In the case of STC-1 with the moderate SSA of 1138 m^2 g^{-1}, the micropores account for the overwhelming fraction of the total pores (**Figure 3.24**c), verifying its microporous pore structure. With the increase of the salt loading, the SSAs gradually and significantly increase to 2203 m^2 g^{-1} for STC-8, followed by 2324 m^2 g^{-1} for STC-16 (**Figure 3.24**g and **Table 3.2**). The content of mesopores exhibits a drastic rise with increased template content (**Figure 3.24**h), which in turn results in a continuous augment of the total pore volumes from 0.51 cm^3 g^{-1} for STC-1 to 1.66 cm^3 g^{-1} for STC-16. In addition, the diameters of the mesopores are also enlarged slightly from 3 nm (STC-2) to 4 nm (STC-16) (**Figure 3.24**b) which is likely due to percolation of the salt templates, allowing to "fine tune" the hierarchical pore structure. The cumulative PSD plots (**Figure 3.24**c) indicate that micropores only contribute a small fraction of the total pore volume in the STC-4, STC-8, and STC-16. The distributions of micropores with diameters of 1.5 nm and below are further evaluated by NLDFT analysis of CO_2 physisorption measurements (**Figure 3.24**d-f). All samples contain three kinds of well-defined narrow micropores with diameters of 0.35, 0.55, and 0.80 nm, corresponding to salt-template clusters with different sizes (**Figure 3.24**e). A higher $ZnCl_2$/sucrose ratio leads to a larger volume of micropores with the diameter of 0.80 nm, which is in the range of the ion size of EMIm⁺ (0.76 nm). This underlines that the salt-templating method provides control over the size and amount of narrow micropores and mesopores. The N_2

3.   Carbon Electrodes and Energy Storage Mechanism of EDLCs

physisorption results of NDSTCs show the similarity of pore structure compared with their corresponding parental STCs (**Figure 3.25** and **Table 3.2**), indicating that the nitrogen doping process is a molecular cross-condensation which has no significant effects on the pore structure. The presence of comparable amounts of nitrogen in purely microporous NDSTC-1 and other hierarchical porous NDSTCs (**Table 3.2**) suggest the homogenous nitrogen doping along both micropores and mesopores.
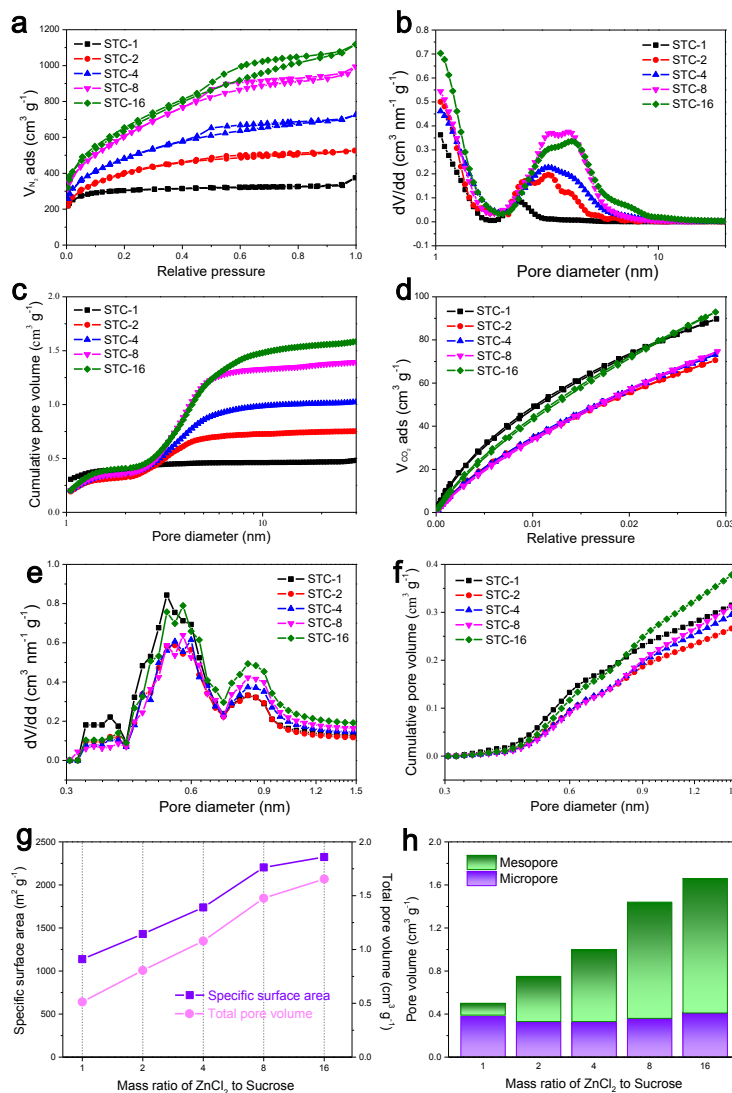
Figure 3.24. (a) N_2 physisorption isotherms (at -196 ℃) with corresponding (b) differential and (c) cumulative QSDFT PSDs as well as (d) CO_2 physisorption (at 0 ℃) isotherms with corresponding (e) differential and (f) cumulative NLDFT PSDs of the STCs. (g) SSA and TPV of STCs with the increase of $ZnCl_2$. (h) Mesopore and micropore volume of STCs with the increase of $ZnCl_2$.
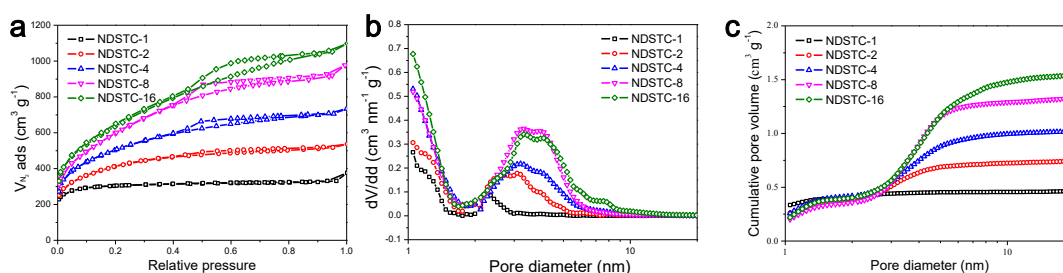
Figure 3.25. (a) N_2 physisorption isotherms (at -196 ℃) with corresponding (b) differential and (c) cumulative QSDFT PSDs of the NDSTCs.

The influence of the amount of $ZnCl_2$ and nitrogen doping on the pore structure is further studied by TEM. Low content of $ZnCl_2$ (STC-1 and STC-2) leads to a rather dense morphology with the presence of abundant narrow micropores, while mesopores can hardly be observed (**Figure 3.26**a-b). With the gradual increase of $ZnCl_2$ (STC-4, STC-8, and STC-16), the morphologies clearly exhibit a distinct trend of being less dense and more open, reflecting the development of mesopore systems (**Figure 3.26**c-e). After nitrogen doping, the NDSTCs consist of pore structures which are comparable to their corresponding STC parents (**Figure 3.26**f-j). This is in good accordance with the physisorption experiments.
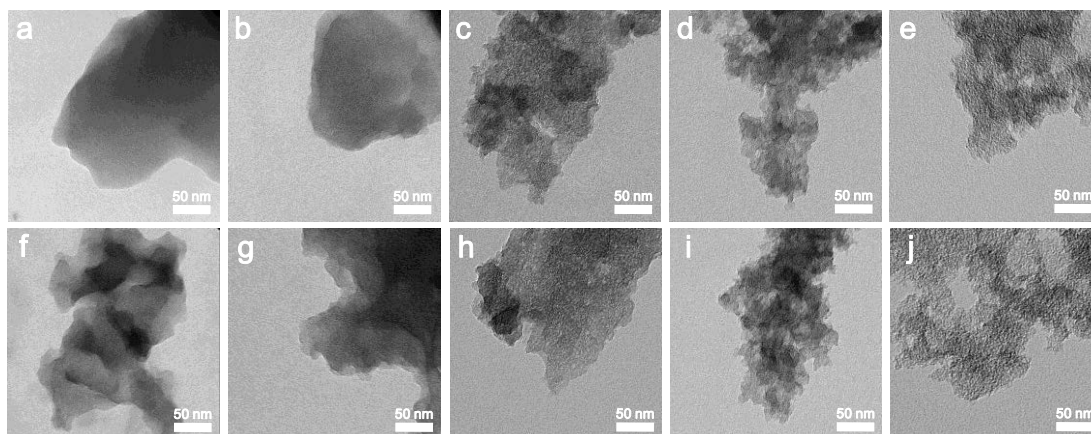
Figure 3.26. TEM images of the STCs and the respective NDSTCs. (a) STC-1, (b) STC-2, (c) STC-4, (d) STC-8, (e) STC-16, (f) NDSTC-1, (g) NDSTC-2, (h) NDSTC-4, (i) NDSTC-8, (j) NDSTC-16.

In the Raman spectra (**Figure 3.27**), the wide (157-196 cm^{-1}) D-bands (**Table 3.3**) in all samples reveal the existence of abundant disordered sections. The peak height ratio of the D- and G-band (I_D/I_G) is employed to evaluate the level of carbon ordering in porous carbons.[133-135] The comparable I_D/I_G value (**Table 3.3**) with the

increase of salt-template (the values of STC-1, STC-2, STC-4, STC-8, and STC-16 equal 1.3, 1.3, 1.2, 1.1, and 1.3, respectively) indicates comparable degree of aromatization and thereby no major differences in the conductivities of the STCs can be expected.
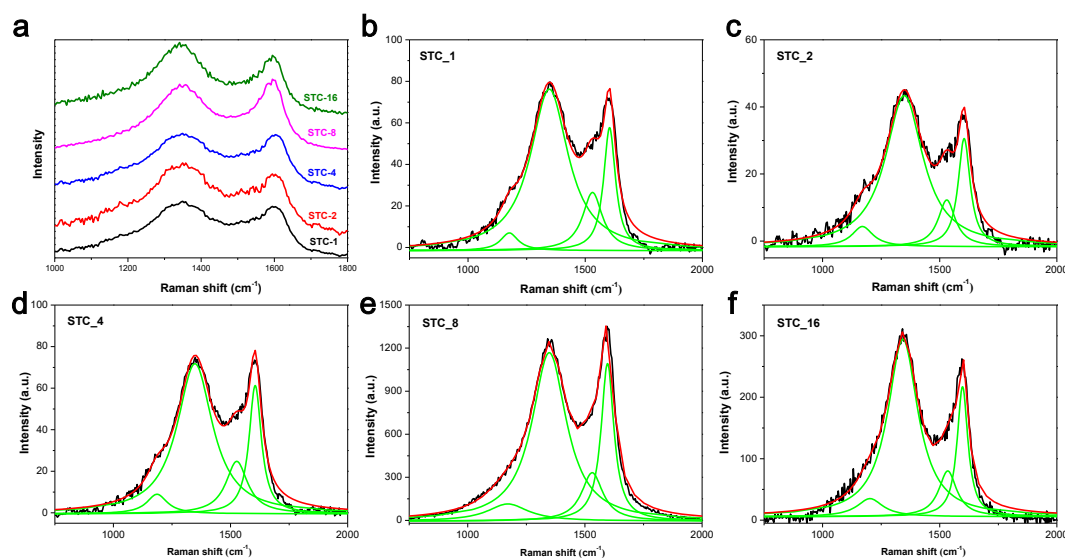
Figure 3.27. (a) Raman spectra of STCs and (b-f) corresponding fitting curves of STC-1, STC-2, STC-4, STC-8, and STC-16, respectively.

Table 3.3. I_D/I_G ratio, and FWHM of the D-band of the carbon materials obtained by Raman spectroscopy.

	STC-1	STC-2	STC-4	STC-8	STC-16
I_D/I_G	1.3	1.3	1.2	1.1	1.3
FWHM of D band (cm⁻¹)	196	195	184	179	157

3.2.2. EDLC performance in ionic liquid electrolytes

To establish structure-performance relationships of the STCs for EDLCs, the carbon samples are fabricated into self-standing electrodes and characterized with CV, GCPL, and EIS measurement in solvent-free ionic liquid (EMImBF$_4$). All the Nyquist plots are nearly vertical in the low-frequency region except for STC-1 due to its partially inaccessible micropores (**Figure 3.28**a). The CV curves show nearly rectangular shapes from 0-3.5 V at different scan rates (**Figure 3.29**a-e) and GCPL curves are close to symmetric triangle at a low specific current of 0.2 A g⁻¹ (**Figure**

3. Carbon Electrodes and Energy Storage Mechanism of EDLCs

3.28b) - a typical characteristic of double-layer capacitor behavior. However, all these CV curves exhibit small peaks at a cell voltage of ~0.6 V (**Figure 3.30**a), which can be attributed to the decoordination of ions when entering micropores during charging/discharging as it will be further discussed in the following section. Even more pronounced peaks start to emerge at higher cell voltages. At a low specific current of 0.2 A g^{-1}, the specific capacitance of microporous STC-1 reaches 49 F g^{-1} as determined by the GCPL measurements (**Figure 3.30**b-c). With the increase of the $ZnCl_2$, the specific capacitance shows a drastic rise to 149 F g^{-1} (STC-2) which then levels off to 178 F g^{-1} (STC-16, **Figure 3.30**b-c), in spite of the further significant increase of the SSAs (**Figure 3.24**g). This results in an increase of the specific capacitance normalized by BET SSA from 4.3 $\mu F\ cm^2$ (STC-1) to 10.4 $\mu F\ cm^2$ (STC-2), followed by an apparent drop to 8.9 $\mu F\ cm^2$ (STC-4) and ~7.5 $\mu F\ cm^2$ (STC-8 and STC-16, **Figure 3.30**c). The rather low normalized specific capacitance at 0.2 A g^{-1} of STC-1 is ascribed to the restricted accessibility of the electrode surface within the purely microporous structure, with a large portion of the carbon surface being not accessible even during a slow, quasi-equilibrium charging/discharging process. The inferior pore accessibility of STC-1 is also revealed by the clear deviation of the Nyquist plot in the low frequency range (**Figure 3.28**a).[143] The drastic rise of normalized specific capacitance from STC-1 to STC-2 is caused by the introduction of mesopores, which renders the whole carbon surface available to ions at a low charging/discharging rate. Due to its enlarged SSA and mesopore volume, STC-2 reaches a relatively high specific capacitance of 149 F g^{-1}. It is worth mentioning that further increase of the SSA only gives rise to the slight improvement of specific capacitance, leading to the decline of normalized specific capacitance to approximate 7.5 $\mu F\ cm^2$ for STC-8 and STC-16 (**Figure 3.30**c). This is consistent with the rather general observation that more and more increase of SSAs above 1500 m^2 g^{-1} has only small impact on the specific capacitance, and the pore size distribution becomes crucial.[53, 144] This is also supported by analysis of a CO_2-activated STC-16

3. Carbon Electrodes and Energy Storage Mechanism of EDLCs

(Ac-STC-16) which "only" reaches 154 F g^{-1} (**Figure 3.31**) despite its ultrahigh SSA of 2833 m^2 g^{-1} with the similar pore structure of STC-16 (**Figure 3.32**). On base of the normalized specific capacitance of 5.4 µF cm^{-2}, this material provides an even lower specific capacitance compared with that of STC-16 (**Figure 3.31**b-c).[132]
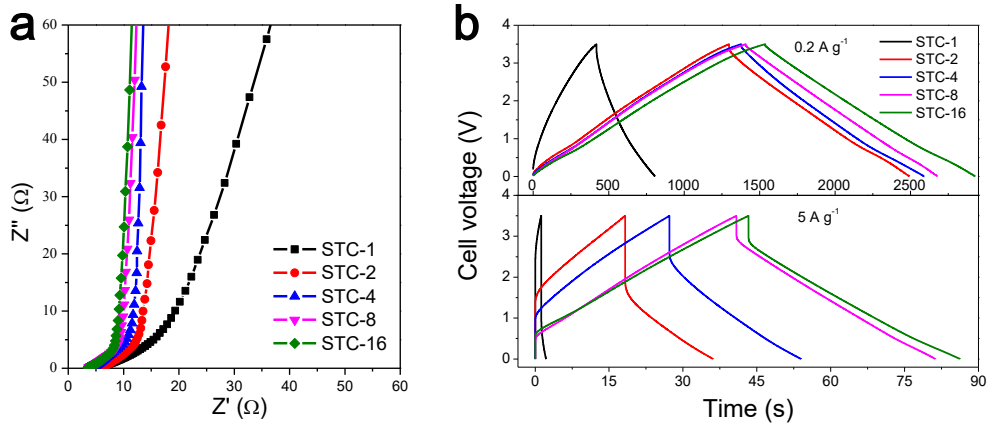
Figure 3.28. (a) Nyquist plots of the EDLC with STCs as electrodes in EMImBF$_4$ electrolyte. (b) Charge/discharge profiles at 0.2 and 5 A g^{-1}.
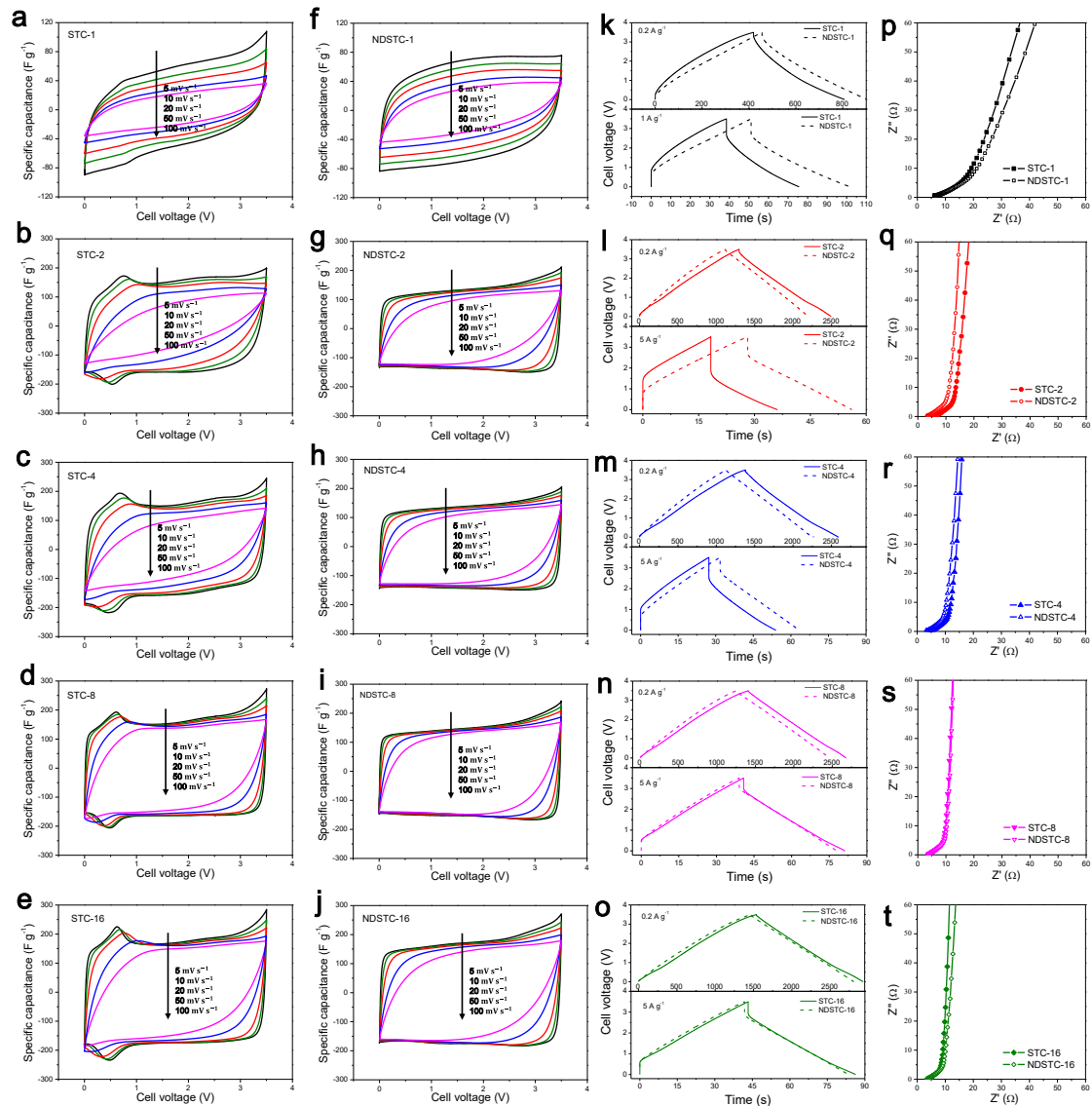
Figure 3.29. EDLC performance of the synthesized STCs and NDSTCs tested in EMImBF$_4$ ionic liquid using a two-electrode configuration: Cyclic voltammograms at different scan rates of (a-e) STCs and (f-j) NDSTCs. (k-o) Comparison of charge/discharge profiles at different specific currents between STCs and their corresponding NDSTCs and (p-t) Nyquist plots of STCs and their corresponding NDSTCs.
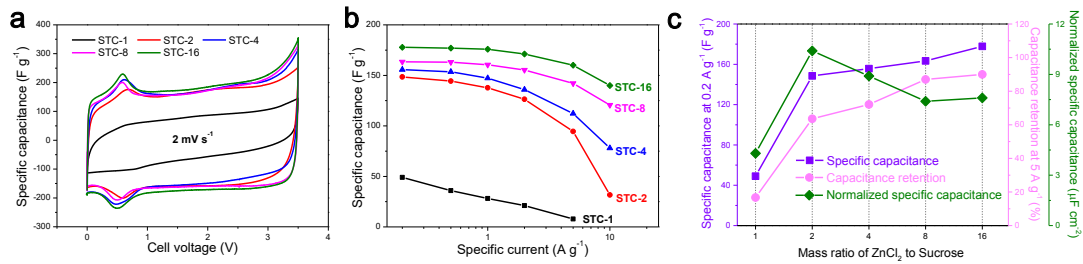
Figure 3.30. EDLC performance of STCs tested in EMImBF$_4$ ionic liquid using a two-electrode configuration: (a) Cyclic voltammograms at 2 mV s^{-1}, (b) capacitance retention with specific current increase, and (c) influence of the amount of ZnCl$_2$ on the specific capacitance at 0.2 A g^{-1}, capacitance retention at 5 A g^{-1}, and specific capacitance normalized by the BET SSAs of the obtained STCs.

Figure 3.31. EDLC performance comparison of STC-16 and Ac-STC-16 tested in EMImBF$_4$ ionic liquid using a two-electrode configuration: (a) Cyclic voltammograms at different scan rates, (b) charge/discharge profiles at different specific currents, (c) capacitance retention with specific current increase, and (d) Nyquist plots.

The rate capabilities show a clear improvement from STC-1 to STC-8 with the higher amounts of the mesopores, which is seen by the smaller voltage drop (**Figure 3.28**b) and higher capacitance retention (**Figure 3.30**b-c). Typically, in the case of STC-1, STC-2, and STC-4, only part of the surface in the micropores is used by ions at a high charging/discharging rate because of the poor ion dynamics. This can be addressed by the substantial development of mesopores (introduced by increasing amounts of salt template), leading to the shrinkage of domains of micropores, thus significantly improving the rate capability. It should be noticed that the larger areal

loading (at similar thickness) of the electrodes with the microporous carbons could also contribute their worse rate capability by decreasing migration dynamics of charge carriers, especially at very high current density. On the other hand, STC-8 and STC-16 exhibit similar rate capabilities with polarization induced voltage drops of 0.34 V and 0.37 V, and capacitance retentions of 87% and 89%, respectively, at a specific current of 5 A g^{-1}, despite their apparent different content of mesopores (**Figure 3.24**h). This is in accordance with the Nyquist plots of the STCs (**Figure 3.28**a), where the length of the 45° sloped curve (known as the Warburg portion in the middle-frequency region, related to the transport of electrolyte ions into the carbon pores) shows an apparent reduction from 10.9 Ω for STC-1 to 4.9 Ω for STC-8, while constancy of this value (~4.9 Ω) is observed for STC-8 and STC-16. This suggests that the further shortening of transport length in the micropores in STC-8 has little influence on the rate capability. It makes also no sense to add more mesopores as this will harm the volumetric efficiency.[28] To identify the rate determining process, the EDLC performance is tested with Ac-STC-16 as an "activated" electrode material where the micropore sizes are slightly enlarged with broader distribution (**Figure 3.32**), so that the ion transport dynamics at the junctions of mesopores and micropores are expected to be improved. However, the rate capability is almost impervious to the enlargement of micropores, as revealed by the similar voltage drop (1.1 V and 1.0 V), and capacitance retention (79% and 81%) of STC-16 and Ac-STC-16 at 10 A g^{-1}, as well as their similar Nyquist plots (**Figure 3.31**b-d). The slightly lower capacitance retention of STC-16 is attributed to the absent peak at ~0.6 V at the high charging/discharging rate (**Figure 3.29**e). Besides, in the previous section 3.1, the hierarchical porous carbon with ordered mesopores (OM-HSTC_2_2.05) shows outstanding rate capability (0.64 V voltage drop and 88% capacitance retention at 10 A g^{-1}), compared with that of the STCs with disordered and relatively narrow mesopores. Therefore, it is concluded that the limiting factor of the ion dynamics inside the mesopores comes into play when

the ratio of mesopores to micropores surpasses 3:1 in pore volume (STC-8). Moreover, after activation, the peak at the cell voltage of ~0.6 V disappears in the CV curves of Ac-STC-16 (**Figure 3.31**a), which indicates that the presence or absence of such a peak is related to the size distribution of the micropores.
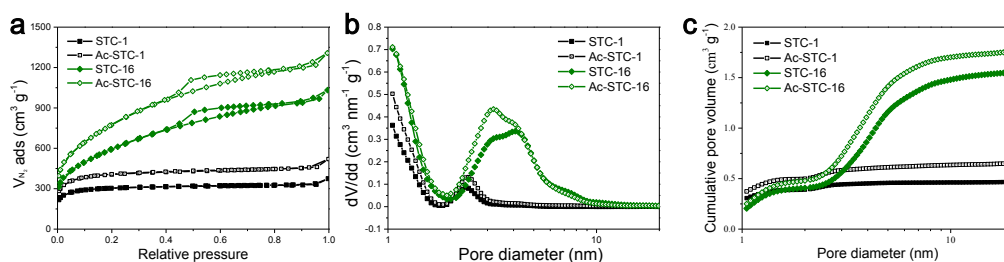
Figure 3.32. (a) N_2 physisorption (at -196 ℃) isotherms with corresponding (b) differential and (c) cumulative QSDFT PSDs of the STCs and Ac-STCs.

Similar to STCs, the nitrogen-doped NDSTCs exhibit an ideal double-layer capacitance behavior, as indicated by the regular shape of the CV curves (**Figure 3.33**a and **Figure 3.29**f-j), the symmetrical triangle shapes with some small voltage drops of GCPL curves (**Figure 3.29**k-o), as well as the nearly vertical Nyquist plots in the low-frequency region (**Figure 3.29**p-t, except NDSTC-1 because of its partially inaccessible micropores). Compared with the CV curves of the STCs (**Figure 3.30**a and **Figure 3.29**a-e), the peaks at the cell voltage of ~0.6 V disappear in those of the NDSTCs, resulting in a slight decrease (~5%) of capacitance at the low specific current of 0.2 A g^{-1} when all the surface is accessible, except in case of NDSTC-1 (**Figure 3.33**b-c). The absence of the peak at ~0.6 V might contribute to the lower capacitance, and at least in the present case nitrogen doping does not improve the capacitance at all. In order to rule out the presence of redox peaks which are invisible in two-electrode configuration, the CV curve of NDSTC-16 is also measured by a three-electrode configuration (**Figure 3.34**). The CV curve shows a nearly rectangular shape without redox peaks, in good accordance with the two-electrode configuration. Therefore, it is deduced that the results tested by two-electrode configurations are representative for the electrochemical properties under real potential control. Moreover, it also proves that the nitrogen/oxygen

containing functional groups and the trace amounts of Zn induce no redox peaks in the CV curve. To further eliminate the possibility of Zn causing redox peaks in the CV curves, EDLCs in aqueous electrolytes were tested. All the CV curves of STC-1, NDSTC-1, STC-16, and NDSTC-16 (**Figure 3.35**) in the 1 M Na_2SO_4 aqueous electrolyte show perfect rectangular shapes without the presence of any redox peaks within the investigated potential range.
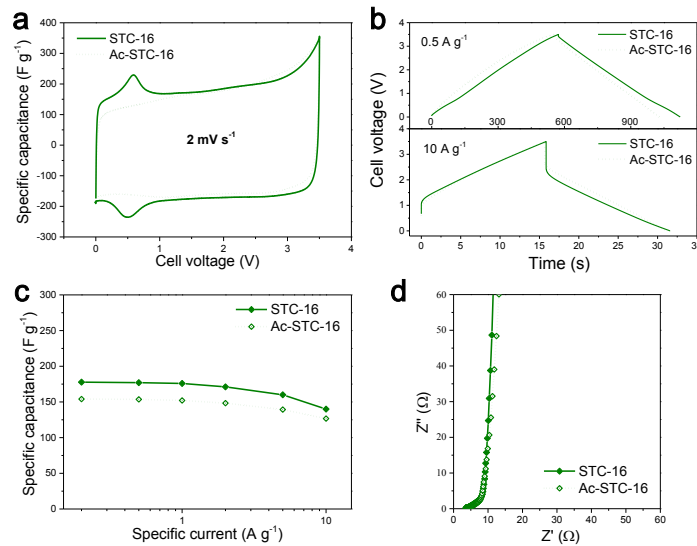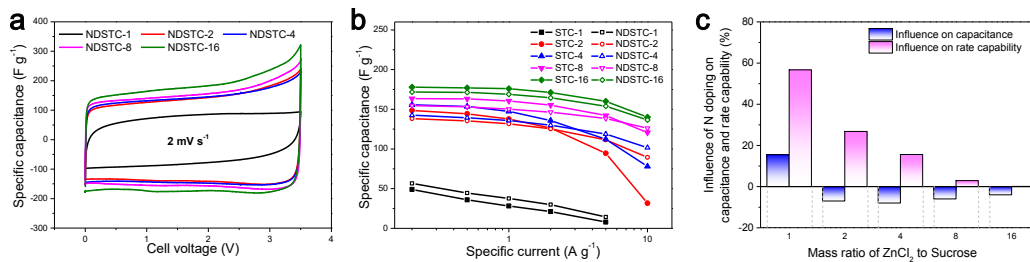

Figure 3.33. EDLC performance of NDSTCs tested in $EMImBF_4$ ionic liquid using a two-electrode configuration: (a) Cyclic voltammograms at 2 mV s^{-1}, (b) capacitance retention with specific current increase, and (c) influence of nitrogen doping on specific capacitance at 0.2 A g^{-1} and capacitance retention at 5 A g^{-1} compared with the corresponding STCs.
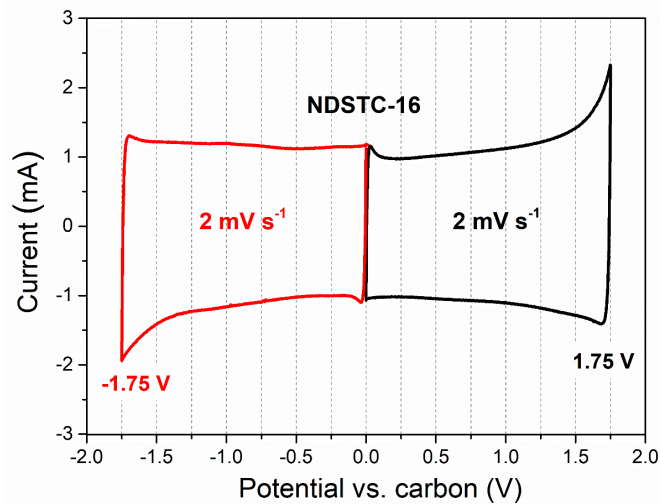
Figure 3.34. Cyclic voltammetry curves of NDSTC-16 at 2 mV s^{-1} tested in $EMImBF_4$ ionic liquid using a three-electrode configuration.
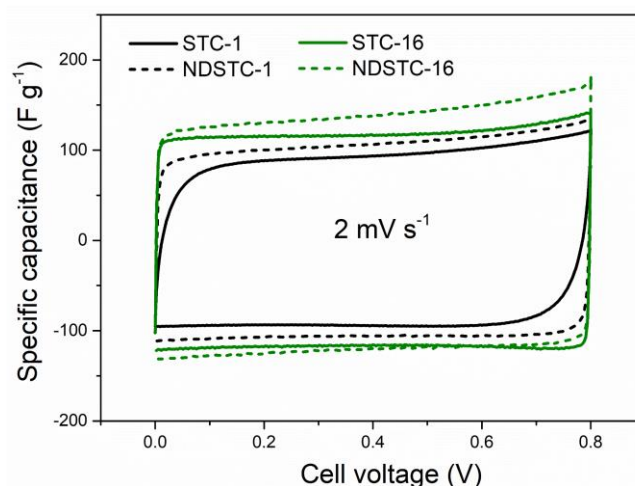
Figure 3.35. Cyclic voltammetry curves of STC-1, NDSTC-1, STC-16, and NDSTC-16 at 2 mV s^{-1} tested in 1 M Na$_2$SO$_4$ aqueous solution using a two-electrode configuration.

Opposite to pure capacitance, a remarkable influence of nitrogen doping on the EDLC performance can be attributed to the improvement of wettability due to specific interactions between IL ions and doped sites in the carbon pore walls, which substantially promotes the ion dynamics inside micropores. This gives the explanation of the 16% capacitance enhancement of STC-1 after nitrogen doping (**Figure 3.33**c). As discussed above, the capacitance of STC-1 at the quasi-equilibrium state is mainly hindered by the poor accessibility of its micropores thus leading to the higher capacitance of NDSTC-1 (**Figure 3.33**c) and Ac-STC-1 (**Figure 3.36**). The better EDLC performance of NDSTC-1 also indicates the success of doping nitrogen in micropores, consistent with the elemental analysis (**Table 3.2**). On the contrary, the capacitance of other STCs is not limited by the ion dynamics inside micropores in the quasi-equilibrium state and thus little influence of the specific capacitance by the nitrogen doping is observed (**Figure 3.33**c). This mechanism also explains the decreasing influence of nitrogen doping on the rate capabilities with the increase of the ZnCl$_2$ (**Figure 3.33**c).
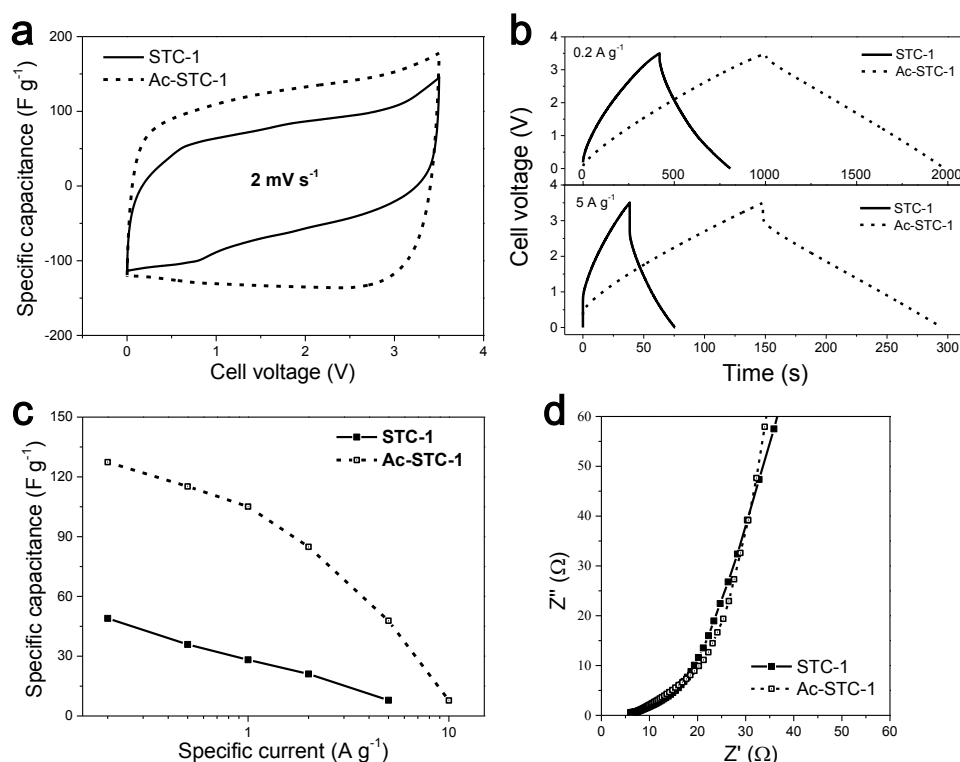
Figure 3.36. EDLC performance comparison of STC-1 and Ac-STC-1 tested in EMImBF$_4$ ionic liquid electrolyte using a two-electrode configuration: (a) Cyclic voltammograms at different scan rates, (b) charge/discharge profiles at different specific currents, (c) capacitance retention with specific current increase, and (d) Nyquist plots.

It is deduced that the EDLC performance comparison between different carbon electrodes is unaffected by the electric conductivity and is exclusively dependent on the ion dynamics inside the carbon pores. Because the electric conductivities of all these STC and NDSTC electrodes approximate to each other as indicated by the intercepts along the real axis (~5 Ω) in the EIS measurement (**Figure 3.28**a and **Figure 3.29**p-t). This is in accordance with their similar degree of aromatization as reflected by the Raman spectroscopy (**Figure 3.27** and **Table 3.3**).

With the highest capacitance and best rate capability among all the samples, STC-16 was selected as the model material to test stability and calculate its specific energy/power. The stability was measured by the voltage floating test, which is a more demanding benchmarking to survey the electrochemical performance stability compared to voltage cycling.[145] The cell voltage was held at 3.5 V for 100 h

3. Carbon Electrodes and Energy Storage Mechanism of EDLCs

and interrupted by cycling at 1 A g^{-1} after every 10 h. This approach provides a more strict condition than voltage cycling, which means an EDLC cell is more likely to undergo failure during floating test. And it is the more realistic representation of the life of a supercapacitor. A high electrochemical stability of STC-16 is revealed by the desirable capacitance retention of more than 92% (significantly above the industry-relevant level of 80%[145]) and the almost unchanged GCPL curves (**Figure 3.37**a). In addition, after cycling at a high charging/discharging rate at 10 A g^{-1} for 10,000 cycles, capacitance retention over 90% is obtained, indicating its admirable cycling stability at such a high rate. The Ragone plot (**Figure 3.37**b) of EDLCs using STC-16 as electrodes with a mass loading of 4.8 mg cm^{-2} shows that the symmetric cells provide the maximum specific energy of 76 Wh kg^{-1} (32 Wh L^{-1}) at a specific power of 0.2 kW kg^{-1} (0.09 kW L^{-1}), with a slight drop to 72 Wh kg^{-1} (31 Wh L^{-1}) at 1 kW kg^{-1} (0.43 kW L^{-1}), and still maintains 39 Wh kg^{-1} (17 Wh L^{-1}) at a specific power of 9 kW kg^{-1} (3.9 kW L^{-1}). The specific energy is indeed one order of magnitude higher than that of commercial EDLCs, without losing the excellent power capability. This outstanding property is attributed to the optimized pore architecture with all micro- and mesopores, plus the access of a new mode of charge storage, in the volume of the IL rather than only surface double layer compression as it will be discussed below. Moreover, the correlation of micropores and mesopores to the EDLC performance is also revealed in Ragone plots (**Figure 3.37**b). The purely microporous STC-1 shows the worst performance due to the poor micropore accessibility for electrolyte ions. With the introduction and increase of mesopores, STC-2 and STC-8 exhibit an apparent trend of improvement in both specific power and energy. On the other hand, the performance (especially the power density) of the STC-8, STC-16, and NDSTC-16 is similar to each other, further strengthening the finding that mesopore content or doping with nitrogen have little influence when the ratio of mesopore to micropore surpasses a threshold value of 3:1 in pore volume as mentioned above.
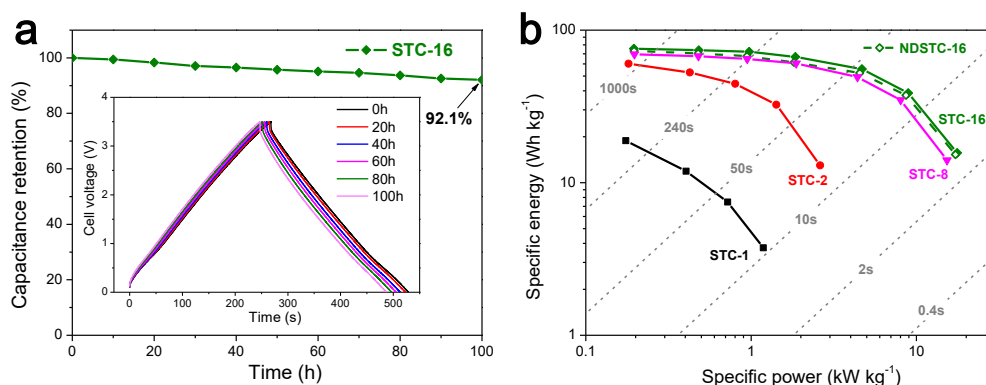
Figure 3.37. (a) Floating stability of STC-16 at a specific current of 1 A g^{-1} for 100 h floating at 3.5 V. The inset shows the charge/discharge profiles every 20 h. (b) Ragone plots of EDLCs using STC-1, STC-2, STC-8, STC-16 and NDSTC-16 as electrodes.

3.2.3. Influnece of pore structure and heteroatom doping on the energy storage mechanism of IL-based EDLCs

Base on the above results, a model (**Scheme 3.4**) is proposed to explain how the pore structure and surface chemistry affect the ion migration as well as the structural rearrangements in the bulk electrolyte, thus contributing to the EDLC performance. The inferior EDLC performance of purely microporous carbon (STC-1) even during the quasi-equilibrium charging/discharging process at 0.2 A g^{-1} is ascribed to the poor micropore accessibility caused by the low mobility of IL ions in such narrow pores, which can be relieved by introducing mesopores and improving wettability/enlarging micropores, respectively (**Scheme 3.4**, first line). Therefore, STC-2 and STC-4 with more mesopores (**Figure 3.30**a-c), NDSTC-1 with improved wettability (**Figure 3.29**f and k), as well as Ac-STC-1 with larger micropores (**Figure 3.36**) exhibit a noticeable enhancement in both specific capacitance and rate capabilities. In comparison, the micropores in the hierarchical micro-mesoporous carbon (STC-2 and STC-4) are fully accessible at the low charging/discharging rate, as revealed by their remarkably increased capacitance when compared to STC-1. But at the higher charging/discharging rate of 5 A g^{-1}, the ion migration again

becomes the limiting factor, leading to the drastic drop of capacitance (**Figure 3.30**b). Thus, larger amount of mesopores (STC-8 and STC-16) and nitrogen doping (NDSTC-2 and NDSTC-4) are needed here (**Scheme 3.4**, second line), resulting in the increase of accessible surface areas and higher capacitance at this rate. Nevertheless, at the ultrahigh charging/discharging rate of 10 A g^{-1} even STC-8 and STC-16 with the highest amount of mesopores exhibit a notable capacitance drop (**Figure 3.30**b). The rate limiting factor switches from ion dynamics inside micropores to ion transport inside mesopores, as the depth of micropores is already short enough for ions to enter practically instantaneously (**Scheme 3.4**, third line). The general limitation for ion transport in presence of large mesopore ratio seems to relate to the viscosity of the electrolyte. As a consequence, it makes no difference to further increase the volume of the mesopores (STC-16 and Ac-STC-16), or dope with nitrogen to reduce the ion migration resistance inside the micropores (NDSTC-8 and NDSTC-16).
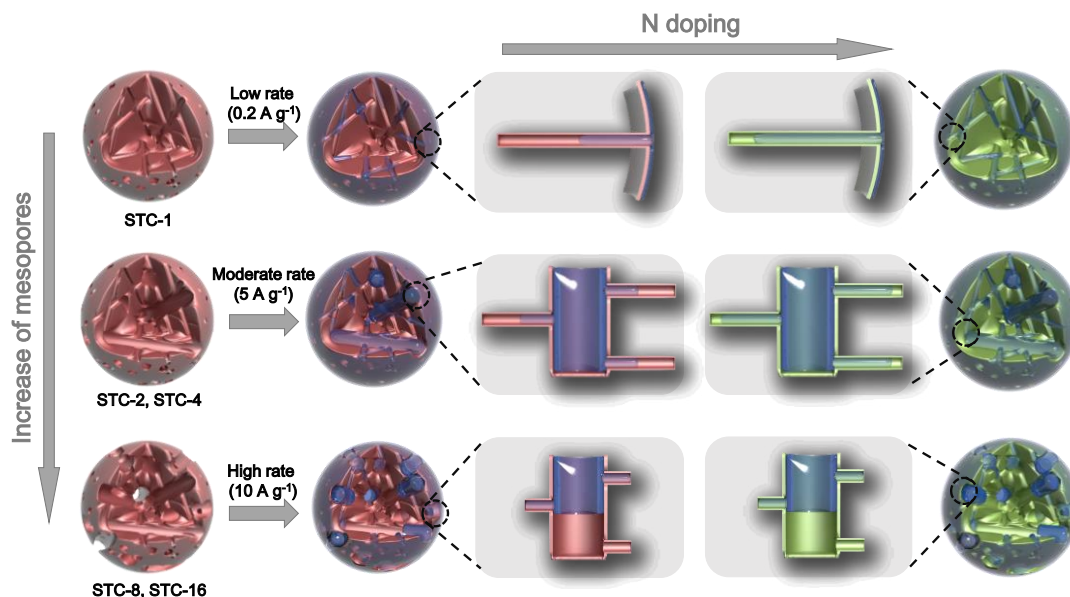
Scheme 3.4. Influence of different pore structures and nitrogen doping on the ion migration process at different charging/discharging rates.

The origin of the peaks in the CVs of the STCs at a cell voltage of ~0.6 V remains an open question. Interestingly, the micropore sizes in the materials are close to the size of EMIm$^+$. The fact that such peaks are also visible in purely microporous STC-1

3. Carbon Electrodes and Energy Storage Mechanism of EDLCs

and that their area increases at higher micropore accessibility indicates that the process that is responsible for their appearance is taking place in the micropores rather than in mesopores. To my opinion, the origin of the peak is likely due to the decoordination of IL ions (a single ion loses all its neighboring Coulombs) when entering narrow micropores with the size of the ions. This process is fully reversible as revealed by the small peak at the same cell voltage of ~0.6 V during discharging in the CV curves (**Figure 3.30**a) and the superior stability (**Figure 3.37**a). It can thus be concluded that decoordination of single IL units and their placement in appropriately sized micropores contributes to the actual energy storage mechanism in EDLCs with IL electrolytes, which is also in agreement with some literature.[128-129] In the case of the NDSTCs with the same micropore size, the ion-pore wall interactions are stronger caused by the (weakly) nitrogen-doped polar surface.[113] In this case, the micropores in NDSTCs are already wetted by IL ions at zero potential (which is not the case in STCs), and thus a narrow peak due to entering of single IL units in the micropores of STCs is not observed.

In addition to the (later vanishing) peaks at ~0.6 V during charging and discharging, the overall charge density is simply too high for ordinary double layers, plus there is another pronounced peak at very high voltage in the CVs of all mesopore-containing materials discussed here not related to material degradation (**Figure 3.30**). Basically, a cell voltage of 3.5 V and specific capacitance up to 178 F g^{-1} relates to a stored charge of 623 C g^{-1}. This is remarkable considering the huge size of the ions of IL electrolytes. It is illustrative to calculate the surface area occupied by one charge. Taking STC-16 as an example, the large EMIm$^+$ ions (0.76 × 0.43 nm) must be attributed to a calculated surface area per ion of 0.6 nm^2 which is already very close to the molecular dimensions of these ions, implying a close to dense layer of cations on the carbon surface. In STC-2 with a lower mesopore ratio, EMIm$^+$ ions are formally even attributed to a calculated area of only 0.44 nm^2. Such a high double-layer compression appears to be unrealistic for large IL ions in absence of

solvent molecules. In contrast to aqueous and organic electrolytes, the density of cations and anions in ionic liquids should stay close to the bulk value, i.e. the energy is essentially not stored in ion compression, but rather in ion ordering rearrangement towards Coulombic higher voltage situations, which obviously can propagate about nanometers into the bulk.

There is no doubt about the contribution of double-layer formation on carbon surfaces to the energy storage in IL electrolytes in general, but from the results it is concluded the absence of double-layer compression as present in aqueous and organic electrolytes (**Scheme 3.5** top), as it has already been shown.[57, 127] Instead, there seems to be a strong contribution of structural changes in the bulk phase of the ILs to the energy storage mechanism in EDLCs.

This indeed would request a paradigm change of energy storage, as then the majority of energy is not stored in micropores (and cannot be related to a high specific surface area), but rather in appropriately designed mesopores which enable high energy Coulombic rearrangements of the IL in the bulk. In these mesopores, the structural changes of IL ions can be assigned to disorder-order transitions in the bulk of the electrolyte (**Scheme 3.5** bottom). It has been shown that the present family of bulk IL are actually liquid crystals and the peak could, for instance, originate from the formation and disappearance of differently organization schemes of the bulk IL in mesopores.[146] According to this view, such contributions cannot be observed in microporous STC-1 and NDSTC-1, and their intensity increases with larger mesopore contribution in the carbon materials. The process is fully reversible as indicated by the high stability of the devices and the nearly perfect symmetrical charge-discharge curves at low current densities.

3. Carbon Electrodes and Energy Storage Mechanism of EDLCs

Supercapacitor anodes with solvent-based electrolytes (compression double-layer)

Carbon Electrode (without potential) — Carbon Anode (low potential) — Carbon Anode (high potential)

Supercapacitor anodes with ionic liquid electrolytes (local ordering transitions)

Carbon Electrode (without potential) — Carbon Anode (low potential) — Carbon Anode (high potential)
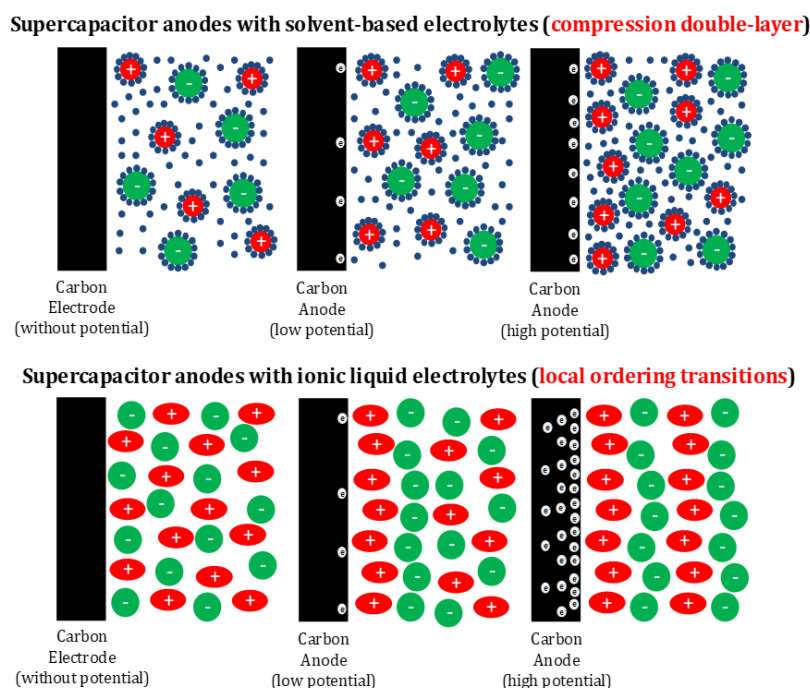
Scheme 3.5. Schematic of the (negative) electrode-electrolyte interface in EDLCs working with solvent-based (top) and IL (bottom) electrolytes.

In principle, any form of chemical energy can be directly translated into a voltage signal, if that the event occurring in the material is coupled to a charge flow in the collector electrodes, and vice versa. For all chemical events, a voltage signal can be calculated using the Nernst equation, as long as the chemical effect creates a charge flow in the electrochemical device. In this regard, the small peak at ~0.6 V in the CV curves of STCs would translate to ~ 60 kJ mol^{-1} which is in the range of strong inter-molecular forces such as hydrogen-bonds or Coulomb dissociation. This further justifies the rationality of the deduction that the small peak is originated from the decoordination of IL ions. Even more importantly, the higher voltage of over 3 V, where a pronounced peak takes place in the CV curves, would translate to a very high enthalpy of above 300 kJ mol^{-1} which is higher than that of covalent bonds, but in the range of the melting of salts and other collective properties and structural transitions involving serious changes in the ion coordination numbers. This makes it clear that such transitions must be related to collective properties and

in structural transitions in the bulk of the IL, in accordance with the proposed "ordering transition theory" (**Scheme 3.5**).

The present data is regarded as an experimental prove that the energy storage mechanism in such IL-based EDLCs significantly deviates from the traditional theory of double-layer compression as present in aqueous and organic electrolytes, and that there is a notable contribution of ion ordering transitions in the bulk of the ILs to the energy storage mechanism in IL-based EDLCs.

In summary, a series of hierarchical porous carbon with different amounts of well-defined micropores and mesopores was synthesized. EDLC based on STC electrodes achieves high specific capacitance of 178 F g^{-1} at 0.2 A g^{-1} and excellent rate capability (140 F g^{-1} at 10 A g^{-1}) combined with an admirable stability, in the ionic liquid electrolyte with the voltage window of 0-3.5 V. Accordingly, it delivers the maximum specific energy of 76 Wh kg^{-1} at a specific power of 0.2 kW kg^{-1}, and still maintains 39 Wh kg^{-1} at a specific power of 9 kW kg^{-1}. The specific energy is indeed one order of magnitude higher than that of commercial EDLCs, without losing the excellent power capability. In terms of ion dynamics, a model was proposed, where the increasing amount of mesopores and nitrogen doping can promote the EDLC performance only when the ion dynamics inside micropores areas are the rate-limiting factor. Ion dynamics inside mesopores commence to limit the EDLC performance at ultrahigh rates when the ratio of mesopores to micropores surpasses 3:1 in volume. Above this ratio, increase of mesopores or nitrogen doping have little influence. A small peak in the CV curves of the STCs was observed, and is ascribed to the decoordination of IL ions when filling the narrow micropores during the charging/discharging process. More importantly, there is a significant contribution to energy storage due to the ion ordering transitions of the IL electrolytes inside carbon mesopores.

As mentioned in section 2.3, to improve the energy density of supercapacitors, another static is the development of NICs, where the biggest obstacle lies in the kinetic imbalance between the cathode and anode. To develop faradic carbonaceous anodes with sufficient dynamics to match the non-faradic cathode, great efforts have been devoted to tailoring the atomic construction and porosity of carbons[91-93] which can contribute to sodium storage and promote rapid ion transport. Another promising approach is the introduction of heteroatoms, especially nitrogen, to provide additional charge storage capacity through reversible binding of sodium to the nitrogen-based functional groups.[81] The nitrogen content in these nitrogen-doped carbons is normally limited [147-150] but higher nitrogen content could further enhance the sodium storage capacity as, for example, carbon nitride has proved its extraordinary lithium capacity (933 mAh g^{-1}).[51] Although this combination of high heteroatom content and one-dimensional nanostructure is quite promising for NIC anodes, the synthetic approaches for such materials are still limited.

In addition to the development of advanced materials for NIC anodes, the mechanism of sodium storage in carbon materials is still not completely understood. The main contributions for storage capacity originate from the underpotential deposition on the high energy adsorption sites on the carbon electrode surface

such as defective sites and functional groups as well as from the intercalation into the stacked graphene layers of the carbons. Although still debated, most studies indicate that the slope region at higher voltage during discharge corresponds to adsorption of sodium ions while the capacity in the low voltage range corresponds to intercalation.[35, 94-98] For sure, there is still a lack of systematic studies and comprehensive interpretation of the mechanism of sodium storage in carbon (and especially in nitrogen-doped carbon) materials. Beyond these questions related to the fundamental storage mechanism, there remains also a lack of profound understanding about the influence of electrode properties such as heteroatom content, nanostructure/porosity of the electrode, electrical conductivity, and degree of graphitization on the capacity and rate capability of NICs. Illuminating these structure-performance relationships requires systematic studies.

Thus, to fulfill the admirable rate capability with high capacity for NIC anodes, this chapter is mainly devoted to fabricating nitrogen-rich porous carbon materials with desirable conductivity for fast electron transport and elaborate nanoarchitectures for rapid ion transport. More importantly, the mechanism of sodium storage in nitrogen-doped carbons is investigated, which is expected to act as theoretical basis to guide the future optimal design of the anode materials for NICs in the perspective of material components and architectures.

4.1.   Understanding the charge storage mechanism to achieve high capacity and fast ion storage in sodium-ion capacitor anodes by using electrospun nitrogen-doped carbon fibers

Electrospun carbon fibers have received particular attention due to their potential scalability and enhanced electrochemical performance as NIC anodes.[151-152] The latter is mainly due to their one-dimensional nanostructure with abundant interconnections between the fibers which facilitates electrical conductivity and ion transport, pushing forward the capacity beyond 300 mA h g^{-1}.[148, 151] In this

section, hexaazatriphenylene-hexacarbonitrile (HAT-CN) with high nitrogen content and polyvinylpyrrolidone (PVP) as precursors are used to electrospin a free-standing carbon fibers composite (nitrogen-doped carbon and partially graphitic carbon) film with high nitrogen contents. The free-standing carbon fibers present remarkable performance as anodes for NICs. Furthermore, the mechanism of sodium storage in this material is illuminated by adjusting the ratio of nitrogen-doped carbon and graphitic carbon domains through different condensation temperatures. A NIC full cell with HAT-CNF as the anode and highly porous salt-templated carbon (STC) is then set-up to quantify the behavior of the two storage materials. The whole data analysis is focused on mechanistic findings in terms of the sodium storage contributions to capacity as well as the importance of the one-dimensional nanostructure and the electrical conductivity for rate capability.

4.1.1.   Synthesis and characterization of nitrogen-doped carbon fibers

A series of nitrogen-doped carbon fibers (denoted as HAT-CNFs) with different nitrogen content are prepared by electrospinning employing HAT-CN mixed with the matrix polymer PVP as the precursors. Thermal condensation of this mixture results in a large volume of structural microporosity and high pyrazinic nitrogen content introduced by the molecular structure of HAT, while PVP is employed as a processing aid for electrospinning. HAT-CN is synthesized according to a previously described procedure[153-155] and dissolved in dimethylformamide (DMF) together with PVP. The precursor solution was electrospun into a fiber matrix composed of PVP and HAT-CN (**Scheme 4.1**). The HAT-CNF-700, HAT-CNF-850, and HAT-CNF-1000 are obtained by condensation of the precursor fibers under N_2 atmosphere for 1 h at 700, 850, and 1000 ℃, respectively. Thermal decomposition of PVP and condensation of HAT-CN lead to gas evolution and to the generation of roughness on the surface of the fibers (**Scheme 4.1**). TGA under N_2 (**Figure 4.1**) indicates that the residual mass of the fiber precursors is significantly higher than that of the pure HAT-CN, suggesting that HAT-CNFs contain excess carbon (likely also slightly

nitrogen-doped) derived from PVP in addition to the very nitrogen-rich product of HAT-CN condensation. This explains the lower nitrogen content of HAT-CNFs compared with that of the carbon derived from pure HAT-CN (HAT-850) at the same calcination temperature (**Table 4.1**). Elemental analysis shows that the nitrogen contents of HAT-CNF-700, HAT-CNF-850, HAT-CNF-1000 still reaches values as high as 15 wt%, 10 wt%, and 5 wt%, respectively (**Table 4.1**). Thus, from the molecular point of view, HAT-CNFs can be described as nitrogen-doped carbon materials, in which the nitrogen-doped sites can possibly act as the active sites to adsorb sodium ions for the improved capacity, while the additional carbon (mostly derived from PVP) enhances the electrical conductivity.
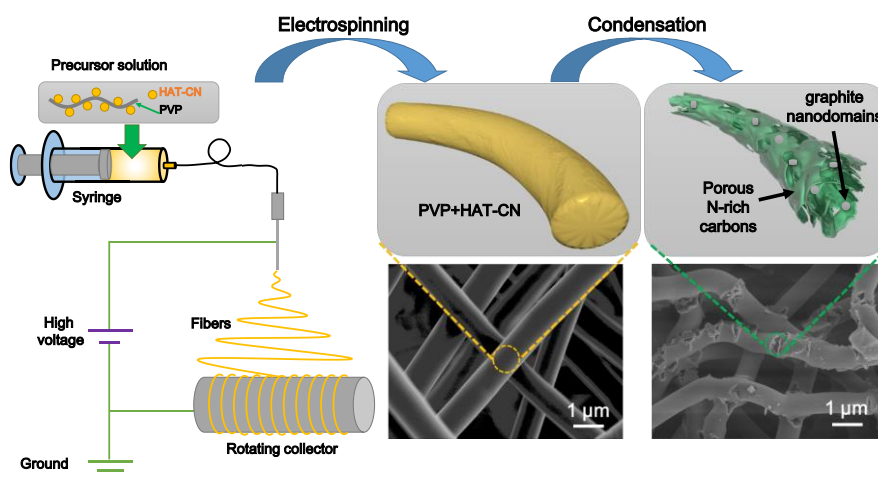
Scheme 4.1. Preparation of the porous HAT-CNF by electrospinning and subsequent condensation. .
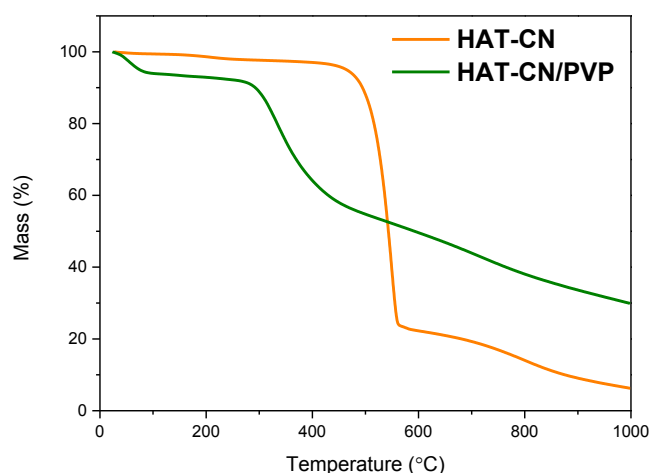
Figure 4.1. TGA curves of HAT-CN and electrospun HAT-CN/PVP under N_2.

4.   Nitrogen-rich Porous Carbons for Sodium-ion Capacitors

The carbonized fibers have a high aspect ratio and are continuous with a narrow diameter distribution as shown in the SEM images (**Figure 4.2**a-c). The diameter of the fibers decreases with the increase of the condensation temperature to ~1000 nm, 800 nm, and 400 nm for HAT-CNF-700, HAT-CNF-850, and HAT-CNF-1000, respectively (**Figure 4.2**d-e), i.e. the mass loss and the density increase are taken up by lateral shrinking. Regardless of the condensation temperature, the carbon fibers exhibit an intact one-dimensional nanostructure with abundant surface defects. This wire-like morphology is useful to provide low electric resistance, while the interstitial mesh openings enable enhanced ion transport inside the materials at the same time. The scanning electron microscopy energy dispersive X-ray spectroscopy (SEM-EDX) mapping images (insets in **Figure 4.2**a-c) reveal the uniform distribution of C and N within the fibrous framework. In agreement with the results from elemental analysis, the increase of calcination temperature results in a gradual decrease of nitrogen content (**Table 4.1**).

Table 4.1. Specific surface area (SSA), total pore volume (V_t), and nitrogen content of the carbon materials determined by elemental analysis and SEM-EDX of the HAT-CNF materials prepared at different temperatures and the non-spun HAT-850 reference sample.

Sample name	SSA (m^2/g)	V_t (cm^3/g)	Nitrogen content (EA wt%)	Nitrogen content (EDX wt%)
HAT-CNF-700	308	0.12	15	19
HAT-CNF-850	337	0.18	10	13
HAT-CNF-1000	644	0.27	5	6
HAT-850	642	0.28	17	20
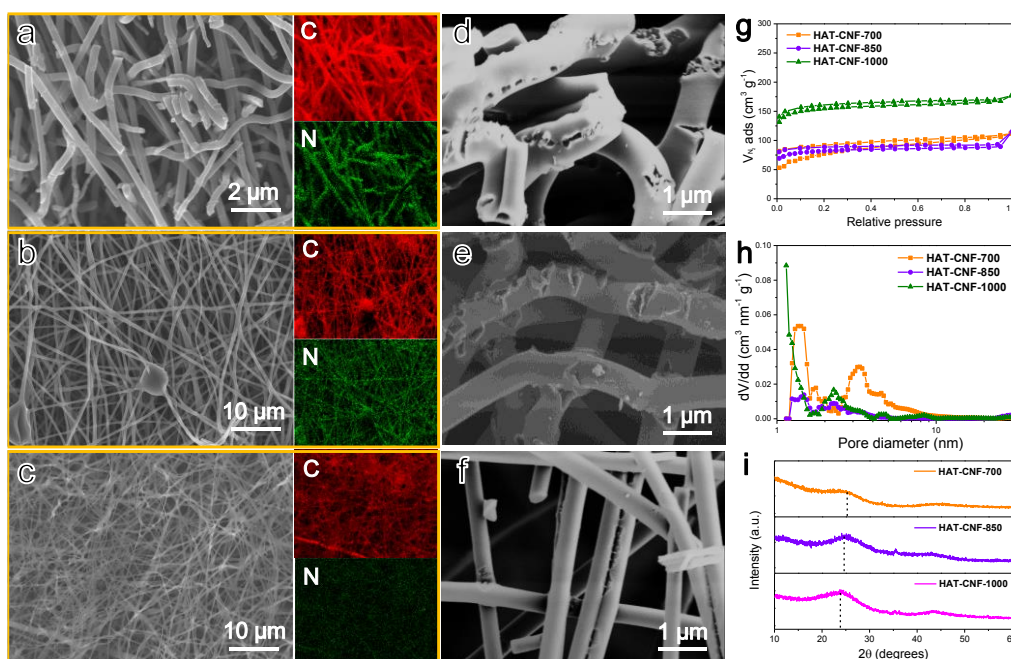
Figure 4.2. SEM images and EDX mapping (C and N) of (a) HAT-CNF-700, (b) HAT-CNF-850, and (c) HAT-CNF-1000. SEM images of (d) HAT-CNF-700, (e) HAT-CNF-850, and (f) HAT-CNF-1000 at higher magnification. (g) N_2 physisorption isotherms (at -196 ℃) with corresponding (h) differential pore size distribution of the HAT-CNFs. (i) XRD patterns of HAT-CNFs.

N_2 physisorption experiments at -196 ℃ are carried out to analyze the pore structure (**Figure 4.2g,** and **Table 4.1**). All the samples show type I(b) isotherms indicating the presence of a small amount of narrow mesopores in addition to the abundant structural micropores.[156] The SSA and the PSD are analyzed by employing the QSDFT for N_2 adsorbed on carbon with slit/cylindrical pore shape.[157] HAT-CNF-700 shows a moderate DFT SSA of 308 m^2 g^{-1}. With the increase of the temperature, the SSAs gradually increase to 337 m^2 g^{-1} and 644 m^2 g^{-1} for HAT-CNF-850 and HAT-CNF-1000, respectively (**Table 4.1**). The total pore volume exhibits the same trend, rising from 0.12 cm^3 g^{-1} for HAT-CNF-700, to 0.18 cm^3 g^{-1} for HAT-CNF-850, followed by 0.27 cm^3 g^{-1} for HAT-CNF-1000. All those values are to be considered as low, not geometrically interrupting the electron conductivity in those materials. The PSDs also confirm their mainly microporous structure and small volumes of narrow mesopores of ~3 nm in diameter (**Figure 4.2**h). XRD results (**Figure 4.2**i) of all the samples showed only broad (002) and (101) carbon peaks at ~26°and ~44°2Theta, verifying their mainly weakly ordered structure as it is typical for porous carbon

materials.[158] An increase of the condensation temperature results in more pronounced peaks with higher intensity, indicating the higher extend of graphitic stacking. It is also worth noting that the (002) carbon peak is shifted to slightly lower angles with temperature increase (~26°, 25°, and 24° for HAT -CNF-700, -850, and -1000, respectively), implying that the high temperature leads to expanded layer distance in the graphitic carbons, which should facilitate sodium intercalation.

4.1.2.   Performance as anodes for NIC and mechanism for sodium storage

HAT-CNFs are used as working electrodes for half-cell measurements in Swagelok-type test cells. Sodium foil and 1 M $NaClO_4$ in ethylene carbonate/propylene carbonate/fluoroethylene carbonate (45:45:10 by mass) are employed as the counter/reference electrode and electrolyte, respectively. The electrochemical performance of HAT-CNFs is first evaluated by GCPL process from 0.1 to 10 A g^{-1} between 0 and 2.5 V vs. Na/Na$^+$. At the low specific current of 0.1 A g^{-1}, the initial discharge capacity of HAT-CNF-700, -850, and -1000 is 875, 828, and 409 mAh g^{-1}, while the corresponding initial charge capacity decreases to 424, 381, and 218 mAh g^{-1} (**Figure 4.3**a-c), resulting from the typical irreversible processes in the initial cycles due to the formation of a solid-electrolyte interphase (SEI) as well as the possible irreversible trapping and consumption of sodium.[84, 159]
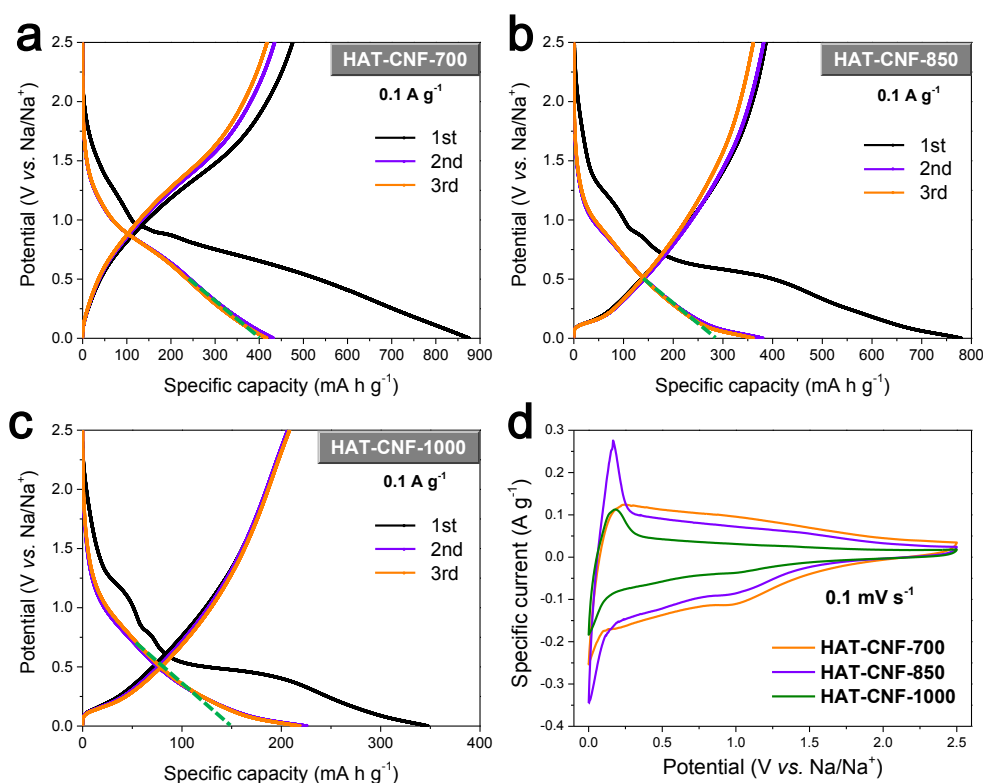
Figure 4.3. Half-cell tests of HAT-CNFs. Galvanostatic charge-discharge profiles of the first cycles of (a) HAT-CNF-700, (b) HAT-CNF-850, and (c) HAT-CNF-1000. (d) Cyclic voltammetry curves of HAT-CNFs scanned at the rate of 0.1 mV s^{-1}.

In the subsequent cycles, all the discharging curves show a very sharp slope region in the high underpotential range of 1.2-2.5 V, which likely corresponds to binding of sodium on specific well-stabilized sites on the porous and defect-rich HAT-CNF surface. When the potential decreases to 0.3-1.2 V, the slope of the curve decreases, and the capacity in this region depends about linear on the nitrogen content (420, 298, and 146 mAh g^{-1} for the 15 wt%, 10 wt%, and 5 wt% nitrogen content, respectively, as revealed by the intercept of the green dashed line with the capacity axis in **Figure 4.3**a-c). The capacity in this range can be attributed to the reversible binding of sodium species on nitrogen-containing sites, which mainly originates from the nitrogen-doped carbon components in the fiber composite. The introduction of nitrogen-containing sites seem to significantly increase the ability for underpotential deposition or intercalation of sodium atoms onto special, highly ligating sites in the porous doped carbon. An underpotential of 1 V therein

corresponds to an adsorption enthalpy of 100 kJ mol^{-1}. This roughly corresponds to the enthalpy of evaporation of metallic sodium, i.e. the sodium interacts with these positions at least as strong as with its own counterparts. Similar effects are widely known from the field of gas adsorption where carbons with high heteroatom content show zeolite-like properties and rather strong adsorption enthalpies to polar molecules, which is here expressed in an electrochemical underpotential (according to the Nernst equation).[155, 160-161] As zeolites are known for their strong interaction with alkali metal ions, it is not surprising that highly polar HAT-CNFs show high adsorption capacity for sodium. For instance, the adsorption capacity of 420 mAh g^{-1} for HAT-CNF-700 would translate to a sodium adsorption capacity of 15.7 mmol$_{Na}$ g^{-1} - a value that nicely compares to the water adsorption capacity of such materials.[155, 162] Assuming an overall stoichiometry of HAT-CNF-700 of $C_{0.87}N_{0.13}$ (based on the elemental analysis data), the nitrogen content of ~10.6 mmol$_N$ g^{-1} is apparently closely related to the sodium storage capacity. Assuming that all the sloped capacity is due to binding of sodium near nitrogen, one nitrogen atom in HAT-CNF-550 relates to 1.5 sodium atoms. Interestingly, for HAT-CNF-850 ($C_{0.913}N_{0.087}$) and for HAT-CNF-1000 ($C_{0.957}N_{0.043}$) these values are still very close to 1.5, indicating that the sodium storage capacity in the slope region indeed precisely scales with the nitrogen content.

On the other hand, there are distinct differences in the low potential range. Typical plateaus are observed in the curves of HAT-CNF-850 and HAT-CNF-1000 at 0-0.3 V, while the curve of HAT-CNF-700 keeps a constant slope shape in this range. This is consistent with the increased degree of carbon layer stacking and the expanded interlayer distance in the more graphitic carbons as revealed by the XRD data, which enables a possible intercalation of sodium ions. CV curves at the scan rate of 0.1 mV s^{-1} (**Figure 4.3**d) further confirm this interpretation. HAT-CNF-850 and -1000 exhibit pronounced peaks at around 0.2 V caused by the reversible intercalation/deintercalation of sodium ions, while the rest of the curves is rather

capacitive-type, representing the underpotential deposition of sodium species on specific binding sites. In summary, the mechanism of sodium storage in these N-rich HAT-CNF materials with partial graphitic stacking can be divided as follows. In the high and medium underpotential range, sodium is stored through deposition on low energy sites with high stabilization. In the low potential range, the intercalation of sodium ions into the carbon interlayers comes into play, which depends on the degree of graphitization and interlayer distance (**Scheme 4.2**).
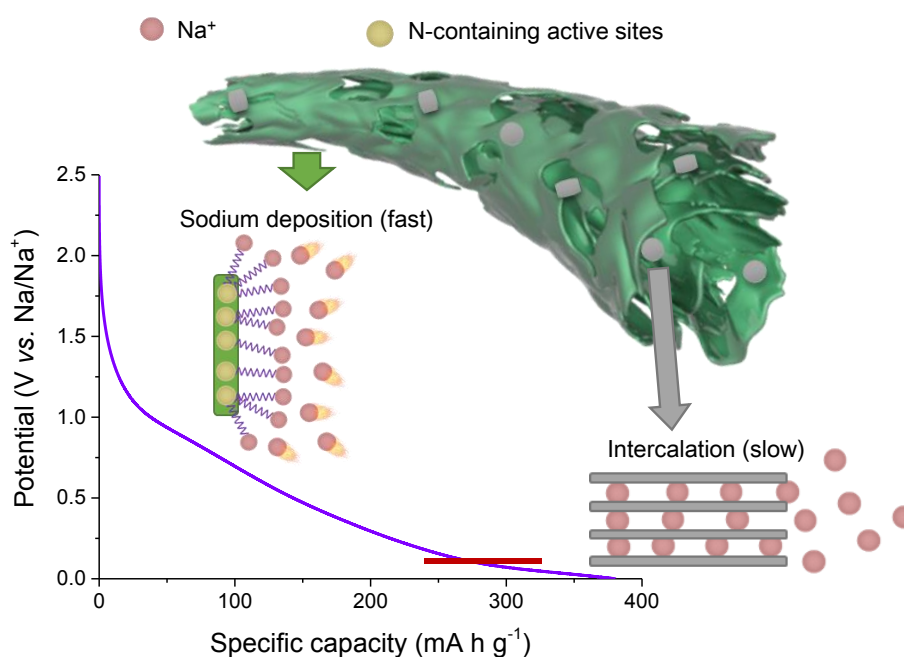
Scheme 4.2. Proposed mechanisms of the sodium storage in the nitrogen-doped carbon fibers.

The reversible capacities at a specific current of 0.1 A g^{-1} of HAT-CNF-700, HAT-CNF-850, and HAT-CNF-1000 determined after 40 cycles are as high as 395 mAh g^{-1}, 361 mAh g^{-1}, and 209 mAh g^{-1}, respectively (**Figure 4.4**d). It is also worth noting that despite the highest SSA, HAT-CNF-1000 provides the lowest capacity, suggesting that the SSA and micropore volume have less influence on the sodium storage than nitrogen content.
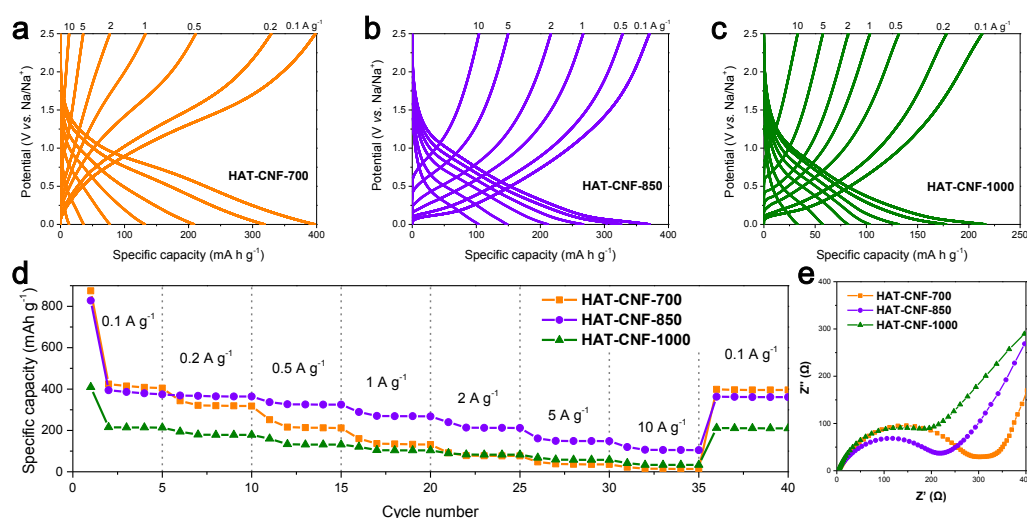
Figure 4.4. Half-cell tests of HAT-CNFs. Galvanostatic charge-discharge profiles at different specific currents of (a) HAT-CNF-700, (b) HAT-CNF-850, and (c) HAT-CNF-1000. (d) Rate performance of HAT-CNFs at different specific currents. (e) Nyquist plot of HAT-CNFs.

The rate capability is examined by varying the specific current in the range of 0.1 to 10 A g^{-1} (**Figure 4.4**a-d). All the samples show the typical decay of capacity with the increase of current, while the rate performance is related to the condensation temperature. At 10 A g^{-1}, the specific capacity of HAT-CNF-700, -850, and -1000 is 13.6, 106, and 33.2 mAh g^{-1}, respectively, corresponding to retention of 3.4%, 29.3%, and 15.9%. The inferior rate capability of HAT-CNF-700 can be ascribed to the comparably low electrical conductivity (**Figure 4.4**e). The moderate rate capability of HAT-CNF-1000 is likely to be attributed to the rather large contribution of intercalation to the sodium ion storage, which is a relatively sluggish process and does not significantly contribute at high rates (**Figure 4.4**c). Therefore, despite its better conductivity, the rate capability is still worse than that of the HAT-CNF-850. The rate capability is to be complemented by the Nyquist plots (**Figure 4.4**e). All the samples exhibit a semicircle curve in the high frequency region plus a straight line in the low frequency region, which is a typical impedance curve for battery materials. Basically, the diameter of the semicircle represents the interfacial charge transfer resistances, which mainly come from the electric and ionic resistances at the interface between the electrode and the electrolyte in a specific process. The

smallest semicircle for HAT-CNF-850 suggests its lowest resistance at favorable processes, leading to the superior rate capability. To summarize, the rate capability depends on the dynamics of the electron and ion transport. The HAT-CNF-700 lacks sufficient electrical conductivity for electron transport, while the HAT-CNF-1000 suffers from the sluggish ion transport dynamics at high rates due to the relatively large portion of intercalation process.

Among these HAT-CNFs, HAT-CNF-850 provides the best overall performance, exhibiting a reversible specific capacity of 361, 269, 149, and 105 mAh g^{-1} at 0.1, 1, 5, and 10 A g^{-1}, respectively. Such a superior capacity and rate capability is attributed to the desirable conductivity, high nitrogen content, fibrous morphology, and high porosity within the fiber surface. The high nitrogen content provides abundant low energy sites for sodium storage, while the graphitic carbon component can accommodate the intercalation of sodium atoms, both giving rise to the capacity. In terms of rate capability, the wide pores of the fibrous structure shortens the transport length of sodium ions, The slow process of intercalation accounts for only a small part of the whole capacity due to the rather low portion of graphitic carbon component. These two factors plus the desirable electrical conductivity result in its excellent rate capability. The high cycling stability of HAT-CNF-850 is verified by cycling tests, which maintain over 95% of the initial capacity after 500 deep charging-discharging cycles at 0.5 A g^{-1}, indicating sufficient electrochemical stability of the material throughout cycling (**Figure 4.5**).
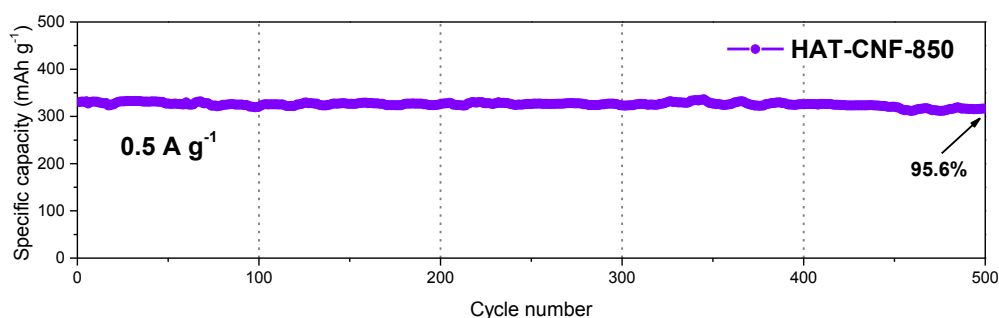
Figure 4.5. Cycling test of HAT-CNF-850 at 0.5 A g^{-1} for 500 cycles.

4. Nitrogen-rich Porous Carbons for Sodium-ion Capacitors

To investigate the influence of the fibrous structure, HAT-CN as such was directly carbonized at 850 ℃ (HAT -850) with the same procedure of HAT-CNF-850, and employed as electrode material for the half-cell measurements. The nitrogen content of HAT-850 is ~17 wt% as determined by elemental analysis (**Table 4.1**), thus slightly higher than that of the (also PVP-based) HAT-CNF-850. SEM and TEM images reveal a plate-like morphology of HAT-850 with a particle size of around 10 µm, and the typical disordered microporous structure with a small contribution of mesopores (**Figure 4.6**a-b). The XRD pattern shows that its local structure is comparable to that of the HAT-CNF-850 (**Figure 4.7**a). In the N_2 (-196 ℃) physisorption experiments, HAT-850 shows a type I(a) isotherm, indicating a porous structure similar to the HAT-CNFs with a slightly higher DFT SSA of 642 m^2 g^{-1} (**Figure 4.7**b). The increase of the SSA is attributed to the absence of PVP. When employing HAT-850 as the working electrode for sodium ion storage, the initial specific discharge and charge capacity is 390 and 168 mAh g^{-1} at 0.1 A g^{-1} (**Figure 4.7**d), corresponding to an initial coulombic efficiency of 43%. It provides only a moderate reversible specific capacity of 161 mAh g^{-1} at 0.1 A g^{-1} (**Figure 4.6**c and f), which is 50% less than HAT-CNF-850 (361 mAh g^{-1}) in spite of the higher nitrogen content and higher porosity of HAT-850. Moreover, the intercalation mechanism that significantly contributes to the capacity of HAT-CNF-850 is absent in HAT-850, which is also revealed by the absence of the pronounced peaks at around 0.2 V (**Figure 4.6**d). HAT-850 also shows relatively inferior rate capability with a specific capacity of 86, 35, and 15 mAh g^{-1} at 1, 5, and 10 A g^{-1}, respectively (**Figure 4.6**c and f). All this can be attributed to the fibrous morphology of the electrospun counterpart, which provides one-dimensional conduction pathways, but also lower lateral dimensions for ion transport perpendicular to the fiber. The superior rate capability of HAT-CNF-850 is also elucidated by the smaller semicircle (lower resistance) in the Nyquist plot (**Figure 4.6**e).
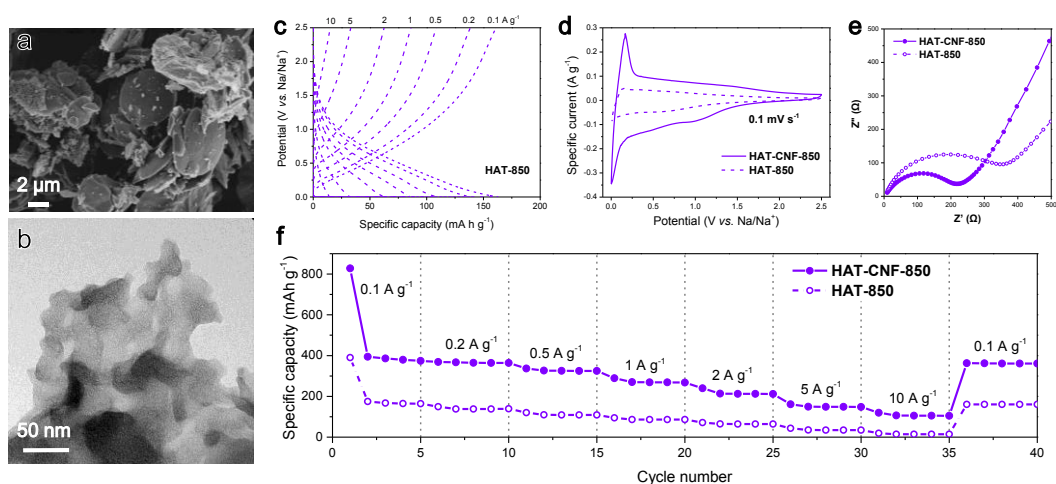
Figure 4.6. (a) SEM and (b) TEM images of HAT-850. (c) Galvanostatic charge-discharge profiles of HAT-850 at different specific currents. (d) Cyclic voltammetry curves, (e) Nyquist plot, and (f) rate performance of HAT-850 in comparison with those of HAT-CNF-850.
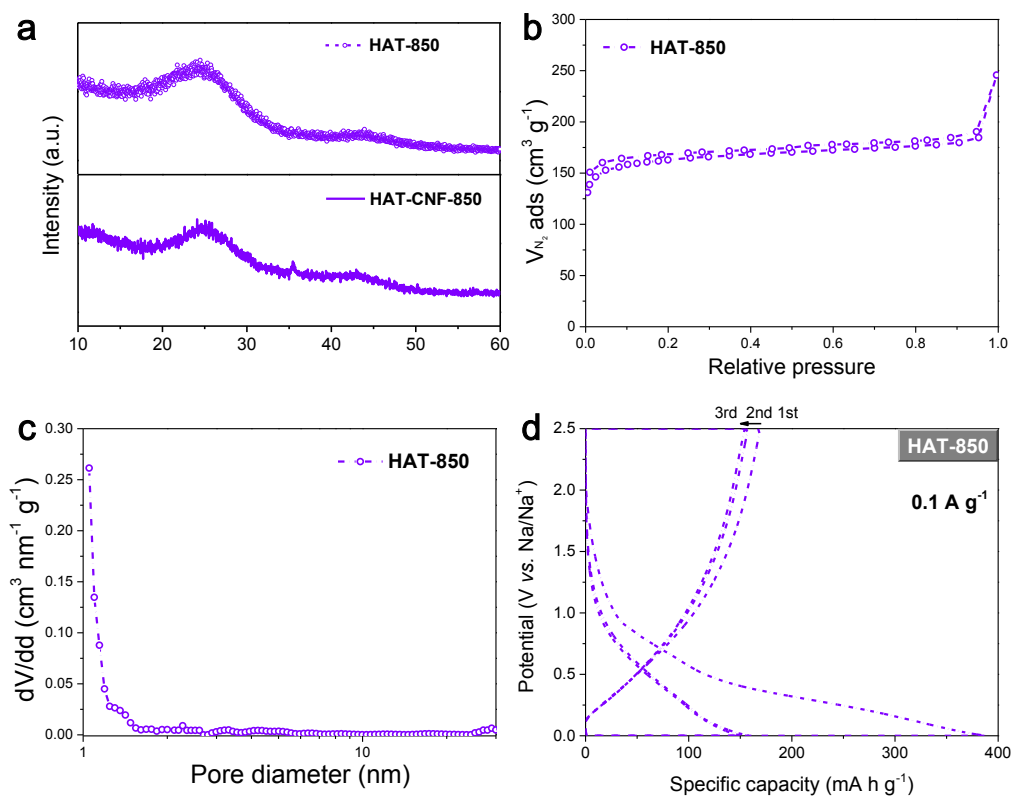
Figure 4.7. (a) XRD patterns of HAT-850 and HAT-CNF-850. (b) N_2 physisorption isotherms (at -196 ℃) with its corresponding (c) differential pore size distribution of HAT-850. (d) Galvanostatic charge-discharge profiles of the initial three cycles of HAT-850 at 0.1 A g^{-1}.

4. Nitrogen-rich Porous Carbons for Sodium-ion Capacitors

To verify the practical applicability of the electrospun HAT-CNF-based electrodes, a prototype NIC full cell is fabricated with the HAT-CNF-850 and salt-templated carbon (STC-16) as the anode and cathode, respectively. STC-16 with hierarchical micro- mesopore architecture has recently been identified as an excellent supercapacitor electrode material.[163] It exhibits good performance as a cathode material in the half-cell NICs with metallic sodium as the counter electrode. The reversible capacity of STC-16 reaches up to 70 mAh g^{-1} at 0.1 A g^{-1} within the voltage range of 3.2 to 4.4 V (**Figure 4.8**a). The capacity loss in the first cycle can again be attributed to the irreversible side reactions between the carbon surface functional groups and the electrolyte at high cell voltage (4.4 V) and the related high oxidation potentials of + 1.5 V, creating an solid electrolyte interphase layer by reaction with the solvent. Both cathode and anode were activated before assembling into the full cell. The anode is cycled for 10 times at 0.1 A g^{-1}, followed by discharging to 0 V to achieve full sodiation. Similarly, the cathode is cycled for 10 times before charging to 4.4 V. The HAT-CNF-850||STC16 full cell is measured with the working voltage cut offs between 0.5 V and 4 V to maximize the utilization of the working potential range of both electrodes and minimizing the risk of electrolyte decomposition or other oxidative side reactions. The nearly rectangular shape of CV curves up to 200 mV s^{-1} (**Figure 4.8**b), the almost symmetric triangle shape of the GCPL curves (**Figure 4.8**c inset), as well as the practically vertical curves in the low-frequency region of the Nyquist plots (**Figure 4.9**a) indicate a capacitive-controlled behavior of the NIC. However, slight distortions from the perfect capacitive shape of these curves are likely caused by the non-capacitive intercalation of Na$^+$ into the HAT-CNF-850 anode. Calculated by the galvanostatic charging/discharging curves, the specific capacitance of the NIC full cell reaches 55.8 F g^{-1} at a specific current of 0.1 A g^{-1}, while it maintains high values of 40, 32, 20, and 15 F g^{-1} at 1, 2, 5, and 10 A g^{-1}, respectively (**Figure 4.8**c). This is also confirmed by the small voltage drop of 0.54 V even at the high specific current of 10 A g^{-1} (**Figure 4.8**c inset). The superior rate

capability is attributed to efficient charge carrier transfer, which is also revealed by the Nyquist plot (**Figure 4.9**a). The small intercept along the real axis (5 Ω) and the minor semicircle illustrate the low intrinsic resistance and high electrical conductivity in both cathode and anode. In the medium frequency region, the short Warburg lengths (the 45° sloped curve) indicate good ion transport dynamics and short ion transfer distance, which can be attributed to the 1D fiber structured anode. Accordingly, the Ragone plot (**Figure 4.8**d) of the NIC shows that the asymmetric cell with the voltage window of 0.5-4.0 V provides the maximum specific energy of 95 Wh kg^{-1} at a specific power of 0.19 kW kg^{-1}, with a slight drop to 65 Wh kg^{-1} at 1.8 kW kg^{-1}, and still maintains 18 Wh kg^{-1} at a specific power of 13 kW kg^{-1}. The specific energy is indeed one order of magnitude higher than that of commercial EDLCs without losing the excellent power capability. The performance of HAT-CNF-850||STC16 NIC device can be compared with some recently reported outstanding devices in a Ragone plot (**Figure 4.8**d). The metal-free electrodes and non-optimized NIC device exhibits competitive energy/power performance comparable to state-of-the-art NICs, such as PI-2.5//AC(PI-5),[164] Na-Ti$_3$C$_2$//AC,[165] TiO$_2$@CNT@C//BAC,[166] Na$_2$Ti$_2$O$_4$(OH)$_2$||RHDPC-KOH,[167] and M-TiO$_2$-RGO||PDPC.[168] The cycling stability was tested in a cycling test at a specific current of 1 A g^{-1}. After 1000 cycles, a specific capacitance of 34.4 F g^{-1} is maintained corresponding to capacitance retention of 89.9% (**Figure 4.9b**). The ~10% capacity loss might be related to the large voltage window that causes the degradation in the positive potential range.[169] The Coulombic efficiency is nearly 100% throughout the cycling process, showing the reversibility of the NIC. Thus, this NIC set-up demonstrates a much higher energy density compared to commercial EDLCs, as well as comparable power density and cycling life, showing great potential as an alternative candidate for future high power electrochemical energy storage.
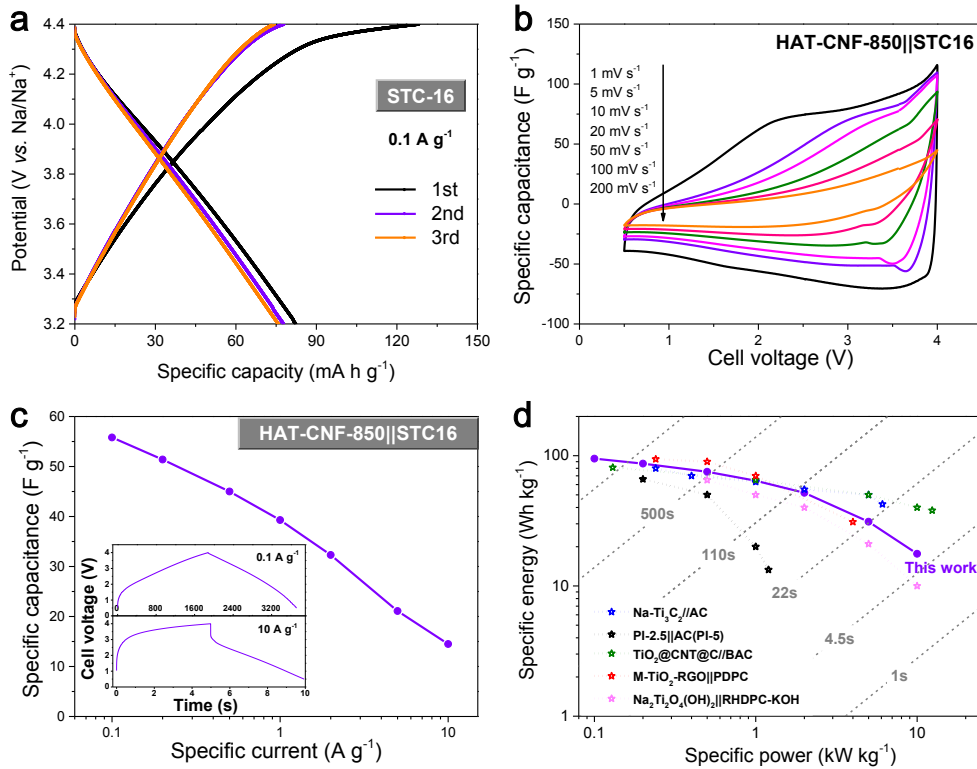
Figure 4.8. Full-cell test of the NIC with HAT-CNF-850 as anodes and STC-16 as cathodes. (a) Galvanostatic charge-discharge profiles of the initial three cycles of STC-16 at 0.1 A g^{-1} as the cathode in a half cell. (b) Cyclic voltammetry curves (0.5-4.0 V), (c) Nyquist plot, (c) capacitance retention with specific current increase, and (d) Ragone plots, and (f) cycling test of the NIC full cell. The inset in (c) represents the galvanostatic charge-discharge profiles of the NIC full cell at 0.1 A g^{-1} and 10 A g^{-1}, respectively.
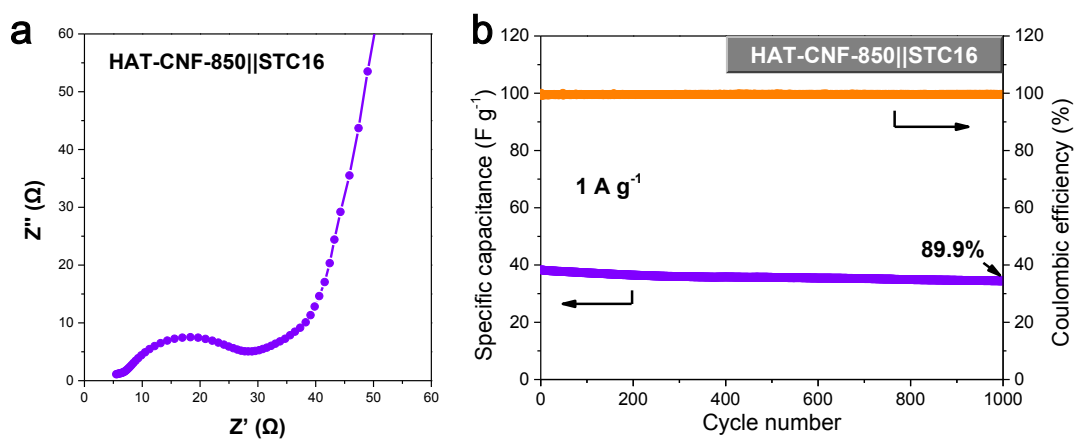
Figure 4.10. (a) Nyquist plot, and (b) cycling test of the NIC full cell.

4. Nitrogen-rich Porous Carbons for Sodium-ion Capacitors

In summary, free-standing fibrous nitrogen-doped carbon materials with the nitrogen content of up to 15 wt% were manufactured by electrospinning of HAT-CN with PVP followed by thermal condensation. The binder-free HAT-CNF-850 electrode delivered a reversible capacity of 361 mAh g^{-1} at 0.1 A g^{-1}. A remarkable capacitance of 106 mAh g^{-1} was retained at the high specific current of 10 A g^{-1}. The material also exhibited an excellent stability of 316 mAh g^{-1} at 0.5 A g^{-1} after 500 cycles, corresponding to more than 95% of the initial capacity. The superior capacity and rate capability can be attributed to the high and uniform nitrogen doping introduced by the HAT-CN precursor, as well as the high electrical and ionic conductivity of the 1D interconnected fibrous structure. The abundant nitrogen-containing groups provide active sites for sodium deposition, which takes place in the high and medium potential range and most significantly contributes to the high capacity. The more graphitic carbon domains at higher condensation temperatures can contribute by the intercalation of sodium in the low potential range below ~0.3 V versus Na/Na$^+$, a process which is highly dependent on the degree of graphitization and layer distance. Sodium deposition shows significantly faster dynamics than the intercalation process. The full cell device of NIC employing HAT-CNF as the anode and STC-16 as the cathode provides a specific energy up to 95 Wh kg^{-1}, and maintains 18 Wh kg^{-1} at a specific power of 13 kW kg^{-1} in the voltage range of 0.5-4.0 V.

4.2. Nitrogen-rich carbon nanoparticles embedded in conductive mesoporous carbon matrix as fast anodes for high-performance sodium-ion capacitors

In the former section, it is deduced that the sodium deposition is deduced to have significantly faster dynamics than the intercalation process (a rather kinetically sluggish process). Therefore, a possible next step is to further improve the nitrogen content to increase the amounts of available deposition sites, while maintaining the high electrical conductivity and elaborate pore structure design for fast electron and ion transfer. Ideally, a nitrogen-doped carbon-carbon composite material would have a conductive carbon backbone in close proximity with a nitrogen-rich surrounding for sodium storage. In this way, the potential of the sodium deposition process can be fully exploited to ensure the high capacity and good rate capability. Therefore, in this section, a mesoporous carbon (ZnO templated carbon, ZTC) is employed as a conductive matrix to host nitrogen-rich carbon nanoparticles obtained by condensation of HAT-CN precursors to fabricate a composite material (nitrogen-rich carbon combined with the conductive carbon matrix, HAT550@ZTC). The composite material stands out by a high nitrogen content of up to 26 wt% induced by the HAT550 component, desirable conductivity due to the ZTC conductive matrix, and elaborate nanostructure. The HAT550@ZTC-based electrode shows an appreciable rate capability even at a specific current of 20 A g^{-1}. A full cell device of NIC employing HAT550@ZTC as the anode and STC-16 as the cathode provides high energy and power density as well as long cycle life.

4.2.1. Synthesis and characterization of HAT550@ZTC

ZTC is prepared by employing ZnO nanoparticles (20 nm) as hard templates for well-defined mesopores (**Scheme 4.3**). Sucrose is dissolved in aqueous solution, where certain amounts of ZnO nanoparticles aree dispersed. Then the carbohydrate was polycondensed at 160 ℃ with the hard template inside. Afterwards, the mixture is carbonized at 950 ℃ under inert gas. During the calcination process, Zn O reacts

with carbons through carbothermal reaction carbothermal reduction according to the following reaction (Equation (4.1)).

$$ZnO + C \rightarrow Zn + CO \tag{4.1}$$

The pyrolysis temperature above the boiling point of zinc leads to its release through the gas phase. Together with the release of CO gas, it gives rise to the generation of micropores which are in direct connection with the mesopores. Therefore, the ZTC can be seen as hierarchical porous carbons with well-defined mesopores and large amounts of micropores. To completely remove the residue inorganic Zn and/or ZnO and purify the porous carbon, the product is washed with diluted hydrochloric acid. HAT-CN is synthesized according to a previously described procedure.[153-155] Afterwards, HAT-CN (with the volume equivalent to the pore volume of ZTC) is dissolved in DMF (with the lowest amount for dissolution of HAT-CN) to impregnate the ZTC. After drying under vacuum, the mixture was calcinated at 550 ℃ unde r N_2 to condense the HAT-CN (**Scheme 4.3**). HAT-CN itself is also condensed with the same condition as a reference sample (HAT550). Thermal condensation of HAT-CN can result in a large volume of structural microporosity with the BET SSA of 617 $m^2\,g^{-1}$, and high pyrazinic content introduced by its molecular structure. According to the elemental analysis, the nitrogen content of HAT550@ZTC reaches values as high as 26 wt% (**Table 4.2**), lower than that of pure HAT550 (39 wt%) due to the nitrogen-free ZTC component. Accordingly, the ratio of HAT550 component in the HAT550@ZTC is calculated to be ~67%. This is consistent with the yield of ~50% for HAT550 derived from HAT-CN, where the mass ratio of HAT550 to ZTC is supposed to be 2:1 starting from the ratio of 4:1 for HAT-CN to ZTC. EDX-mapping further confirms the high content and homogeneous distribution of N in the HAT550@ZTC and HAT550 samples (**Figure 4.11**). Thus, from the molecular point of view, HAT550@ZTC can be regarded as a composite material, in which the nitrogen-doped sites in the nitrogen-rich carbon component (HAT550) can act as the active sites to adsorb sodium ions for the improved capacity, while

the nitrogen-free ZTC component enhances the electrical conductivity. Moreover, such chemical synthetic approach ensures strong bonding and close contact between the semiconductor HAT550 and the conductive ZTC, which promotes the electron transport inside the whole composite.
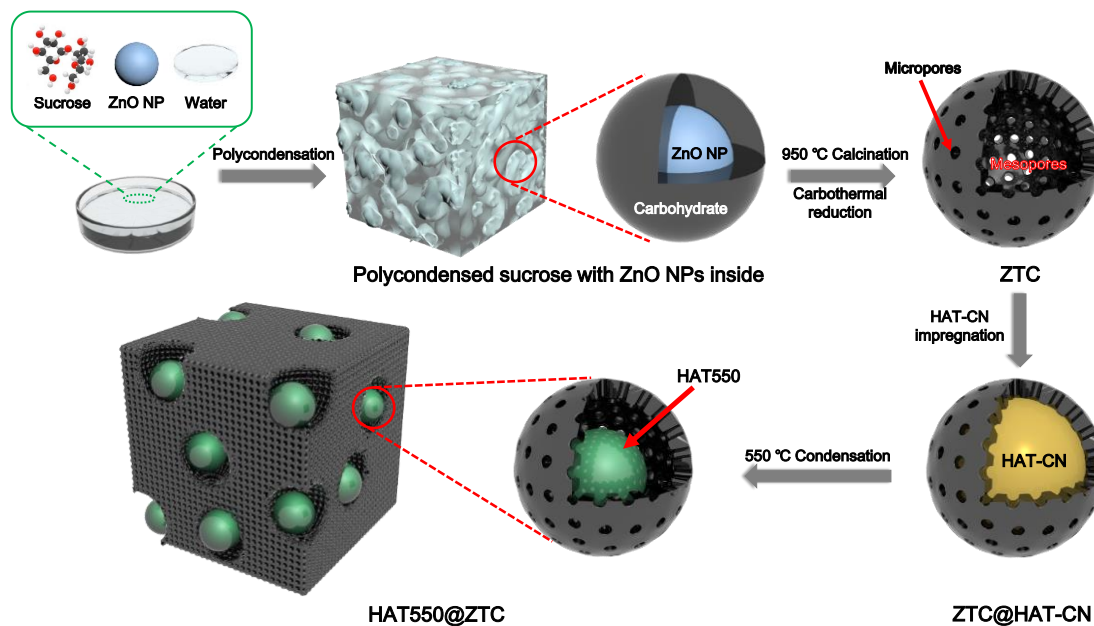
Scheme 4.3. Preparation of the HAT550@ZTC.
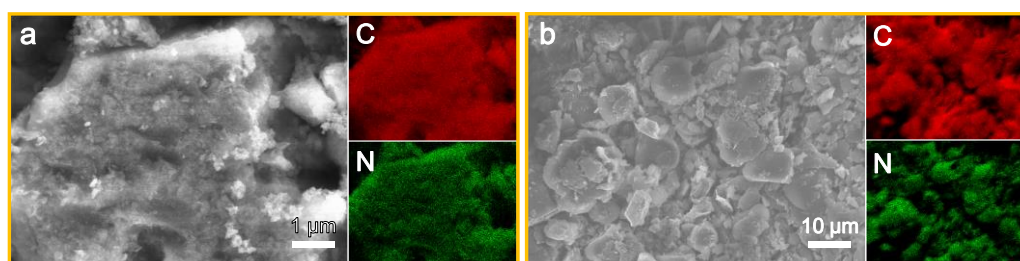
Figure 4.11. SEM images and EDX mapping (C and N) of (a) HAT550@ZTC, and (b) HAT550.

4. Nitrogen-rich Porous Carbons for Sodium-ion Capacitors

Table 4.2. BET SSA, total pore volume (V_t), and nitrogen content of the carbon materials determined by elemental analysis, as well as the ratio of HAT550 carbon of HAT550@ZTC and the reference samples of HAT550 and ZTC.

Sample name	SSA (m^2/g)	V_t (cm^3/g)	Nitrogen content	HAT550 wt%
HAT550@ZTC	415	0.6	26 wt%	67 wt%
HAT550	671	0.3	39 wt%	100 wt%
ZTC	1762	2.9	/	0

XRD results (**Figure 4.12**a) of all the samples showed only broad (002) and (101) carbon peaks at ~26°and ~44°2Theta, verifying their mainly amorphous structure with pronounced disorder. It is worth noting that the graphitization degree of ZTC is the lowest as revealed by the smallest XRD peaks. Incorporating with the HAT550 component gives rise to the drastic elevation of the XRD peaks (HAT550@ZTC), similar to that of the HAT550 sample, implying the successful combination of the HAT550 component with the matrix ZTC in the HAT550@ZTC sample. N_2 physisorption experiments at -196 °C are carried out to analyze the pore structure (**Figure 4.12**b-c, and **Table 4.2**). HAT550 shows the typical type I(a) isotherm indicating the mainly microporous structure.[156] ZTC exhibits type IV(a) isotherm with a continuous slope above a relative pressure of 0.2, and a narrow hysteresis loop with near-parallel shape in the relative pressure range between 0.8 and 1.0 (**Figure 4.12**b), suggesting the existence of well-defined mesopores with large amounts of micropores. After loading HAT550, HAT550@ZTC shows the same type of isotherm (**Figure 4.12**b) compared with the pristine ZTC, indicating the unchanged hierarchical pore structure. On the other hand, there appears to be an apparent drop of the adsorbed N_2 amount, giving rise to the drastic decrease of SSA and total pore volume from 1762 m^2 g^{-1} and 2.9 cm^3 g^{-1} (HAT550@ZTC) to 415 m^2 g^{-1} and 0.6 cm^3 g^{-1} (ZTC), respectively, suggesting the pore blocking from the HAT550 component. The PSDs are analyzed by employing the QSDFT for N_2

adsorbed on carbon with slit/cylindrical pore shape (**Figure 4.12c**).[157] As expected, HAT550 only shows the pore size in the micropore region. HAT550@ZTC and ZTC have both micropores and mesopores with similar diameters but different amounts, consistent with their isotherms. The notable content of mesopores of HAT550@ZTC is caused by the shrinkage of HAT-CN precursor during condensation (**Scheme 4.3**). Thus, from all these physisorption results, it is deduced that the HAT550 was successfully embedded in the nanopores of ZTC.

The morphology of the prepared samples were characterized by SEM and TEM techniques (**Figure 4.12**d-l). Basically, HAT550 shows the large plate-like morphology with the particle size of around 10 µm (**Figure 4.12**g-h), and typical disordered microporous structure revealed by the TEM image (**Figure 4.12**i). In comparison, ZTC exhibits a more coarse morphology with abundant nanopores (**Figure 4.12**j-k), while the loose feature in the TEM image (**Figure 4.12**l) indicates the presence of large amounts of mesopores derived from the ZnO nanoparticle templates, in accordance with the N_2 physisorption results. In the case of HAT550@ZTC, it shows the comparable coarse morphology with plenty of nanopores similar to ZTC (**Figure 4.12**d). But in the higher-resolution SEM image (**Figure 4.12**e), the ubiquitous HAT550 nanoparticles all over the pores of ZTC matrix can clearly be observed. This is further identified by the TEM image (**Figure 4.12**f), where the rather dense structure suggests that the ZTC nanopores (**Figure 4.12**l) are mostly filled by the HAT550 nanoparticles. Compared with the large plate-like particles of HAT550 itself (**Figure 4.12**g-i), the HAT550 nanoparticles in HAT550@ZTC are supposed to significantly promote the accessibility of the interior active materials to the Na^+, thus improving both the capacity and rate capability. The formation of nanoparticles is attributed to the confinement effect of the ZTC nanopores. Typically, the quasi incipient wetness impregnation of ZTC with HAT-CN precursor and the subsequent vacuum drying ensure the encapsulation of the HAT-CN nanoparticles inside the ZTC nanopores (**Scheme 4.3**). During the condensation

process, the HAT-CN nanoparticles are confined in these pores with little aggregation, turning into the HAT550 nanoparticles. Meanwhile, they undergo slight shrinkage and leave out some spare space in the mesopores (consistent with the N_2 physisorption result of HAT550@ZTC), which can act as the electrolyte reservoir for rapid ion transport.
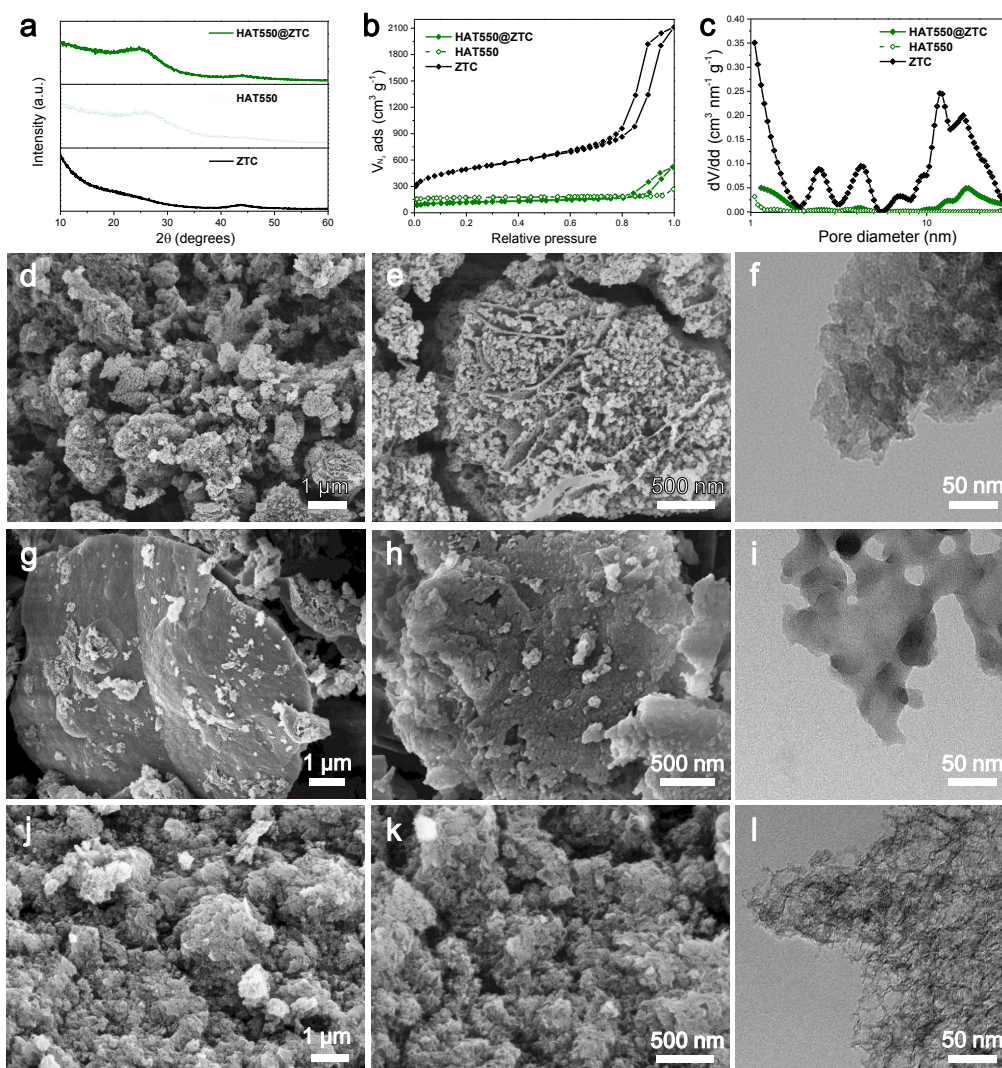
Figure 4.12. (a) XRD patterns, and (b) N_2 physisorption isotherms (at -196 ℃) with corresponding (c) differential pore size distribution of HAT550@ZTC, HAT550, and ZTC. SEM and TEM images of (d-f) HAT550@ZTC, (g-i) HAT550, and (j-l) ZTC.

4.2.2. Half-cell and full-cell test of the sodium-ion capacitor

The prepared samples are fabricated into electrodes by adding conductive additive and binder for half-cell measurements in Swagelok-type test cells. Sodium foil and

4. Nitrogen-rich Porous Carbons for Sodium-ion Capacitors

1 M NaClO$_4$ in ethylene carbonate/propylene carbonate/fluoroethylene carbonate (45:45:10 by mass) are employed as the counter/reference electrode and electrolyte, respectively. Their electrochemical performance is firstly evaluated by GCPL process from 0.1 to 20 A g^{-1} between 0 and 2.5 V. At the low specific current of 0.1 A g^{-1}, the initial discharge capacity of HAT550@ZTC, HAT500, and ZTC reaches 988, 500, and 2492 mAh g^{-1}, while the corresponding initial charge capacity decreases to 460, 246, and 253 mAh g^{-1}, corresponding to the moderate initial coulombic efficiency (CE) of 47%, 51%, and 8.6%, respectively (**Figure 4.13**a-c). It is mainly caused by the typical irreversible processes in the initial cycles due to the formation of a SEI as well as the possible irreversible trapping of sodium ions.[84, 159] Therefore, the highest SSA of ZTC leads to the largest amount of SEI, resulting in the lowest initial CE. The reversible capacities at a specific current of 0.1 A g^{-1} of HAT550@ZTC, HAT500, and ZTC determined after 40 cycles are 343 mAh g^{-1}, 210 mAh g^{-1}, and 122 mAh g^{-1}, respectively (**Figure 4.14**d). Apparently, despite the highest SSA, ZTC provides the lowest capacity, implying that the SSA has less influence on the sodium ion storage than nitrogen contents. Moreover, the shape of the CV curve of HAT550@ZTC is similar to that of the HAT550, while quite different from that of the ZTC (especially in the voltage range from 0.2 V to 2.0 V, **Figure 4.13d**), suggesting the different Na$^+$ storage mechanisms of N-rich carbons and hard carbons. Indeed, the N-containing groups can act as the active sites for the reversible binding of the Na$^+$ (chemical adsorption) for the additional capacity besides the defect-induced capacity in hard carbons. On the other hand, the capacity of HAT550 (210 mAh g^{-1}) is much inferior to that of HAT550@ZTC (343 mAh g^{-1}). And if the contribution of the ZTC capacity is further subtracted from that of the composite material, the capacity of pure HAT550 nanoparticles will reach up to 453 mAh g^{-1}, more than twice that of the pristine HAT550. This is ascribed to the superior accessibility of deposition sites of the HAT550 nanoparticles to sodium species, as compared with the pristine HAT550 where abundant active sites inside

the large particles tend to be unavailable even at such quasi-equilibrium state because of the long and non-directional transport pathways for the charge carriers.
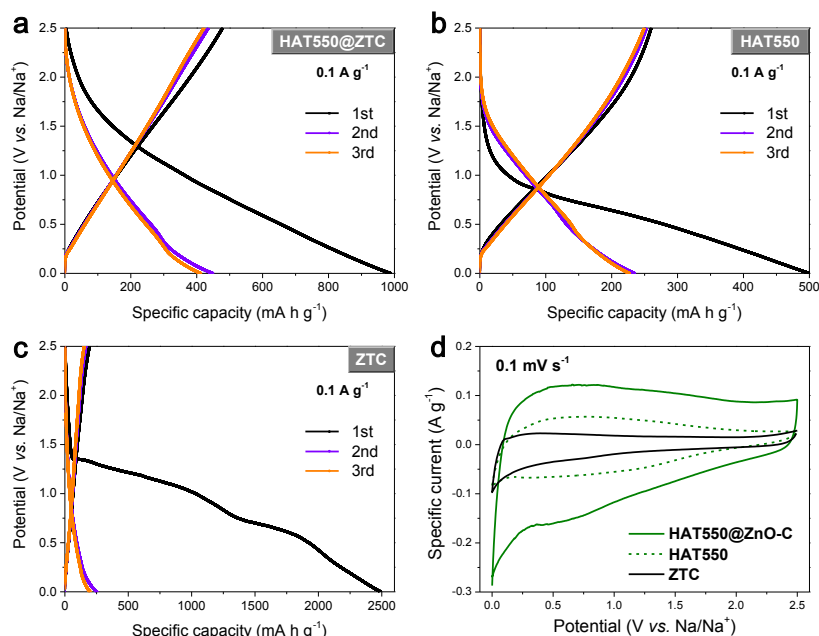
Figure 4.13. Half-cell tests of HAT550@ZTC and the reference samples. Galvanostatic charge-discharge profiles of the first cycles of (a) HAT550@ZTC, (b) HAT550, and (c) ZTC. (d) Cyclic voltammetry curves scanned at the rate of 0.1 mV s^{-1}.

The rate capability is examined by varying the specific current in the range of 0.1 to 20 A g^{-1} (**Figure 4.14**a-d). All the samples show a decay of capacity with the increase of current, but with apparently different decay degrees (**Figure 4.14**a-c). At 20 A g^{-1}, the specific capacity of HAT550@ZTC, HAT500, and ZTC is 124, 27, and 2 mAh g^{-1}, respectively, corresponding to retention of 36%, 12%, and 1.6% (**Figure 4.14**d). The inferior rate capability of ZTC can be ascribed to nonpolar N-free carbon surface which is likely to repulse the polar Na^{+}. Furthermore, the adsorption of Na^{+} by ZTC defects and micropores tends to be unfavorable in kinetics compared with the reversible binding process of sodium species with nitrogen-based functional groups. On the other hand, although with the same sodium storage mechanism, HAT550@ZTC prevails over HAT500 in terms of rate capability. This is attributed to two reasons. The first one is the superior electrical conductivity of the HAT550@ZTC sample, which is induced by the ZTC conductive matrix as well as its

strong binding and large contact area with the embedded semi-conductive HAT550 nanoparticles. Moreover, the nanoparticle morphology and the electrolyte reservoir (spare space in the mesopores due to the shrinkage of condensation of HAT-CN) can greatly shorten the transport length of the sodium ions, leading to the appreciable dynamics for ion transport and contributing to the superb rate capability. These factors are further elucidated by the Nyquist plots (**Figure 4.14**e), where all the samples exhibit a semicircle curve in the high frequency region plus a straight line in the low frequency region, a typical impedance curve for battery materials. Basically, the diameter of the semicircle represents the interfacial charge transfer resistance, which mainly come from the electric and ionic resistances at the interface between the electrode and the electrolyte. The smallest semicircle for HAT550@ZTC reveals its lowest resistance for both electrons and ions, accounting for its admirable rate capability.
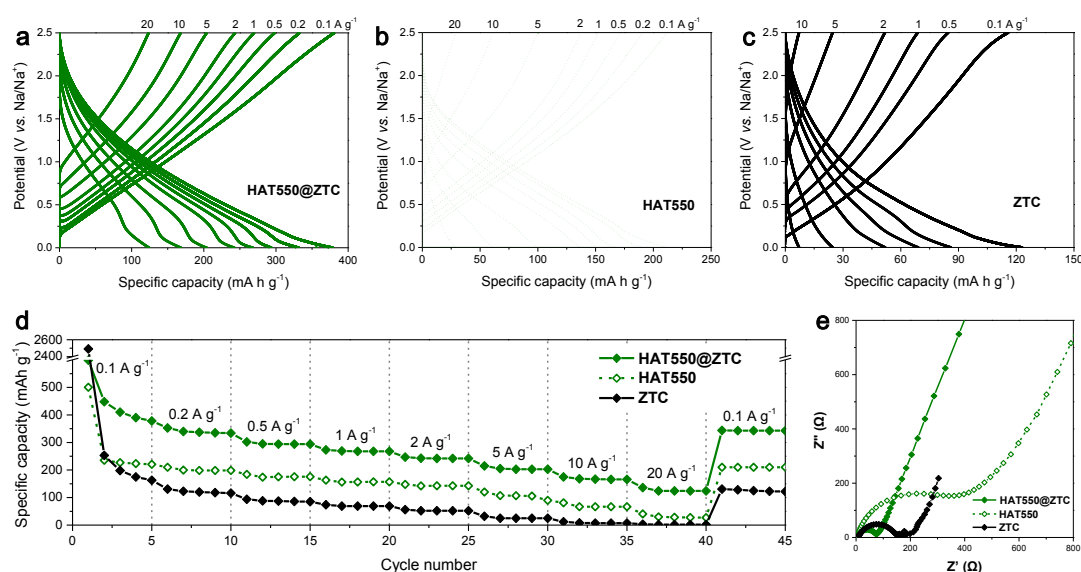
Figure 4.14. Half-cell tests of HAT550@ZTC and the reference samples. Galvanostatic charge-discharge profiles at different specific currents of (a) HAT550@ZTC, (b) HAT550, and (c) ZTC. (d) Rate performance of the prepared samples at different specific currents, and (e) Nyquist plot of HAT550@ZTC and HAT550.

HAT550@ZTC provides a reversible specific capacity of 343, 268, 203, 166, and 124 mAh g^{-1} at 0.1, 1, 5, 10, and 20 A g^{-1}, respectively. Such a superior capacity and rate

capability is attributed to the high nitrogen content, nanoparticle morphology, admirable conductivity, and mesoporous ion reservoir. The high nitrogen content with small nanoparticle morphology provides abundant accessible active sites for sodium ion deposition, giving rise to the appreciable capacity. In terms of rate capability, the conductive ZTC matrix acts as the high way for electron transport, while the nanoparticle morphology and mesoporous ion reservoir shortens the transport length of sodium ions. These two factors promote the dynamics of electron and ion transport, and thus result in its excellent rate capability. The high cycling stability of is verified by the cycling test, which maintains about 90% of the initial capacity after 1300 deep charging-discharging cycles at 0.5 A g^{-1}, indicating sufficient electrochemical stability of the nitrogen-containing groups throughout cycling (**Figure 4.15**).
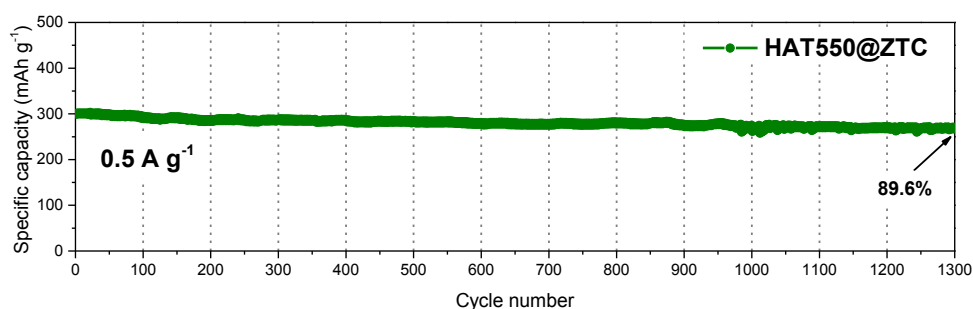
Figure 4.15. Cycling test of HAT550@ZTC at 0.5 A g^{-1} for 1300 cycles.

To verify the practical applicability, a prototype NIC full cell is fabricated with the HAT550@ZTC and STC-16 as the anode and cathode, respectively. STC-16 with hierarchical micro- mesopore architecture exhibits good performance as the cathode material in the half-cell NICs with metallic sodium as the counter electrode (**Figure 4.16**). Both cathode and anode are activated before assembling into the full cell, with the same procedure illustrated in section 4.1. The HAT550@ZTC||STC16 full cell is measured with the working voltage cut offs between 1.0 V and 4.0 V to maximize the utilization of the working potential range of both electrodes and minimizing the risk of electrolyte decomposition or other side reactions. The nearly

rectangular shape of CV curves up to 500 mV s^{-1} (**Figure 4.17**a), the almost symmetric triangle shape of the GCPL curves up to 10 A g^{-1} (**Figure 4.17**b), as well as the practically vertical curves in the low-frequency region of the Nyquist plots (**Figure 4.18a**) indicate the mainly capacitive behavior of the NIC. However, slight distortions from the perfect capacitive shape of these curves indicate the small deviation from the ideal capacitive behavior, which is likely caused by the non-capacitive storage of sodium in the HAT550@ZTC anode. Calculated by the GCPL curves, the specific capacitance of the NIC full cell reaches 48.5 F g^{-1} at a specific current of 0.05 A g^{-1} (according to the total mass of the cathode and anode), while it maintains high values of 40, 30, 25, and 15 F g^{-1} at 1, 5, 10, and 20 A g^{-1}, respectively (**Figure 4.17**c). This is also confirmed by the small voltage drop of 0.32 V even at the high specific current of 10 A g^{-1} (**Figure 4.17**b). The superior rate capability is attributed to efficient charge carrier transfer, which is revealed by the Nyquist plot (**Figure 4.18**a). The small intercept along the real axis (3.9 Ω) and the minor semicircle illustrate the low intrinsic resistance and high electrical conductivity in both cathode and anode. In the medium-frequency region, the very short Warburg length implies appreciable ion transport dynamics, which is ascribed to the nanoparticle morphology and mesoporous ion reservoir of the anode, as well as the rapid capacitor-type cathode. Accordingly, the Ragone plot (**Figure 4.17**d) of the NIC shows that the asymmetric cell with the voltage window of 1.0-4.0 V provides the maximum specific energy of 61 Wh kg^{-1} at a specific power of 0.1 kW kg^{-1}, with a slight drop to 44 Wh kg^{-1} at 3.4 kW kg^{-1}, and still maintains 12 Wh kg^{-1} at a specific power of 24 kW kg^{-1}. The cycling stability was measured by the cycling test at a specific current of 1 A g^{-1}. After 1000 cycles, a specific capacitance of 36.6 F g^{-1} is maintained corresponding to capacitance retention of 91.5% (**Figure 4.18**b). The minor 8% capacity loss might be related to the large voltage window that causes the degradation in the STC-16 oxygen functionalities at the lower potential range.[169] The Coulombic efficiency is nearly 100% throughout

the cycling process, showing the excellent reversibility of the NIC. Thus, the NIC demonstrates a much higher energy density compared to commercial EDLCs, as well as comparable power density and cycling life, showing great potential as an alternative candidate for future high power electrochemical energy storage.
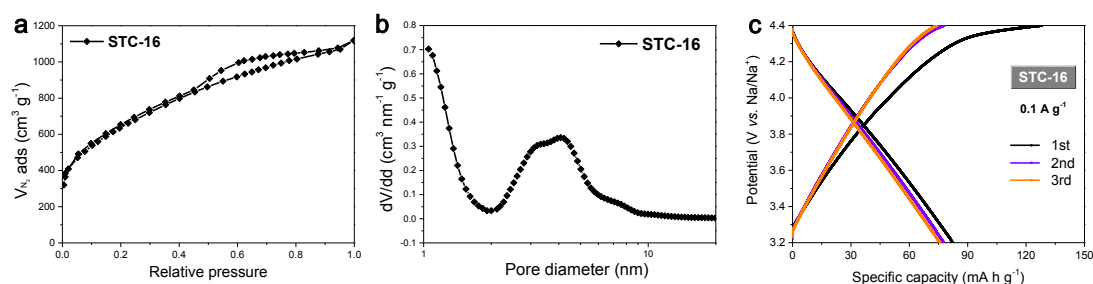
Figure 4.16. (a) N_2 physisorption isotherms (at -196 ℃) with corresponding (b) differential pore size distribution of STC-16. (c) Galvanostatic charge-discharge profiles of the initial three cycles of STC-16 at 0.1 A g^{-1} as the cathode in a half cell.
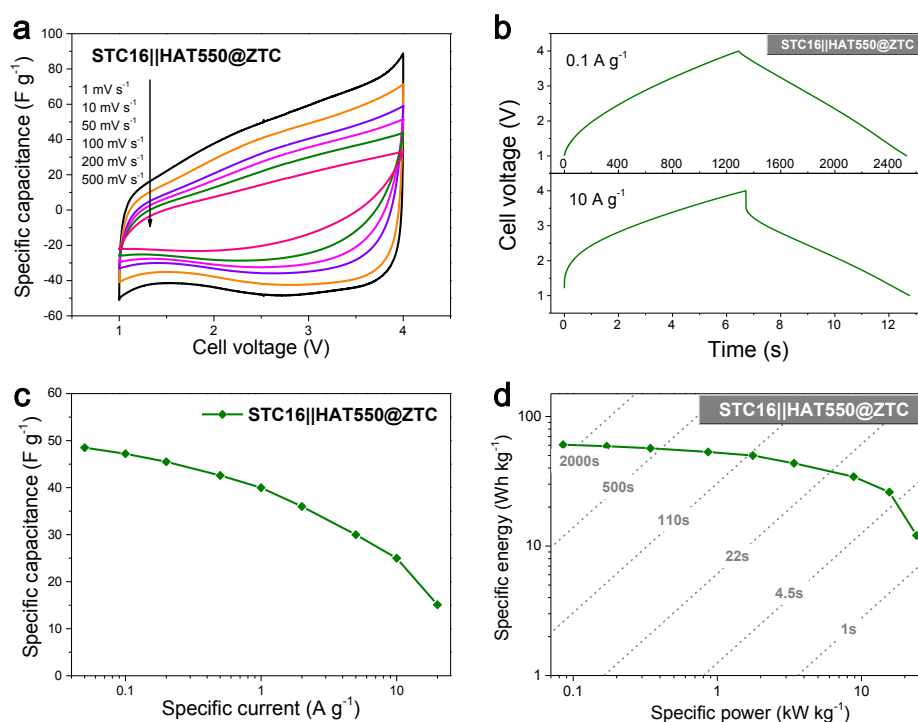
Figure 4.17. Full-cell test of the NIC with HAT550@ZTC as anodes and STC-16 as cathodes. (a) Cyclic voltammetry curves (1.0-4.0 V), (b) Galvanostatic charge-discharge profiles at 0.1 A g^{-1} and 10 A g^{-1}, (c) capacitance retention with specific current increase, and (d) Ragone plots of the NIC full cell.
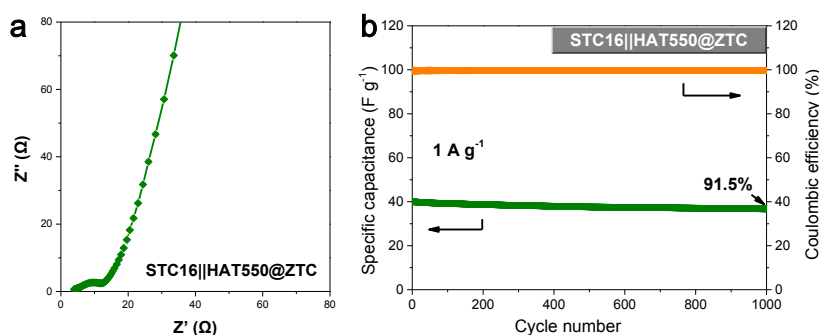
Figure 4.18. (a) Nyquist plot, and (b) cycling test of the NIC full cell.

In summary, a composite material composed of nitrogen-rich carbon nanoparticles embedded in conductive mesoporous carbon matrix (HAT550@ZTC, nitrogen content up to 26 wt%) is fabricated by impregnating ZTC with HAT-CN followed by thermal condensation. The composite presents remarkable rate capability as the anode for NICs, with a reversible capacity of 343 mAh g^{-1} at 0.1 A g^{-1} and capacity retention of 124 mAh g^{-1} at 20 A g^{-1}. These properties are ascribed to the abundant nitrogen-functional sites for sodium deposition introduced by condensation of HAT-CN, as well as high electrical conductivity and efficient ion transport induced by the conductive matrix and elaborate nanostructure, respectively. A full cell device of NIC employing HAT550@ZTC as the anode and STC-16 as the cathode provided remarkable energy and power density in the voltage range of 1.0-4.0 V (61 Wh kg^{-1} at 0.1 kW kg^{-1}, and still maintains 12 Wh kg^{-1} at 24 kW kg^{-1}) as well as long cycle life (~92% capacity retention after 1000 cycles). The specific energy is indeed significantly higher than that of state-of-the-art EDLCs without losing the excellent power capability and cycling stability. More importantly, disclosed is the synergistic effects of the high nitrogen content, nanostructure design, and the electrical conductivity for high capacity and rate capability, which sheds substantial light on a future targeted promotion of NICs and sodium-based batteries employing nitrogen-rich carbons as the anode materials.

5. Conclusions and Perspectives

The central motivation of the thesis was to provide possible solutions and concepts (mechanisms) for minimizing the dilemma of the inferior energy density of supercapacitors. (Nitrogen-doped) porous carbon materials for sure play a major role as electrodes in this context. IL electrolytes with larger electrochemical windows and novel device design of NIC can influence the energy density even more pronouncedly. Therefore, the advanced design of electrode materials and the insights into the fundamentals of the energy storage mechanisms are the two most crucial points to be addressed. In this regard, four main topics were investigated, which can be all related to the novel synthesis of advanced design of electrodes for EDLCs and NICs, as well as the study of their energy storage mechanisms (**Figure 5.1**).
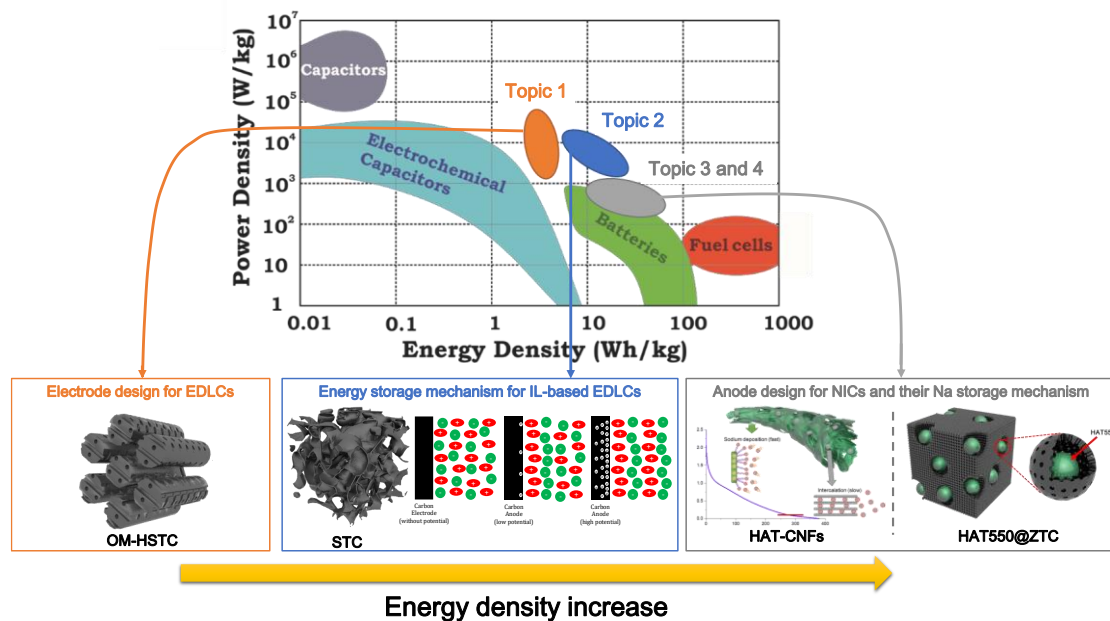
Figure 5.1. Top: Ragone plot of the supercapacitors developed in this dissertation in comparison with other representative electrochemical energy storage devices. Bottom: schematic summary of each topic.

The first topic described in section 3.1 mainly focused on the synthetic method of advanced electrode materials with hierarchical pore architecture for traditional EDLCs. Here, ordered mesoporous carbon with high content of micropores (OM-

HSTCs) were synthesized by a combined hard/salt-templating method. Large specific surface area up to 2649 m^2 g^{-1} and high pore volume exceeding 2.2 cm^3 g^{-1} have been obtained when applying optimized synthetic conditions. The synergistic effects of the large amount of micropores, highly ordered mesopores, and a thin microporous shell endow abundant active sites for charge storage, efficient electrolyte transport, and improved electrical conductivity. Therefore, EDLC employing OM-HSTCs as electrodes delivers high specific energy of 29 Wh kg^{-1} at a specific power of 78 W kg^{-1}, and still maintains 23 Wh kg^{-1} at a high specific power of 27 kW kg^{-1} in organic electrolyte. The novel OM-HSTC materials can also act as model substances for fundamental investigations on EDLC operating mechanisms (e.g., with NMR spectroscopy[170-173] or SAXS/SANS[174-175]) because the synthesis procedure allows adjustment of the pore sizes/geometries and ratios between the pore systems over a wide range and independent from each other. This feature remains difficult to be achieved with established methods towards OMMCs and other nanoporous carbons. Finally, the possibility of depositing a microporous shell around a hierarchical carbon particle will open new possibilities for applications where the encapsulation of guest species into a porous matrix is required.[176-177] Such a system could be for instance a carbon-sulfur composite for Li-S battery cathodes.

The employment of IL as electrolytes can cause the upsurge of the energy density of EDLCs by enlarging the electrochemical window. In the second topic (section 3.2), the mechanism of energy storage in IL-based supercapacitors was investigated. A series of hierarchical porous carbons (STCs) with different amounts of well-defined micropores and mesopores, large specific surface areas up to 2324 m^2 g^{-1} and high pore volumes exceeding 1.65 cm^3 g^{-1} were synthesized. EDLC with STC electrodes delivers the maximum specific energy of 76 Wh kg^{-1} at a specific power of 0.2 kW kg^{-1}, and still maintains 39 Wh kg^{-1} at a specific power of 9 kW kg^{-1}, using the ionic liquid model electrolyte of EMImBF$_4$ with the voltage window of 0-3.5 V. The pore

structure, electronic properties, and surface chemistry of the electrode materials were adjusted elaborately to thoroughly investigate the influence of these parameters on EDLC performance. The precise insights into structure-performance relationships enabled by this series of samples reveal that there is a significant contribution to energy storage due to ordering transitions in the bulk of the electrolytes in addition to charge storage in the electrical double layer. Decoupling their respective contributions in carbon materials with different pore sizes and surface chemistries holds much promise for further targeted improvement of IL-based energy storage devices. Based on these findings, the introduction of specific adsorption sites to strengthen the electrode-electrolyte interaction and thus to stabilize high energy electrolyte modifications is a more promising way to further increase the energy density of EDLCs than striving for ever-higher micropore volumes and SSAs. Finally, the uncovered mechanism offers new possibilities in modifying and optimizing the energy storage mechanisms in IL-based supercapcitors by controlled adjustments of the electrolyte composition (i.e., presence of traces of inorganic salts, traces of solvents, or variations of the ionic liquid ions themselves).

As a promising high-energy alternative supercapacitor to EDLCs, NIC was in focus of chapter 4, where the nitrogen-rich carbonaceous anode material and its sodium storage mechanism were thoroughly investigated. In section 4.1 (topic 3) , free-standing fibrous nitrogen-rich carbon materials (HAT-CNFs) were manufactured by electrospinning with a high nitrogen content of up to 15 wt%, a well-defined one-dimensional morphology, and microporous nanostructure. The free-standing carbon fibers present remarkable performance as anodes for NICs, with a reversible capacity of 395 mAh g^{-1} at 0.1 A g^{-1} and high rate capacity retention of 106 mAh g^{-1} at 10 A g^{-1}. These properties are ascribed to the high electrical conductivity and efficient ion transport introduced by the interconnected one dimensional structure of the fibers, and the high nitrogen content introduced by condensation of HAT-CN.

Furthermore, the mechanism of sodium storage in this material is illuminated by adjusting the ratio of nitrogen-doped carbon and graphitic carbon domains through different condensation temperatures. The intercalation process takes place only in the low underpotential range, while the sodium storage in the high underpotential range is attributed to its deposition on the nitrogen functional groups, which dominantly contribute to the high capacity. Sodium deposition is deduced to have significantly faster dynamics than the intercalation process. The textural properties (fiber diameter, internal porosity, fiber connectivity, and so on) still provide room for further improvement. And the role of the specific chemical architecture of the nitrogen-sites requires further investigation in order to better understand their contribution to the charge storage. The assembled full cell NIC device delivered the maximum specific energy and specific power of 95 Wh kg^{-1} and 13 kW kg^{-1}, respectively (voltage range of 0.5-4.0 V), showing a remarkable improvement to the other EDLCs of the current generation.

On the basis of the deduced sodium storage mechanism, section 4.2 (topic 4) was to further optimize the anode for NICs by improving the nitrogen content as well as enhancing the dynamics for fast electron and ion transport. A composite material composed of nitrogen-rich carbon nanoparticles embedded in conductive carbon matrix (HAT550@ZTC) was fabricated. The composite material provided the nitrogen-rich HAT550 nanoparticle component for sodium storage sites, which in close proximity with the conductive carbon backbone for fast electron transport. The elaborate nanostructure significantly facilitated fast ion transport. The HAT550@ZTC-based electrode therefore delivered a remarkable rate capability of 124 mAh g^{-1} at 20 A g^{-1}, which is expected to solve the most severe problem in NIC – the kinetic imbalance between cathode and anode. A full cell device of NIC employing HAT550@ZTC as the anode and STC-16 as the cathode provided a high specific energy up to 61 Wh kg^{-1} (despite the rather small voltage range of 1.0-4.0 V) with a remarkable specific power up to 24 kW kg^{-1}, indicating a prominent

promotion in specific power compared with the HAT-CNF anode materials. The approach for fabrication of such high nitrogen containing electrodes with desirable electrical conductivity shows great potential to scale up and provides a method to increase the rate performance of anode materials for NICs or sodium-ion batteries. Throughout this thesis, the ubiquitous problem of low energy density of supercapacitors is stressed by synthesizing high-performance electrode materials and exploring novel energy storage mechanisms in EDLCs and NICs. The elaborate designs and synthetic methods of electrodes (especially STCs) provide direct application value of practical usage with promising potential for commercial production. The energy density of the supercapacitors employing these electrode materials in this thesis significantly prevail that of common ones while maintaining the high power density and long cycle life. Even more importantly, revealed are the structure-performance relationships, as well as the mechanisms for energy storage in IL-based EDLCs and sodium storage in nitrogen-rich carbon-based NIC anodes. These fundamental understandings pave way for a future optimal design and targeted promotion of electrode/electrolyte materials, and are expected to help inspire concepts of novel electrochemical energy storage devices. One example are phase-change electrolytes for high-energy supercapacitors. Other possible concepts include decoupling the electron and ion storage separately in a composite two-phase solid material while improving their storage capacity and dynamics to achieve battery-level energy density, EDLC-level power density and cycle life.

6.   Appendix

6.1.   Abbreviations

Abbreviation	Full name
AC	Activated carbon
BET	Brunauer–Emmett–Teller theory
CMK	Carbon mesostructured by KAIST
CV	Cyclic voltammetry
EDLC	Electrochemical double-layer capacitor
IL	Ionic liquid
NIC	Sodium-ion capacitor
HIC	Hybrid-ion capacitor
LIC	Lithium-ion capacitor
OM-HSTC	Ordered mesoporous hard-salt-templated carbon
STC	Salt-templated carbon
QSDFT	Quenched solid density functional theory
NPs	Nanoparticles
PSD	Pore size distribution
SSA	Specific surface area
TPV	Total pore volume
XRD	X-ray diffraction
TEM	Transmission electron microscopy
SEM	Scanning electron microscopy
EDX	Energy-dispersive X-ray spectroscopy
TGA	Thermogravimetric analysis
XPS	X-ray photoelectron spectroscopy
HAT-CN	Hexaazatriphenylene-hexacarbonitrile
CNF	Carbon fiber

ZTC	ZnO-templated carbon
SAXS	Small-angle X-ray scattering
FWHM	Full-width at half maximum
PVP	Polyvinylpyrrolidone
DMF	Dimethylformamide
PTFE	Polytetrafluoroethylene
AcOH	Acetic acid
TEABF$_4$	Tetraethylammonium tetrafluoroborate
ACN	Acetonitrile
EMImBF$_4$	1-Ethyl-3-methylimidazolium tetrafluoroborate

6.2. Applied Methods

6.2.1. Nitrogen physisorption

Physisorption takes place whenever a fluid phase (the adsorptive) contacts with a solid surface (the adsorbent). The molecules adsorbed on the surface are denoted as the adsorbate. The interactions between the adsorbate and the adsorbent are basically van-der Waals forces without covalent chemical bond formation. A physisorption isotherm is the plot of the adsorbed amount of the fluid as a function of the relative pressure p/p_0, where p_0 is the saturation pressure of the adsorptive at a specific temperature. The isotherm is a measure of the pore size, pore geometry, and surface polarity. Thus, from the isotherms, one can obtain information of the porosity, in particular the specific surface area, the total pore volume, and the pore size distribution. The most often used adsorbate is nitrogen at -196 ℃, which is highly attractive because it is non-destructive, convenient to use, and allows precise analysis over a wide range of pore sizes including the complete range of micro- and mesopores.

In a typical volumetric nitrogen physisorption measurement, nitrogen is dosed in small portions into the measurement cell containing the sample and the adsorbed volume is detected in respect to the relative pressure at -196 ℃. The pressure is first increased usually till $p/p_0 \sim 1.0$. The thereby recorded points of adsorbed amount of fluid at a given relative pressure represent the adsorption branch of the isotherm. Usually, the pressure is also lowered again to measure the desorption behavior of the sample. The shape of the adsorption/desorption isotherm generally represents the interactions of the adsorbate with the adsorbent and is thus influenced by the pore size and pore shape.[178]

In 2015, the IUPAC reported an updated classification of the types of physisorption isotherms (**Figure 6.1**).[156] The type I(a) and I(b) isotherms are found for microporous materials; the difference between the two being the size of the micropores, i.e., type I(a) isotherms are observed by filling of ultramicropores (pores of width below 0.7 nm), whereas type I(b) isotherms are obtained by filling supermicropores (pores of width 0.7–2 nm) and even some small mesopores. Type II isotherms are typically obtained on non-porous or macroporous materials, where mono- and then multi-layer formation occurs on the surface. A sharp knee (point B) can be connected to the completion of the coverage of the surface with a monolayer of adsorbate. This multilayer formation is also observed in the rare type VI isotherm where each step indicates formation of a new layer of adsorbate on a smooth, non-porous surface. A type III isotherm indicates the presence of a nonporous or macroporous sample coupled with very weak adsorbate-adsorbent interactions. Hence, the adsorbate molecules are clustered around the most favorable adsorption site and no point B exits. A type IV isotherm is representative for mesoporous materials. Here, the shape is determined by the adsorbate-adsorbent interactions and by the interactions between the adsorptive molecules in the condensed state. The initial adsorption proceeds similar to a type II isotherm but at higher pressures pore condensation (inside the mesopores) occurs. Pore

condensation implies that a gas condenses inside a pore at pressures lower than the bulk liquid's saturation pressure (p_o). If the pores exceed a critical size (d > ~ 4 nm), capillary condensation is coupled with the formation of a hysteresis, giving rise to a type IV(a) isotherm. If the present mesopores are smaller, a reversible type IV(b) isotherm is observed. At high pressures, the adsorbed volume for a type IV isotherm usually reaches a saturation plateau. Type V and type VI isotherms are rather uncommon, and characteristic for a porous sample with weak adsorbent-adsorbate interactions and for a layer-by-layer adsorption on a non-porous specimen, respectively.
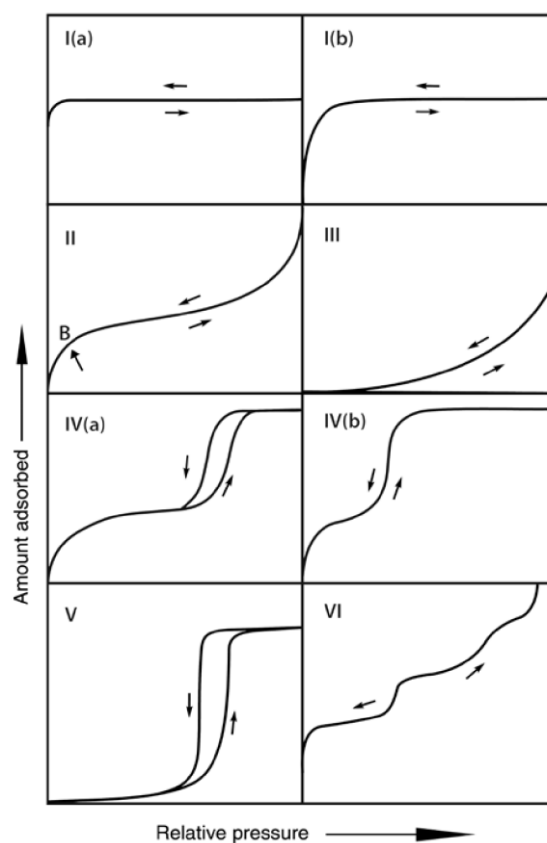
Figure 6.1. Classification of physisorption isotherms according to IUPAC.[156]

The points recorded during a N_2-phyisisorption measurement allow the calculation of the SSA by the employment of different models. The most commonly employed method nowadays is the so called Brunauer-Emmett-Teller theory.[179] In contrast to the older Langmuir-theory, the BET model takes the possibility of multilayer

adsorption of a fluid on the pore surface with a different adsorption enthalpy between the first and the following layers into consideration. In the BET equation (Equation (6.1)), V_{ads} is the total adsorbed volume, V_{Mono} is the volume of a monolayer, and C is the adsorption constant, $\frac{p}{(p_0-p)V_{ads}}$ is plotted against the ralative pressure and the volume of the monolayer can be calculated by extrapolation of the line to its intersection with the y-axis $\frac{1}{C \cdot V_{Mono}}$ or from the slope $\frac{C-1}{C \cdot V_{Mono}}$.

$$\frac{p}{(p_0-p)V_{ads}} = \frac{1}{C \cdot V_{Mono}} + \frac{1}{C \cdot V_{Mono}}\frac{p}{p_0} \tag{6.1}$$

After the V_{Mono} is obtained, the SSA can be calcultated according to equation (6.2). N_A is the Avogadro constant ($6.022 \cdot 10^{23}$ mol^{-1}), σ_{N_2} is the required surface area of a single N2 molecule in dense package (0.162 nm^2), V_{Mol} is the ideal gas volume ($2.241 \cdot 10^{-2}$ m^3 mol^{-1}), and m_{Ads} is the mass of the adsorbent.

$$SSA = \frac{N_A \cdot V_{Mono} \cdot \sigma_{N_2}}{V_{Mol} \cdot m_{Ads}} \tag{6.2}$$

In the presence of micropores (i.e., type I isotherms and combinations of types I and II or types I and IV isotherms, which are characteristic of many micro–mesoporous materials), the application of the BET method only leads to an apparent surface area (i.e., BET SSA). Because for predominantly microporous materials, linear BET plots are typically found at relative pressures of 0.1 and even lower. This makes it impossible to separate the processes of monolayer–multilayer adsorption and micropore filling, which may lead to a significant overestimation of the monolayer capacity in a BET analysis.

Alternatively, one may rather apply methods based on statistical mechanics, such as DFT-based methods, which correctly take into account the adsorption mechanism over the complete micro- and mesopore range. Microscopic methods based on DFT can provide a more realistic description of the thermo-physical properties of the adsorbed fluid. These approaches, which yield the

thermodynamic and density profiles of confined fluids in pores, accurately describe the adsorbed phase on a molecular level and thus provide detailed information about the local fluid structure near the adsorbent surface. The fluid-solid interaction potential is dependent on the pore shape model including slit, cylinder and spherical geometries and hybrid models have been developed for various material classes with different electronic structures such as carbons, silicas, zeolites, etc. Advanced methods based on DFT capture the essential features of the pore filling mechanism of micropores and the mechanism of pore condensation, evaporation, and hysteresis. As a consequence they allow one to obtain reliable information regarding SSA and pore size distributions over the complete range of micro- and mesopores. The most advanced method for the characterization of nanoporous carbons is the quenched solid density functional theory which takes into account the surface roughness and defects on energetically heterogeneous surfaces which are typically present in porous carbon materials.[178]

6.2.2. Scanning Electron Microscopy / Transmission Electron Microscopy

SEM and TEM, are both based on interactions of electrons with the samples. Generally, electrons are generated by an electron gun, accelerated by an electromagnetic field, and vertically directed (as well as focused) towards the sample by electromagnetic lenses.

SEM is based on the detection of secondary and backscattered electrons created in the samples upon interaction with the incident electron beam. Thus, information about the morphology and the chemical properties of the specimen can be gathered. Due to collisions between the incident electron beam and valence electrons of the sample, secondary electrons are created. Those electrons possess relatively low energy and can only escape the specimen if they are generated close to the surface. Local curvatures (e.g., edges or plates) facilitate the release of electrons. Hence, the quantity of created electrons depends on the morphology of the sample which leads to an intensity contrast in the recorded image representing

topological information of the specimen's surface. Qualitative information about the sample can be obtained by EDX. Here, the incident electron beam excites an electron from an inner shell of an atom. The electron is ejected thus generating an electron hole in the inner shell. Subsequently, an electron from an outer shell occupies the generated electron hole. The difference in energy between the inner- and outer shell is released in the form of X-rays. The X-ray energy is specific for each element leading to qualitative information. The X-ray intensities of the different elements present in a sample allow conclusions regarding the quantitative occurrence of the elements. Moreover, EDX-mapping can be used to study the local distribution of elements in the sample. It is worth noting that EDX is sensititve for the surface rather than for the bulk.

In TEM the electrons transmitting a very thin sample are detected leading to even higher resolution in comparison to SEM. The resolution can be adjusted by the acceleration voltage where larger voltage generally allows higher resolutions. The contrast of the detected image depends on the thickness and the elemental composition of the specimen. In the typically applied bright field mode, the non-scattered (or only slightly scattered) electrons are detected. Thus, thicker regions appear darker than thinner domains, and low scattering (lighter) elements appear brighter than heavier elements.

6.2.3. X-Ray Diffraction

XRD is a widely employed method to characterize crystalline substances. XRD is based on the interaction between an X-ray beam and the electrons of the atoms in the specimen. The X-ray beam is generated by high-energy electrons which hit a material and are thereby deaccelerated. The therein occurring processes result in the radiation of a continuous X-ray spectrum and in a for each element specific line-spectrum of X-rays. The individual X-rays of the line-spectrum are monochromatic and are used for the XRD experiment. If the monochromatic X-ray hits the specimen, elastic and inelastic interactions occur. Inelastic effects cause coherent scattering

representing the basis for all diffraction experiments. Generally, diffraction occurs if the wavelength of the radiation is in the same range as the distance of the diffraction lattice. Since the atom distances in crystals are in the same range as the wavelength of X-rays, crystalline materials have a number of diffrction lattices which can cause constructive interference during a XRD experiment. It is to consider that constructive interference only occurs if the optical path difference (Δ) is an integral multiple of the wavelength (λ). Hence, positive interference exits only for specific diffraction angles (θ). The mathematical description between the interlayer spacing (d) of the atomic planes and λ (in respect to θ) is given by Bragg's Law (Equation (6.3)).

$$\Delta = n\lambda = 2d\sin(\theta) \tag{6.3}$$

Positive interferences lead to reflections in the recorded diffractogram revealing the characteristic diffraction pattern of the investigated specimen.

6.2.4. Thermogravimetric Analysis

TGA allows to monitor different thermodynamic events such as phase transition, thermal decomposition as well as the adsorption and desorption of gases. Usually, the mass change of a sample during heating is observed. A sample on a balance is heated with a certain heating rate and the mass of the sample is recorded as a function of temperature and time.

6.3. Experimental Section

Chemicals

Table 6.1. List of used chemicals.

Chemical	chemical formula	Purity	supplier
Cyanamide	$NCNH_2$	99%	Sigma Aldrich
Ethanol	CH_3CH_2OH	$\geq$ 99.8 %	Sigma Aldrich
Carbon black (super-P)	C	99+%	Alfa Aesar
Sodium sulfate	Na_2SO_4	$\geq$99%	Sigma Aldrich
Acetonitrile	CH_3CN	99.8%	Sigma Aldrich
Sodium chloride	NaCl	$\geq$ 99.8%	Sigma Aldrich
Sulfuric acid	H_2SO_4	98%	Merck
Zinc chloride	$ZnCl_2$	98+%	Alfa Aesar
Poly(acrylic acid)	$(C_3H_4O_2)_n$	$\geq$ 99%	Sigma Aldrich
Sodium perchlorate	$NaClO_4$	$\geq$ 99%	Sigma Aldrich
Sodium hydroxide	NaOH	$\geqslant$98%	Sigma Aldrich
Acetic acid	CH_3COOH	$\geq$99%	Sigma Aldrich
Ethylene carbonate	$C_3H_4O_3$	99%	Sigma Aldrich
Propylene carbonate	$C_4H_6O_3$	99.7%	Sigma Aldrich
Fluoroethylene carbonate	$C_3H_3FO_3$	99%	Sigma Aldrich
Sucrose	$C_{12}H_{22}O_{11}$	> 99.5%	Sigma Aldrich
Diaminomaleonitrile	$C_4H_4N_4$	98%	Sigma Aldrich
Polyvinylpyrrolidone	$(C_6H_9NO)_n$	$\geq$99%	Sigma Aldrich
Dimethylformamide	C_3H_7NO	99.8%	Sigma Aldrich
Hydrochloric acid	HCl	37%	Sigma Aldrich
Polytetrafluoroethylene dispersion	$(C_2F_4)_n$	60 wt%	Sigma Aldrich
Hexaketocyclohexane octahydrate	$C_6O_6 \cdot 8H_2O$	97%	Sigma Aldrich
Tetraethylammonium tetrafluoroborate	$(C_2H_5)_4N(BF_4)$	$\geq$99%	Sigma Aldrich
1-ethyl-3-methylimidazolium tetrafluoroborate	$C_6H_{11}BF_4N_2$	$\geq$99%	Sigma Aldrich
Triblock copolymer Pluronic P123	$HO(CH_2CH_2O)_{20}(CH_2CH(CH_3)O)_{70}(CH_2CH_2O)_{20}H$	$\geq$ 99%	Sigma Aldrich
Tetraethyl orthosilicate	$Si(OC_2H_5)_4$	$\geq$ 99%	Sigma Aldrich
Zinc oxide nanoparticles	ZnO	99%	Nanostructured & Amorphous Materials, Inc.

Synthesis of ordered mesoporous SiO$_2$ (SBA-15)

The hexagonal ordered silica SBA-15 was synthesized by dissolving 66.8 g of triblock copolymer Pluronic P123 (EO$_{20}$PO$_{70}$EO$_{20}$; M$_w \approx$ 5800) in 1212 g of distilled water and 38.6 g of 37% hydrochloric acid aqueous solution at 35 °C for 12 h. After stirring for 1 h, 143.6 g of tetraethyl orthosilicate were subsequently added to the solution. After 24 h of stirring at 35 °C, the white dispersion underwent a hydrothermal treatment at 130 °C for another 24 h. The resulting white powder was filtered, washed with a water/ethanol mixture (2000 mL, 1:1 by volume), and finally calcinated under air atmosphere at 550 °C for 5 h.

Synthesis of OM-HSTCs and STC_2

For the synthesis of OM-HSTCs, SBA-15 and ZnCl$_2$ were employed as hard- and salt template, respectively. In a typical procedure, 1.0 g SBA-15 was first impregnated with 4 mL of an aqueous solution of 1.25 g sucrose, 2.5 g ZnCl$_2$, and 0.14 g concentrated sulfuric acid in a petri dish. The mixture was then heated to 100 °C and held for 6 h followed by subsequent heating to 160 °C for another 6 h under air to polymerize of the carbohydrate molecules. Afterwards, the mixture was impregnated again with 3 mL of an aqueous solution of 0.8 g sucrose, 0.8 g ZnCl$_2$, and 0.09 g concentrated sulfuric acid, followed by repeated heating to 100 °C for 6 h and 160 °C for 6 h. The polymerized carbohydrate was carbonized and the salt template was removed in a horizontal tubular furnace at 900 °C for 2 h under N$_2$ flow. The heating ramp was set to be 60 °C h^{-1} from room temperature to 300 °C and 150 °C h^{-1} from 300 °C to 900 °C. SBA -15 was removed by heating the carbon/silica composite in 5 M NaOH aqueous solution overnight under reflux followed by filtration, washing with large amounts of water, and drying at 60 °C. The final product was named as OM-HSTC_X_Y, where X and Y represent the mass ratio of ZnCl$_2$/sucrose and sucrose/SBA-15, respectively (for example, OM-HSTC_2_2.05 for the above sample). Other hard-salt templated carbons, including OM-HSTC_1_2.05, HSTC_3_2.05 and OM-HSTC_1_1.31, were synthesized by the same method but with

different amounts of $ZnCl_2$ and sucrose (**Table 6.2**). Hard-templated ordered mesoporous carbon (OM-HTC_0_2.05) and salt-templated microporous carbon (STC_2) were employed as reference samples. OM-HTC_0_2.05 was synthesized by the similar procedure as OM-HSTC_2_2.05 without the addition of salt templates. STC_2 was prepared by the salt-template method. Typically, 5 mL aqueous solution of 2 g sucrose, 4 g $ZnCl_2$ and 0.2 g concentrated sulfuric acid was dried at 100℃ for 6 h, before being heated to 160 ℃ and kept for 6 h. The mixture was then transferred to a horizontal tubular furnace for carbonization at 900 ℃ for 2 h under N_2 flow (150℃ h^{-1} heating rate).

Table 6.2. Summary of the amounts of sucrose, $ZnCl_2$, and SBA-15 used for the synthesis of different carbon materials.

	Sucrose (g)	$ZnCl_2$ (g)	SBA-15 (g)
OM-HSTC_2_2.05	2.05	4.1	1
OM-HSTC_1_2.05	2.05	2.05	1
OM-HSTC_1_1.31	1.31	1.31	1
HSTC_3_2.05	2.05	6.15	1
OM-HTC_0_2.05	2.05	-	1
STC_2	2	4	/

Synthesis of salt-templated carbons (STCs)

$ZnCl_2$ was employed as the salt template for the synthesis of STCs. In a typical process, 30 mL aqueous solution of 5 g sucrose, a certain amount of $ZnCl_2$ and 0.55 g concentrated sulfuric acid was dried at 100 ℃ for 6 h, before being heated to 160 ℃ and kept f or 6 h. The amount of $ZnCl_2$ is determined by the mass ratio of the salt template to sucrose regarding different STCs (e.g. 16 for STC-16). The mixture was then transferred to a horizontal tubular furnace for carbonization at 900 ℃ for 2 h under N_2 flow with heating rate of 1 ℃ min^{-1}. After cooling to room temperature,

it was thoroughly washed by stirring in 1 M HCl aqueous solution overnight, followed by drying at 60 ℃ for 6 h.

Synthesis of nitrogen-doped STCs (NDSTCs)

0.5 g STC was dispersed in 1 mL aqueous solution of cyanamide (1 g mL^{-1}), followed by drying at 60 ℃ for 12 h under air. After calcination of the mixture at 800 ℃ for 4 h under N_2 flow at with a heating rate of 1 ℃ min^{-1}, the corresponding NDSTC was obtained.

Synthesis of CO_2-activated STCs (Ac-STCs)

Ac-STCs were synthesized by CO_2 activation of the STCs. Typically, 0.5 g STC was put in a horizontal tubular furnace for thermal treatment at 800 ℃ for 0.5 h under CO_2 flow with a heating rate of 10 ℃ min^{-1} to yield around 0.3 g corresponding Ac-STC.

Synthesis of hexaazatriphenylene-hexacarbonitrile (HAT-CN)

HAT-CN was synthesized according to a previous procedure.[153-155] Hexaketocyclohexane octahydrate (4 g, 12.6 mmol) and diaminomaleonitrile (10.88 g, 100.8 mmol) were refluxed in acetic acid (AcOH, 150 mL) for 2 h. The black suspension was filtered off while hot and washed with hot AcOH (3 × 25 mL) resulting in a black solid. The solid was suspended in 30 % HNO_3 (60 mL) and heated at 100 ℃ f or 3 h. The hot dark brown suspension was poured into ice water (200 mL) and cooled overnight. The suspension was filtered and the solid was refluxed in acetonitrile (400 mL) for 2 h followed by filtration. The filtrate was evaporated under vacuum yielding an orange solid.

Synthesis of HAT-derived carbon fiber (HAT-CNF)

HAT-CNF-X was fabricated using electrospinning and subsequent condensation. The spinning solution was prepared by stirring HAT-CN (200 mg) and polyvinylpyrrolidone (PVP, 300 mg) in DMF at 60 ℃ for 2 h. The solution was loaded to a 2 mL syringe, and mounted on the syringe pump in a spinning machine (Professional Electrospinner, Yflow, Spain). A positive high voltage was connected

via alligator clip to a needle with an inner diameter of 0.5 mm and outer diameter of 1 mm. A grounded rotating drum covered with aluminum foil was employed to collect the fibers at a rotation speed of 200 rpm for a duration of 25 min. Process parameters were fixed at a high voltage of 13 kV, flow rate of 2 mL h⁻¹ and distance from tip to collector of 15 cm. The temperature was 23℃ and the humidity 40 -50%. The pristine fibers were then carbonized in a chamber furnace at different temperatures for 1 h under N_2 gas flow. The heating ramp was set up to be 2.5 ℃ min⁻¹ from room temperature to 450 ℃, and 4 ℃ min ⁻¹ from 450 ℃ to 700, 850 or 1000 ℃. The resulting materials are labelled as HAT -CNF-X, where X stands for the condensation temperature.

Synthesis of ZnO-templated carbon (ZTC)

ZnO was employed as the hard template for the synthesis of ZTC. 8.0 g ZnO nanoparticles were first impregnated with 13 mL of an aqueous solution of 7.0 g sucrose and 0.4 g NaOH in a petri dish. The mixture was then heated to 100 ℃ and held for 3 h followed by subsequent heating to 160 ℃ for another 6 h under air to polymerize of the carbohydrate molecules. Afterwards, the polymerized carbohydrate was carbonized in a horizontal tubular furnace at 950 ℃ for 2 h under N_2 flow. The heating ramp was set to be 60 ℃ h⁻¹ from room temperature to 950 ℃. Then it was thoroughly washed by stirring in 1 M HCl aqueous solution overnight, followed by drying at 60 ℃ for 6 h.

Synthesis of HAT550@ZTC

HAT550@ZTC was prepared through post-treatment of ZTC with HAT-CN, followed by calcination. In a typical procedure, 400 mg HAT-CN was dissolved in 0.6 mL dimethylformamide by sonication, which was then injected into 100 mg ZTC followed by thoroughly grinding. Afterwards, the mixture was dried under vacuum at 60 ℃. Finally, the HAT550@ZTC was obtained by calcination of the composite material in a horizontal tubular furnace at 550℃ for 1 h under N_2 flow. The heating ramp was set to be 240℃ h⁻¹.

Materials characterization

N_2 physisorption experiments were carried out at -196 ℃ on a Quadrasorb apparatus (40-60 mg sample) and an Autosorb IQ instrument (10-20 mg sample for low-pressure measurements), both from Quantachrome Instruments. Prior to all measurements, the samples were outgassed at 150 ℃ for 20 h under vacuum. SSAs were calculated using the multi-point Brunauer-Emmett-Teller (BET) model (p/p_o = 0.05-0.2). Total pore volumes were determined at p/p_o = 0.95. SSAs and V_t were calculated from the data obtained by measurements with 40-60 mg sample. Pore size distributions were calculated using the QSDFT method (adsorption branch kernel) for N_2 adsorbed on carbon with a slit/cylindrical pore shape at -196 ℃ from the data obtained by the low-pressure measurements. CO_2 physisorption experiments were carried out at 0 ℃ on the Autosorb instrument to investigate the pores with the diameter smaller than 1.5 nm. Corresponding PSDs were calculated by the non-local density functional theory method for CO_2 adsorbed on carbon at 0 ℃.

Further structural characterization was carried out by SEM (LEO 1550-Gemini) operating at 3 kV, transmission electron microscopy TEM (EM 912 Omega/Carl-Zeiss Oberkochen) operating at 120 kV, and high-resolution TEM (JEOL ARM 200F) operating at 200 kV. To prepare the TEM samples, carbon particles were dispersed in ethanol, followed by dropping several droplets on a carbon-coated copper TEM grid and drying at room temperature. SAXS was conducted with a Bruker AXS and $CuK_{\alpha 1}$ radiation (λ=0.154 nm). Raman spectra were recorded using a Renishaw inVia Raman Microscope operating with an objective (Nikon, 10x/0.25, ∞/- WD 6.1) and an excitation wavelength of 532 nm with a power of 4.0 mW. After the background noise was subtracted from the obtained Raman spectra, the D, D^2, A, and G bands were fitted with a Lorentz function. Thermogravimetric analysis was conducted with a Netzsch TG 209 F1 device under constant artificial air flow in platinum pans at a heating rate of 10℃ min^{-1} to 1000 ℃. XPS measurement was performed on a

spectrometer equipped with $Al_{K\alpha}$ anode (hυ = 1486.6 eV). Elemental compositions were determined using survey scans over a range of 1350-0 eV with a step size of 1.0 eV and a pass energy of 200 eV. Quantitative characterization of the presence of various nitrogen and oxygen sites were accomplished with high-resolution XPS, scanning over a range of 410-392 eV and 544-524 eV, respectively, with a step size of 0.1 eV and pass energy of 50 eV.

Fabrication of EDLCs and electrochemical measurements

To prepare free-standing electrodes for EDLCs, carbon materials and polytetrafluoroethylene (PTFE, 60 wt% solution in H_2O from Sigma Aldrich) were mixed with a mass ratio of ~9:1 in ethanol. The solution was then transferred to a glass plate and mixed with razor blades until it changed to a rubber-like consistency. Then it was placed into aluminum foil and rolled to uniformly thin sheets (thicknesses 180±10 µm) using a commercial roll mill, followed by punching into free-standing electrode disks of 10 mm in diameter. The areal density of an electrode was above 3 mg cm^{-2}. The electrodes were dried at 120℃ for 12 h under vacuum. EDLCs were tested with a symmetrical two-electrode configuration employing different electrolytes, namely 1 M Na_2SO_4 aqueous solution, 1 M tetraethylammonium tetrafluoroborate/acetonitrile solution, and 1-ethyl-3-methylimidazolium tetrafluoroborate (≥99.0%, Sigma Aldrich). Typically, custom-built cells (with a spring to control the pressure at 10 MPa and highly conductive titanium pistons)[180] and Swagelok cells were employed as supercapacitor devices with OM-HSTC electrodes and STC electrodes, respectively. They were assembled using a pair of circular electrodes sandwiching a separator, with 100 µL electrolyte and two platinum foils as current collectors. Commercially available Dreamweaver Silver (Dreamweaver International Inc.) separator of 13 mm in diameter was used for aqueous and EMImBF$_4$ electrolyte, while a 25 µm trilayer polypropylene-polyethylene-polypropylene membrane (Celgard 2325, 13 mm in diameter) was used as separator in TEABF$_4$/AN electrolyte. For the aqueous electrolyte, the device

assembly took place under air atmosphere. For the other two electrolytes, EDLCs were assembled in an argon filled glove box (H_2O < 0.1 ppm, O_2 < 0.1 ppm). A Biologic MPG-2 galvanostat/potentiostat was used for electrochemical characterization. All measurements were performed at room temperature. For the test in three-electrode configuration, another piece of PVDF-bound activated carbon was introduced from the side to a custom-made cell[27] and served as quasi-reference electrode (reference potential: 190 ± 10 mV versus ferrocene).[27] The counter electrode was made of PTFE-bound NDSTC-16 and largely oversized in charge capacity. All other test conditions are chosen similar to the two-electrode configuration. The electrochemical impedance spectroscopy was performed at open circuit potential with a sinusoidal signal over a frequency range from 20 kHz to 10^{-2} Hz at an amplitude of 10 mV. The specific gravimetric capacitance of a single electrode C_{EIS} (F g^{-1}), was calculated according to the following formula and normalized to the specific gravimetric capacitance at 10^{-2} Hz:

$$C_{EIS} = \frac{2|Im(Z)|}{2\pi f[(Im(Z))^2 + (Re(Z))^2] \cdot m} \tag{6.4}$$

where f is the operating frequency (Hz), $Im(Z)$, and $Re(Z)$ are the imaginary and real component of the total device impedance (Ω), and m is the active mass in a single carbon electrode (g).

CV tests were performed at scan rates of 2-500 mV s^{-1} for aqueous and organic electrolytes, and 2-200 mV s^{-1} for IL electrolytes. The carbon differential gravimetric capacitance for CV plots, C_d (F g^{-1}), and the integral gravimetric capacitance, C (F g^{-1}), were calculated according to the following equations:

$$C_d = \frac{2I}{m\gamma} \tag{6.5}$$

$$C = (\int_{V_1}^{V_2} I_+(V)dV - \int_{V_1}^{V_2} I_-(V)dV)/m \cdot \gamma \cdot (V_2 - V_1) \tag{6.6}$$

where I is the current (A), γ is the scan rate (V s^{-1}), and m is the active mass in a single carbon electrode (g).

GCPL measurement was applied at specific currents between 0.1 and 40 A g^{-1} in different cell voltage ranges (-0.5 V to +0.5 V, 0 to +2.5 V, and 0 to +3.5 V for aqueous, organic and ionic liquid electrolytes, respectively). The carbon gravimetric capacitance, C (F g^{-1}), was calculated according to equation (6.7):

$$C = \frac{2Q_{dis}}{(V-V_{drop})m} \tag{6.7}$$

Where Q_{dis} (C) is the charge of the discharging cycle, V (V) is the discharging potential change, V_{drop} (V) is the voltage drop at the beginning of the discharge, and m (g) is the active mass in a single carbon electrode.

The specific energy, E (Wh kg^{-1}) and specific power, P (W kg^{-1}) of EDLCs were estimated via:

$$E = \frac{1}{8\times3.6}C(V-V_{drop})^2 \tag{6.8}$$

$$P = \frac{E\times3600}{\Delta t} \tag{6.9}$$

where V (V) is the discharging potential change, V_{drop} (V) is the voltage drop at the beginning of the discharge, Δt (s) is the discharging time.

The energy density, E$_V$ (Wh L^{-1}) and power density, P$_V$ (W L^{-1}) of EDLCs were calculated by:

$$E_V = \rho \times E \tag{6.10}$$

$$P_V = \rho \times P \tag{6.11}$$

where ρ (g cm^{-3}) is the density of carbon electrodes, E (Wh kg^{-1}) and P (W kg^{-1}) are the specific energy and the specific power of carbon electrodes, respectively.

For long-term stability tests in organic electrolyte, the cells were charged and discharged by galvanostatic cycling for 10,000 cycles. Afterwards, the voltage was kept at 2.5 V for 100 h, and the specific capacity was measured every 10 h by galvanostatic cycling at 20 A g^{-1}. For long-term stability tests in the IL electrolyte, the voltage of the cell was kept at 3.5 V for 100 h, and the specific capacity was measured every 10 h by galvanostatic cycling at 1 A g^{-1}. In addition, the cycling

stability test is accomplished by charging and discharging the cell at a specific current of 10 A g^{-1} for 10,000 cycles.

Fabrication of NICs and electrochemical measurements

The free-standing film of HAT-CNF was punched into disks of 10 mm in diameter, which were directly used as free-standing working electrodes. The areal loading of an electrode was about 0.5 mg cm^{-2}. To prepare electrodes from powder samples (HAT-850, HAT550@ZTC, HAT550, and ZTC), 80 wt% of the active materials, 10 wt% of carbon black (super-P), 5 wt% of sodium carboxymethyl cellulose (Sigma, average Mw ~250000) and 5 wt% of poly(acrylic acid) (Sigma, average Mw ~450000) were uniformly mixed in Milli-Q water under mechanical stirring. The obtained slurries were transferred onto a copper current collector (10 mm in diameter) and dried at 60 °C overnight. The areal loading of a HAT-850 electrode was about 0.8 mg cm^{-2}. The areal loading of the other electrodes was about 1.5 mg cm^{-2}. The half-cell tests were carried out using Swagelok-type cells assembled in an argon filled glove box (H$_2$O < 0.1 ppm, O$_2$ < 0.1 ppm). Sodium metal foil (11 mm in diameter) was used as both counter and reference electrodes. Glass fibers (Whatman GF/C, 13 mm in diameter) were employed as the separators. The electrolyte was 1 M NaClO$_4$ in ethylene carbonate/propylene carbonate/fluoroethylene carbonate (45:45:10 by mass). The Swagelok cell was assembled using the working and counter electrodes sandwiching the separator, with 300 µL electrolyte and a copper foil as the current collector for the working electrode. A Biologic MPG-2 galvanostat/potentiostat was used for electrochemical characterization. All measurements were performed at room temperature. The electrochemical impedance spectroscopy was performed at open circuit potential with a sinusoidal signal over a frequency range from 20 kHz to 10^{-2} Hz at an amplitude of 10 mV. CV tests were performed at the scan rate of 0.1 mV s^{-1}. GCPL measurement was applied at specific currents between 0.1 and 20 A g^{-1} in a voltage range from 0 to +2.5 V. The specific capacity, Q (mAh g^{-1}), was calculated according to the following equation:

$$Q = \frac{Q_{dis}}{m} \tag{6.12}$$

Where Q_{dis} (mAh) is the charge of the discharging cycle, and m (g) is the mass of the active material in a single electrode.

Full-cell NICs were assembled with STC-16 as the cathode material. The preparation method for the cathode was the same as that for the powder anode preparation (such as HAT-850) except using the aluminum current collector (10 mm in diameter). The weight ratio between the cathode and anode active materials was set to be 2.5:1. The electrolyte and the separator applied in full cells were all the same as those in half cells. The specific capacitance C (F g^{-1}), specific energy E (Wh kg^{-1}), and specific power P (W kg^{-1}) of NICs were calculated via:

$$C = \frac{Q_{dis}}{(V - V_{drop})M} \tag{6.13}$$

$$E = \frac{1}{2 \times 3.6} C(V - V_{drop})^2 \tag{6.14}$$

$$P = \frac{E \times 3600}{\Delta t} \tag{6.15}$$

where M (g) is total mass of the active materials (cathode and anode), V (V) is the discharging potential change, V_{drop} (V) is the voltage drop at the beginning of the discharge, Δt (s) is the discharging time.

For long-term stability tests, the full cells were charged and discharged by galvanostatic cycling for 1,000 cycles at 1 A g^{-1}.

7. References

1. United Nations, Department of Economic and Social Affairs, Population Division (2017), "World Population Prospects: The 2017 Revision". **2018.**

2. Conti, J.; Holtberg, P.; Diefenderfer, J.; LaRose, A.; Turnure, J. T.; Westfall, L. *International energy outlook 2016 with projections to 2040*; USDOE Energy Information Administration (EIA), Washington, DC (United States). **2016.**

3. Chen, C.-C.; Maier, J. Decoupling electron and ion storage and the path from interfacial storage to artificial electrodes. *Nat. Energy* **2018,** *3*, 102-108.

4. Nayak, P. K.; Yang, L. T.; Brehm, W.; Adelhelm, P. From Lithium-Ion to Sodium-Ion Batteries: Advantages, Challenges, and Surprises. *Angew Chem Int Edit* **2018,** *57*, 102-120.

5. Liu, J. L.; Wang, J.; Xu, C. H.; Jiang, H.; Li, C. Z.; Zhang, L. L.; Lin, J. Y.; Shen, Z. X. Advanced Energy Storage Devices: Basic Principles, Analytical Methods, and Rational Materials Design. *Adv. Sci.* **2018,** *5*.

6. Carol Weis, C. F. Net Metering & Beyond. https://www.homepower.com/articles/solar-electricity/design-installation/net-metering-beyond/page/0/2?v=print.

7. Forse, A. C.; Griffin, J. M.; Merlet, C.; Bayley, P. M.; Wang, H.; Simon, P.; Grey, C. P. NMR Study of Ion Dynamics and Charge Storage in Ionic Liquid Supercapacitors. *J. Am. Chem. Soc.* **2015,** *137*, 7231-42.

8. Zhang, C.; Lv, W.; Tao, Y.; Yang, Q. H. Towards superior volumetric performance: design and preparation of novel carbon materials for energy storage. *Energy Environ. Sci.* **2015,** *8*, 1390-1403.

9. Liu, T. Y.; Zhang, F.; Song, Y.; Li, Y. Revitalizing carbon supercapacitor electrodes with hierarchical porous structures. *J. Mater. Chem. A* **2017,** *5*, 17705-17733.

10. Zeiger, M.; Jackel, N.; Mochalin, V. N.; Presser, V. Review: carbon onions for electrochemical energy storage. *J. Mater. Chem. A* **2016,** *4*, 3172-3196.

11. Benzigar, M. R.; Talapaneni, S. N.; Joseph, S.; Ramadass, K.; Singh, G.; Scaranto, J.; Ravon, U.; Al-Bahily, K.; Vinu, A. Recent advances in functionalized micro and mesoporous carbon materials: synthesis and applications. *Chem. Soc. Rev.* **2018,** *47*, 2680-2721.

12. Landi, B. J.; Ganter, M. J.; Cress, C. D.; DiLeo, R. A.; Raffaelle, R. P. Carbon nanotubes for lithium ion batteries. *Energy Environ. Sci.* **2009,** *2*, 638-654.

13. Rehman, S.; Khan, K.; Zhao, Y. F.; Hou, Y. L. Nanostructured cathode materials for lithium-sulfur batteries: progress, challenges and perspectives. *J. Mater. Chem. A* **2017,** *5*, 3014-3038.

14. Hou, H. S.; Qiu, X. Q.; Wei, W. F.; Zhang, Y.; Ji, X. B. Carbon Anode Materials for Advanced Sodium-Ion Batteries. *Adv. Energy Mater.* **2017,** *7*.

15. Cohn, A. P.; Muralidharan, N.; Carter, R.; Share, K.; Pint, C. L. Anode-Free Sodium Battery through in Situ Plating of Sodium Metal. *Nano Lett.* **2017,** *17*, 1296-1301.

16. Roston, E., *The Carbon Age: How Life's Core Element Has Become Civilization's Greatest Threat*. DIANE Publishing Company: 2011.

17. Greenwood, N. N.; Earnshaw, A. Chemistry of the Elements. **1984.**

18. Titirici, M. M.; White, R. J.; Brun, N.; Budarin, V. L.; Su, D. S.; del Monte, F.; Clark, J. H.; MacLachlan, M. J. Sustainable carbon materials. *Chem. Soc. Rev.* **2015,** *44*, 250-290.

19. Rao, C. N. R.; Sood, A. K.; Subrahmanyam, K. S.; Govindaraj, A. Graphene: The New Two-Dimensional Nanomaterial. *Angew Chem Int Edit* **2009,** *48*, 7752-7777.

20. Avouris, P.; Freitag, M.; Perebeinos, V. Carbon-nanotube photonics and optoelectronics. *Nat. Photonics* **2008,** *2*, 341-350.

21. Kozyrev, S. V.; Rotkin, V. V. Fullerene - Structure, Crystal-Lattice Dynamics, Electron-Structure, and Properties (a Review). *Semiconductors* **1993,** *27*, 777-791.

22. Allotropes of carbon. https://en.wikipedia.org/wiki/Allotropes_of_carbon.

23. Stein, A.; Wang, Z. Y.; Fierke, M. A. Functionalization of Porous Carbon Materials with Designed Pore Architecture. *Adv. Mater.* **2009,** *21*, 265-293.

24. Zhai, Y. P.; Dou, Y. Q.; Zhao, D. Y.; Fulvio, P. F.; Mayes, R. T.; Dai, S. Carbon Materials for Chemical Capacitive Energy Storage. *Adv. Mater.* **2011,** *23*, 4828-4850.

25. Yao, F.; Pham, D. T.; Lee, Y. H. Carbon-Based Materials for Lithium-Ion Batteries, Electrochemical Capacitors, and Their Hybrid Devices. *ChemSusChem* **2015,** *8*, 2284-2311.

26. Ghosh, A.; Lee, Y. H. Carbon-Based Electrochemical Capacitors. *ChemSusChem* **2012,** *5*, 480-499.

27. Liu, J.; Wickramaratne, N. P.; Qiao, S. Z.; Jaroniec, M. Molecular-based design and emerging applications of nanoporous carbon spheres. *Nat. Mater.* **2015,** *14*, 763-774.

28. Borchardt, L.; Oschatz, M.; Kaskel, S. Tailoring porosity in carbon materials for supercapacitor applications. *Mater. Horiz.* **2014,** *1*, 157-168.

29. Thommes, M.; Kaneko, K.; Neimark, A. V.; Olivier, J. P.; Rodriguez-Reinoso, F.; Rouquerol, J.; Sing, K. S. W. Physisorption of gases, with special reference to the evaluation of surface area and pore size distribution (IUPAC Technical Report). *Pure Appl. Chem.* **2015,** *87*.

30. Chmiola, J.; Yushin, G.; Gogotsi, Y.; Portet, C.; Simon, P.; Taberna, P. L. Anomalous increase in carbon capacitance at pore sizes less than 1 nanometer. *Science* **2006,** *313*, 1760-3.

31. Sevilla, M.; Mokaya, R. Energy storage applications of activated carbons: supercapacitors and hydrogen storage. *Energy Environ. Sci.* **2014,** *7*, 1250-1280.

32. Linares-Solano, A.; de Lecea, C. S. M.; Cazorla-Amoros, D.; Martin-Gullon, I. Porosity development during CO_2 and steam activation in a fluidized bed reactor. *Energy Fuels* **2000,** *14*, 142-149.

33. Wang, J.; Kaskel, S. KOH activation of carbon-based materials for energy storage. *J. Mater. Chem.* **2012,** *22*, 23710.

34. Rodriguezreinoso, F.; Molinasabio, M. Activated Carbons from Lignocellulosic Materials by Chemical and or Physical Activation - an Overview. *Carbon* **1992,** *30*, 1111-1118.

35. Stevens, D. A.; Dahn, J. R. High capacity anode materials for rechargeable sodium-ion batteries. *J. Electrochem. Soc.* **2000,** *147*, 1271-1273.

36. Gu, W. T.; Yushin, G. Review of nanostructured carbon materials for electrochemical capacitor applications: advantages and limitations of activated carbon, carbide-derived carbon, zeolite-templated carbon, carbon aerogels, carbon nanotubes, onion-like carbon, and graphene. *Wires Energy Environ* **2014,** *3*, 424-473.

37. Sakintuna, B.; Yurum, Y. Templated porous carbons: A review article. *Ind. Eng. Chem. Res.* **2005,** *44*, 2893-2902.

38. Xia, Y. D.; Yang, Z. X.; Mokaya, R. Templated nanoscale porous carbons. *Nanoscale* **2010,** *2,* 639-659.

39. Yang, X. Y.; Chen, L. H.; Li, Y.; Rooke, J. C.; Sanchez, C.; Su, B. L. Hierarchically porous materials: synthesis strategies and structure design. *Chem. Soc. Rev.* **2017,** *46,* 481-558.

40. Jun, S.; Joo, S. H.; Ryoo, R.; Kruk, M.; Jaroniec, M.; Liu, Z.; Ohsuna, T.; Terasaki, O. Synthesis of new, nanoporous carbon with hexagonally ordered mesostructure. *J. Am. Chem. Soc.* **2000,** *122,* 10712-10713.

41. Saikia, D.; Wang, T. H.; Chou, C. J.; Fang, J.; Tsai, L. D.; Kao, H. M. A comparative study of ordered mesoporous carbons with different pore structures as anode materials for lithium-ion batteries. *Rsc Adv* **2015,** *5,* 42922-42930.

42. Strubel, P.; Thieme, S.; Biemelt, T.; Helmer, A.; Oschatz, M.; Brückner, J.; Althues, H.; Kaskel, S. ZnO Hard Templating for Synthesis of Hierarchical Porous Carbons with Tailored Porosity and High Performance in Lithium-Sulfur Battery. *Adv. Funct. Mater.* **2015,** *25,* 287-297.

43. Libbrecht, W.; Verberckmoes, A.; Thybaut, J. W.; Van der Voort, P.; De Clercq, J. Soft templated mesoporous carbons: Tuning the porosity for the adsorption of large organic pollutants. *Carbon* **2017,** *116,* 528-546.

44. Gu, D.; Schuth, F. Synthesis of non-siliceous mesoporous oxides. *Chem. Soc. Rev.* **2014,** *43,* 313-344.

45. Zhang, F. Q.; Meng, Y.; Gu, D.; Yan, Y.; Yu, C. Z.; Tu, B.; Zhao, D. Y. A facile aqueous route to synthesize highly ordered mesoporous polymers and carbon frameworks with Ia(3)over-bard bicontinuous cubic structure. *J. Am. Chem. Soc.* **2005,** *127,* 13508-13509.

46. Liu, X. F.; Fechler, N.; Antonietti, M. Salt melt synthesis of ceramics, semiconductors and carbon nanostructures. *Chem. Soc. Rev.* **2013,** *42,* 8237-8265.

47. Liu, X.; Giordano, C.; Antonietti, M. A Facile Molten‐Salt Route to Graphene Synthesis. *Small* **2014,** *10,* 193-200.

48. Fechler, N.; Fellinger, T. P.; Antonietti, M. "Salt templating": a simple and sustainable pathway toward highly porous functional carbons from ionic liquids. *Adv. Mater.* **2013,** *25,* 75-79.

49. Deng, Y. F.; Xie, Y.; Zou, K. X.; Ji, X. L. Review on recent advances in nitrogen-doped carbons: preparations and applications in supercapacitors. *J. Mater. Chem. A* **2016,** *4,* 1144-1173.

50. Ong, W. J.; Tan, L. L.; Ng, Y. H.; Yong, S. T.; Chai, S. P. Graphitic Carbon Nitride (g-C3N4)-Based Photocatalysts for Artificial Photosynthesis and Environmental Remediation: Are We a Step Closer To Achieving Sustainability? *Chem. Rev.* **2016,** *116,* 7159-7329.

51. Xu, J. T.; Mahmood, J.; Dou, Y. H.; Dou, S. X.; Li, F.; Dai, L. M.; Baek, J. B. 2D Frameworks of C2N and C3N as New Anode Materials for Lithium-Ion Batteries. *Adv. Mater.* **2017,** *29,* 1702007.

52. Wei, Q. L.; Tong, X.; Zhang, G. X.; Qiao, J. L.; Gong, Q. J.; Sun, S. H. Nitrogen-Doped Carbon Nanotube and Graphene Materials for Oxygen Reduction Reactions. *Catalysts* **2015,** *5,* 1574-1602.

53. Simon, P.; Gogotsi, Y. Materials for electrochemical capacitors. *Nat. Mater.* **2008,** *7,* 845-854.

54. Conway, B. E., *Electrochemical supercapacitors: scientific fundamentals and technological applications.* Springer Science & Business Media: 2013.

55. Yu, A. P.; Chen, Z. W.; Maric, R.; Zhang, L.; Zhang, J. J.; Yan, J. Y. Electrochemical supercapacitors for energy storage and delivery: Advanced materials, technologies and applications. *Appl. Energy* **2015,** *153*, 1-2.

56. Capacitor. https://en.wikipedia.org/w/index.php?title=Capacitor&oldid=874292781.

57. Salanne, M.; Rotenberg, B.; Naoi, K.; Kaneko, K.; Taberna, P. L.; Grey, C. P.; Dunn, B.; Simon, P. Efficient storage mechanisms for building better supercapacitors. *Nat. Energy* **2016,** *1*, 16070.

58. Zhang, H.; Cao, G.; Yang, Y.; Gu, Z. Capacitive performance of an ultralong aligned carbon nanotube electrode in an ionic liquid at 60℃. *Carbon* **2008,** *46*, 30-34.

59. Korenblit, Y.; Kajdos, A.; West, W. C.; Smart, M. C.; Brandon, E. J.; Kvit, A.; Jagiello, J.; Yushin, G. In Situ Studies of Ion Transport in Microporous Supercapacitor Electrodes at Ultralow Temperatures. *Adv. Funct. Mater.* **2012,** *22*, 1655-1662.

60. Kotz, R.; Carlen, M. Principles and applications of electrochemical capacitors. *Electrochim. Acta* **2000,** *45*, 2483-2498.

61. Miller, J. R.; Simon, P. Materials science - Electrochemical capacitors for energy management. *Science* **2008,** *321*, 651-652.

62. Gu, W.; Yushin, G. Review of nanostructured carbon materials for electrochemical capacitor applications: advantages and limitations of activated carbon, carbide-derived carbon, zeolite-templated carbon, carbon aerogels, carbon nanotubes, onion-like carbon, and graphene. *WIREs. Energy Environ.* **2014,** *3*, 424-473.

63. Yu, Z.; Tetard, L.; Zhai, L.; Thomas, J. Supercapacitor electrode materials: nanostructures from 0 to 3 dimensions. *Energy Environ. Sci.* **2015,** *8*, 702-730.

64. Chmiola, J.; Largeot, C.; Taberna, P. L.; Simon, P.; Gogotsi, Y. Desolvation of ions in subnanometer pores and its effect on capacitance and double-layer theory. *Angew. Chem. Int. Ed. Engl.* **2008,** *47*, 3392-5.

65. Jäckel, N.; Simon, P.; Gogotsi, Y.; Presser, V. Increase in Capacitance by Subnanometer Pores in Carbon. *ACS Energy Letters* **2016,** *1*, 1262-1265.

66. Raymundo-Piñero, E.; Kierzek, K.; Machnikowski, J.; Béguin, F. Relationship between the nanoporous texture of activated carbons and their capacitance properties in different electrolytes. *Carbon* **2006,** *44*, 2498-2507.

67. Liu, H.-J.; Wang, J.; Wang, C.-X.; Xia, Y.-Y. Ordered Hierarchical Mesoporous/Microporous Carbon Derived from Mesoporous Titanium-Carbide/Carbon Composites and its Electrochemical Performance in Supercapacitor. *Adv. Energy Mater.* **2011,** *1*, 1101-1108.

68. Rose, M.; Korenblit, Y.; Kockrick, E.; Borchardt, L.; Oschatz, M.; Kaskel, S.; Yushin, G. Hierarchical micro- and mesoporous carbide-derived carbon as a high-performance electrode material in supercapacitors. *Small* **2011,** *7*, 1108-17.

69. Oschatz, M.; Kockrick, E.; Rose, M.; Borchardt, L.; Klein, N.; Senkovska, I.; Freudenberg, T.; Korenblit, Y.; Yushin, G.; Kaskel, S. A cubic ordered, mesoporous carbide-derived carbon for gas and energy storage applications. *Carbon* **2010,** *48*, 3987-3992.

70. Oschatz, M.; Borchardt, L.; Pinkert, K.; Thieme, S.; Lohe, M. R.; Hoffmann, C.; Benusch, M.; Wisser, F. M.; Ziegler, C.; Giebeler, L.; Rummeli, M. H.; Eckert, J.; Eychmuller, A.; Kaskel, S. Hierarchical Carbide-Derived Carbon Foams with Advanced Mesostructure as a Versatile Electrochemical Energy-Storage Material. *Adv. Energy Mater.* **2014,** *4*.

71.   Paraknowitsch, J. P.; Thomas, A. Doping carbons beyond nitrogen: an overview of advanced heteroatom doped carbons with boron, sulphur and phosphorus for energy applications. *Energy Environ. Sci.* **2013,** *6*, 2839-2855.

72.   Xu, Z. F.; Chen, J. L.; Zhang, X.; Song, Q.; Wu, J.; Ding, L.; Zhang, C. Z.; Zhu, H. L.; Cui, H. Z. Template-free preparation of nitrogen-doped activated carbon with porous architecture for high-performance supercapacitors. *Microporous Mesoporous Mater.* **2019,** *276*, 280-291.

73.   Majumder, M.; Choudhary, R. B.; Thakur, A. K. Hemispherical nitrogen-doped carbon spheres integrated with polyindole as high performance electrode material for supercapacitor applications. *Carbon* **2019,** *142*, 650-661.

74.   Men, B.; Guo, P. K.; Sun, Y. Z.; Tang, Y.; Chen, Y. M.; Pan, J. Q.; Wan, P. Y. High-performance nitrogen-doped hierarchical porous carbon derived from cauliflower for advanced supercapacitors. *J. Mater. Sci.* **2019,** *54*, 2446-2457.

75.   Wang, Y.; Song, Y.; Xia, Y. Electrochemical capacitors: mechanism, materials, systems, characterization and applications. *Chem. Soc. Rev.* **2016,** *45*, 5925-5950.

76.   Beguin, F.; Presser, V.; Balducci, A.; Frackowiak, E. Carbons and Electrolytes for Advanced Supercapacitors. *Adv. Mater.* **2014,** *26*, 2219-2251.

77.   Eftekhari, A. Supercapacitors utilising ionic liquids. *Energy Storage Mater.* **2017,** *9*, 47-69.

78.   Antonietti, M.; Chen, X.; Yan, R.; Oschatz, M. Storing electricity as chemical energy: beyond traditional electrochemistry and double-layer compression. *Energy Environ. Sci.* **2018,** *11*, 3069-3074.

79.   Han, P. X.; Xu, G. J.; Han, X. Q.; Zhao, J. W.; Zhou, X. H.; Cui, G. L. Lithium Ion Capacitors in Organic Electrolyte System: Scientific Problems, Material Development, and Key Technologies. *Adv. Energy Mater.* **2018,** *8*, 1801243.

80.   Wang, H.; Zhu, C.; Chao, D.; Yan, Q.; Fan, H. J. Nonaqueous Hybrid Lithium-Ion and Sodium-Ion Capacitors. *Adv. Mater.* **2017,** *29*, 1702093.

81.   Hou, H. S.; Qiu, X. Q.; Wei, W. F.; Zhang, Y.; Ji, X. B. Carbon Anode Materials for Advanced Sodium-Ion Batteries. *Adv. Energy Mater.* **2017,** *7*, 1602898.

82.   Balogun, M. S.; Luo, Y.; Qiu, W. T.; Liu, P.; Tong, Y. X. A review of carbon materials and their composites with alloy metals for sodium ion battery anodes. *Carbon* **2016,** *98*, 162-178.

83.   Tang, K.; Fu, L. J.; White, R. J.; Yu, L. H.; Titirici, M. M.; Antonietti, M.; Maier, J. Hollow Carbon Nanospheres with Superior Rate Capability for Sodium-Based Batteries. *Adv. Energy Mater.* **2012,** *2*, 873-877.

84.   Wenzel, S.; Hara, T.; Janek, J.; Adelhelm, P. Room-temperature sodium-ion batteries: Improving the rate capability of carbon anode materials by templating strategies. *Energy Environ. Sci.* **2011,** *4*, 3342-3345.

85.   Li, Z.; Ding, J.; Mitlin, D. Tin and Tin Compounds for Sodium Ion Battery Anodes: Phase Transformations and Performance. *Acc. Chem. Res.* **2015,** *48*, 1657-1665.

86.   Zhang, N.; Han, X. P.; Liu, Y. C.; Hu, X. F.; Zhao, Q.; Chen, J. 3D Porous gamma-Fe2O3@C Nanocomposite as High-Performance Anode Material of Na-Ion Batteries. *Adv. Energy Mater.* **2015,** *5*, 1401123.

87.   Lim, E.; Jo, C.; Kim, M. S.; Kim, M.-H.; Chun, J.; Kim, H.; Park, J.; Roh, K. C.; Kang, K.; Yoon, S.; Lee, J. High-Performance Sodium-Ion Hybrid Supercapacitor Based on Nb2O5@Carbon

Core-Shell Nanoparticles and Reduced Graphene Oxide Nanocomposites. *Adv. Funct. Mater.* **2016,** *26*, 3711-3719.

88.   Geng, P. B.; Zheng, S. S.; Tang, H.; Zhu, R. M.; Zhang, L.; Cao, S.; Xue, H. G.; Pang, H. Transition Metal Sulfides Based on Graphene for Electrochemical Energy Storage. *Adv. Energy Mater.* **2018,** *8*, 1703259.

89.   Hu, Z.; Liu, Q. N.; Chou, S. L.; Dou, S. X. Advances and Challenges in Metal Sulfides/Selenides for Next-Generation Rechargeable Sodium-Ion Batteries. *Adv. Mater.* **2017,** *29*, 1700606.

90.   Xiao, Y.; Lee, S. H.; Sun, Y. K. The Application of Metal Sulfides in Sodium Ion Batteries. *Adv. Energy Mater.* **2017,** *7*, 1601329.

91.   Li, F.; Zhou, Z. Micro/Nanostructured Materials for Sodium Ion Batteries and Capacitors. *Small* **2018,** *14*.

92.   Shi, L.; Zhao, T. S. Recent advances in inorganic 2D materials and their applications in lithium and sodium batteries. *J. Mater. Chem. A* **2017,** *5*, 3735-3758.

93.   Lu, P.; Sun, Y.; Xiang, H.; Liang, X.; Yu, Y. 3D Amorphous Carbon with Controlled Porous and Disordered Structures as a High-Rate Anode Material for Sodium-Ion Batteries. *Adv. Energy Mater.* **2018,** *8*, 1702434.

94.   Stevens, D. A.; Dahn, J. R. The mechanisms of lithium and sodium insertion in carbon materials. *J. Electrochem. Soc.* **2001,** *148*, A803-A811.

95.   Zhang, B. A.; Ghimbeu, C. M.; Laberty, C.; Vix-Guterl, C.; Tarascon, J. M. Correlation Between Microstructure and Na Storage Behavior in Hard Carbon. *Adv. Energy Mater.* **2016,** *6*, 1501588.

96.   Cao, Y. L.; Xiao, L. F.; Sushko, M. L.; Wang, W.; Schwenzer, B.; Xiao, J.; Nie, Z. M.; Saraf, L. V.; Yang, Z. G.; Liu, J. Sodium Ion Insertion in Hollow Carbon Nanowires for Battery Applications. *Nano Lett.* **2012,** *12*, 3783-3787.

97.   Ding, J.; Wang, H. L.; Li, Z.; Kohandehghan, A.; Cui, K.; Xu, Z. W.; Zahiri, B.; Tan, X. H.; Lotfabad, E. M.; Olsen, B. C.; Mitlin, D. Carbon Nanosheet Frameworks Derived from Peat Moss as High Performance Sodium Ion Battery Anodes. *ACS Nano* **2013,** *7*, 11004-11015.

98.   Bommier, C.; Surta, T. W.; Dolgos, M.; Ji, X. L. New Mechanistic Insights on Na-Ion Storage in Nongraphitizable Carbon. *Nano Lett.* **2015,** *15*, 5888-5892.

99.   Liu, R.; Shi, Y.; Wan, Y.; Meng, Y.; Zhang, F.; Gu, D.; Chen, Z.; Tu, B.; Zhao, D. Triconstituent co-assembly to ordered mesostructured polymer– silica and carbon– silica nanocomposites and large-pore mesoporous carbons with high surface areas. *J. Am. Chem. Soc.* **2006,** *128*, 11652-11662.

100. Jin, J.; Tanaka, S.; Egashira, Y.; Nishiyama, N. KOH activation of ordered mesoporous carbons prepared by a soft-templating method and their enhanced electrochemical properties. *Carbon* **2010,** *48*, 1985-1989.

101. Lv, Y.; Zhang, F.; Dou, Y.; Zhai, Y.; Wang, J.; Liu, H.; Xia, Y.; Tu, B.; Zhao, D. A comprehensive study on KOH activation of ordered mesoporous carbons and their supercapacitor application. *J. Mater. Chem.* **2012,** *22*, 93-99.

102. Oschatz, M.; Borchardt, L.; Pinkert, K.; Thieme, S.; Lohe, M. R.; Hoffmann, C.; Benusch, M.; Wisser, F. M.; Ziegler, C.; Giebeler, L.; Rümmeli, M. H.; Eckert, J.; Eychmüller, A.; Kaskel, S.

Hierarchical Carbide-Derived Carbon Foams with Advanced Mesostructure as a Versatile Electrochemical Energy-Storage Material. *Adv. Energy Mater.* **2014,** *4*, 1300645.

103. Fechler, N.; Fellinger, T. P.; Antonietti, M. "Salt templating": a simple and sustainable pathway toward highly porous functional carbons from ionic liquids. *Adv. Mater.* **2013,** *25*, 75-9.

104. Porada, S.; Schipper, F.; Aslan, M.; Antonietti, M.; Presser, V.; Fellinger, T. P. Capacitive Deionization using Biomass-based Microporous Salt-Templated Heteroatom-Doped Carbons. *ChemSusChem* **2015,** *8*, 1867-74.

105. Davenport, M.; Rodriguez, A.; Shea, K. J.; Siwy, Z. S. Squeezing Ionic Liquids through Nanopores. *Nano Lett.* **2009,** *9*, 2125-2128.

106. Pean, C.; Merlet, C.; Rotenberg, B.; Madden, P. A.; Taberna, P. L.; Daffos, B.; Salanne, M.; Simon, P. On the Dynamics of Charging in Nanoporous Carbon-Based Supercapacitors. *ACS Nano* **2014,** *8*, 1576-1583.

107. Rajput, N. N.; Monk, J.; Singh, R.; Hung, F. R. On the Influence of Pore Size and Pore Loading on Structural and Dynamical Heterogeneities of an Ionic Liquid Confined in a Slit Nanopore. *J. Phys. Chem. C* **2012,** *116*, 5170-5182.

108. He, Y. D.; Qiao, R.; Vatamanu, J.; Borodin, O.; Bedrov, D.; Huang, J. S.; Sumpter, B. G. Importance of Ion Packing on the Dynamics of Ionic Liquids during Micropore Charging. *J Phys Chem Lett* **2016,** *7*, 36-42.

109. Kondrat, S.; Wu, P.; Qiao, R.; Kornyshev, A. A. Accelerating charging dynamics in subnanometre pores. *Nat. Mater.* **2014,** *13*, 387-393.

110. Kondrat, S.; Kornyshev, A. A. Pressing a spring: what does it take to maximize the energy storage in nanoporous supercapacitors? *Nanoscale Horiz* **2016,** *1*, 45-52.

111. Iacob, C.; Sangoro, J. R.; Papadopoulos, P.; Schubert, T.; Naumov, S.; Valiullin, R.; Karger, J.; Kremer, F. Charge transport and diffusion of ionic liquids in nanoporous silica membranes. *Phys. Chem. Chem. Phys.* **2010,** *12*, 13798-13803.

112. Singh, R.; Monk, J.; Hung, F. R. Heterogeneity in the Dynamics of the Ionic Liquid [BMIM+][PF6-] Confined in a Slit Nanopore. *J. Phys. Chem. C* **2011,** *115*, 16544-16554.

113. Singh, R.; Rajput, N. N.; He, X. X.; Monk, J.; Hung, F. R. Molecular dynamics simulations of the ionic liquid [EMIM+][TFMSI-] confined inside rutile (110) slit nanopores. *Phys. Chem. Chem. Phys.* **2013,** *15*, 16090-16103.

114. Monk, J.; Singh, R.; Hung, F. R. Effects of Pore Size and Pore Loading on the Properties of Ionic Liquids Confined Inside Nanoporous CMK-3 Carbon Materials. *J. Phys. Chem. C* **2011,** *115*, 3034-3042.

115. He, Y. D.; Huang, J. S.; Sumpter, B. G.; Kornyshev, A. A.; Qiao, R. Dynamic Charge Storage in Ionic Liquids-Filled Nanopores: Insight from a Computational Cyclic Voltammetry Study. *J Phys Chem Lett* **2015,** *6*, 22-30.

116. Rajput, N. N.; Monk, J.; Hung, F. R. Structure and Dynamics of an Ionic Liquid Confined Inside a Charged Slit Graphitic Nanopore. *J. Phys. Chem. C* **2012,** *116*, 14504-14513.

117. Oschatz, M.; Boukhalfa, S.; Nickel, W.; Lee, J. T.; Klosz, S.; Borchardt, L.; Eychmuller, A.; Yushin, G.; Kaskel, S. Kroll-carbons based on silica and alumina templates as high-rate electrode materials in electrochemical double-layer capacitors. *J. Mater. Chem. A* **2014,** *2*, 5131-5139.

118. Yan, R.; Heil, T.; Presser, V.; Walczak, R.; Antonietti, M.; Oschatz, M. Ordered Mesoporous Carbons with High Micropore Content and Tunable Structure Prepared by Combined Hard and Salt Templating as Electrode Materials in Electric Double-Layer Capacitors. *Advanced Sustainable Systems* **2017**, 1700128.

119. Oschatz, M.; Boukhalfa, S.; Nickel, W.; Hofmann, J. P.; Fischer, C.; Yushin, G.; Kaskel, S. Carbide-derived carbon aerogels with tunable pore structure as versatile electrode material in high power supercapacitors. *Carbon* **2017,** *113*, 283-291.

120. Forse, A. C.; Merlet, C.; Allan, P. K.; Humphreys, E. K.; Griffin, J. M.; Aslan, M.; Zeiger, M.; Presser, V.; Gogotsi, Y.; Grey, C. P. New insights into the structure of nanoporous carbons from NMR, Raman, and pair distribution function analysis. *Chem. Mater.* **2015,** *27*, 6848-6857.

121. Hou, J. H.; Cao, C. B.; Idrees, F.; Ma, X. L. Hierarchical Porous Nitrogen-Doped Carbon Nanosheets Derived from Silk for Ultrahigh-Capacity Battery Anodes and Supercapacitors. *ACS Nano* **2015,** *9*, 2556-2564.

122. Ewert, J.-K.; Weingarth, D.; Denner, C.; Friedrich, M.; Zeiger, M.; Schreiber, A.; Jäckel, N.; Presser, V.; Kempe, R. Enhanced capacitance of nitrogen-doped hierarchically porous carbide-derived carbon in matched ionic liquids. *J. Mater. Chem. A* **2015,** *3*, 18906-18912.

123. Wu, P.; Huang, J. S.; Meunier, V.; Sumpter, B. G.; Qiao, R. Voltage Dependent Charge Storage Modes and Capacity in Subnanometer Pores. *J Phys Chem Lett* **2012,** *3*, 1732-1737.

124. Levi, M. D.; Levy, N.; Sigalov, S.; Salitra, G.; Aurbach, D.; Maier, J. Electrochemical quartz crystal microbalance (EQCM) studies of ions and solvents insertion into highly porous activated carbons. *J. Am. Chem. Soc.* **2010,** *132*, 13220-13222.

125. Tsai, W.-Y.; Taberna, P.-L.; Simon, P. Electrochemical quartz crystal microbalance (EQCM) study of ion dynamics in nanoporous carbons. *J. Am. Chem. Soc.* **2014,** *136*, 8722-8728.

126. Richey, F. W.; Dyatkin, B.; Gogotsi, Y.; Elabd, Y. A. Ion dynamics in porous carbon electrodes in supercapacitors using in situ infrared spectroelectrochemistry. *J. Am. Chem. Soc.* **2013,** *135*, 12818-12826.

127. Forse, A. C.; Merlet, C.; Griffin, J. M.; Grey, C. P. New Perspectives on the Charging Mechanisms of Supercapacitors. *J. Am. Chem. Soc.* **2016,** *138*, 5731-5744.

128. Jiang, D. E.; Wu, J. Z. Microscopic Insights into the Electrochemical Behavior of Nonaqueous Electrolytes in Electric Double-Layer Capacitors. *J Phys Chem Lett* **2013,** *4*, 1260-1267.

129. Merlet, C.; Rotenberg, B.; Madden, P. A.; Taberna, P. L.; Simon, P.; Gogotsi, Y.; Salanne, M. On the molecular origin of supercapacitance in nanoporous carbon electrodes. *Nat. Mater.* **2012,** *11*, 306-310.

130. Kondrat, S.; Perez, C. R.; Presser, V.; Gogotsi, Y.; Kornyshev, A. A. Effect of pore size and its dispersity on the energy storage in nanoporous supercapacitors. *Energy Environ. Sci.* **2012,** *5*, 6474-6479.

131. Shim, Y.; Kim, H. J. Nanoporous Carbon Supercapacitors in an Ionic Liquid: A Computer Simulation Study. *ACS Nano* **2010,** *4*, 2345-2355.

132. Largeot, C.; Portet, C.; Chmiola, J.; Taberna, P.-L.; Gogotsi, Y.; Simon, P. Relation between the ion size and pore size for an electric double-layer capacitor. *J. Am. Chem. Soc.* **2008,** *130*, 2730-2731.

133. Oschatz, M.; Pré, P.; Dörfler, S.; Nickel, W.; Beaunier, P.; Rouzaud, J.-N.; Fischer, C.; Brunner, E.; Kaskel, S. Nanostructure characterization of carbide-derived carbons by morphological analysis of transmission electron microscopy images combined with physisorption and Raman spectroscopy. *Carbon* **2016**, *105*, 314-322.

134. Osswald, S.; Chmiola, J.; Gogotsi, Y. Structural evolution of carbide-derived carbons upon vacuum annealing. *Carbon* **2012**, *50*, 4880-4886.

135. Pawlyta, M.; Rouzaud, J.-N.; Duber, S. Raman microspectroscopy characterization of carbon blacks: Spectral analysis and structural information. *Carbon* **2015**, *84*, 479-490.

136. Kornyshev, A. A. Double-layer in ionic liquids: Paradigm change? *J. Phys. Chem. B* **2007**, *111*, 5545-5557.

137. Salanne, M. Ionic Liquids for Supercapacitor Applications. *Top. Curr. Chem.* **2017**, *375*, 63.

138. Wei, L.; Sevilla, M.; Fuertes, A. B.; Mokaya, R.; Yushin, G. Polypyrrole-Derived Activated Carbons for High-Performance Electrical Double-Layer Capacitors with Ionic Liquid Electrolyte. *Adv. Funct. Mater.* **2012**, *22*, 827-834.

139. Vu, A.; Li, X.; Phillips, J.; Han, A.; Smyrl, W. H.; Bühlmann, P.; Stein, A. Three-Dimensionally Ordered Mesoporous (3DOm) Carbon Materials as Electrodes for Electrochemical Double-Layer Capacitors with Ionic Liquid Electrolytes. *Chem. Mater.* **2013**, *25*, 4137-4148.

140. Fechler, N.; Wohlgemuth, S.-A.; Jäker, P.; Antonietti, M. Salt and sugar: direct synthesis of high surface area carbon materials at low temperatures via hydrothermal carbonization of glucose under hypersaline conditions. *J. Mater. Chem. A* **2013**, *1*, 9418.

141. Zhong, J.; Deng, J. J.; Mao, B. H.; Xie, T.; Sun, X. H.; Mou, Z. G.; Hong, C. H.; Yang, P.; Wang, S. D. Probing solid state N-doping in graphene by X-ray absorption near-edge structure spectroscopy. *Carbon* **2012**, *50*, 335-338.

142. Li, M.; Li, W.; Liu, S. X. Hydrothermal synthesis, characterization, and KOH activation of carbon spheres from glucose. *Carbohydr. Res.* **2011**, *346*, 999-1004.

143. Yang, J.; Wu, H.; Zhu, M.; Ren, W.; Lin, Y.; Chen, H.; Pan, F. Optimized mesopores enabling enhanced rate performance in novel ultrahigh surface area meso-/microporous carbon for supercapacitors. *Nano Energy* **2017**, *33*, 453-461.

144. Simon, P.; Gogotsi, Y. Capacitive energy storage in nanostructured carbon–electrolyte systems. *Acc. Chem. Res.* **2012**, *46*, 1094-1103.

145. Weingarth, D.; Noh, H.; Foelske-Schmitz, A.; Wokaun, A.; Kötz, R. A reliable determination method of stability limits for electrochemical double layer capacitors. *Electrochim. Acta* **2013**, *103*, 119-124.

146. Zhou, Y.; Schattka, J. H.; Antonietti, M. Room-temperature ionic liquids as template to monolithic mesoporous silica with wormlike pores via a sol-gel nanocasting technique. *Nano Lett.* **2004**, *4*, 477-481.

147. Xu, J. T.; Wang, M.; Wickramaratne, N. P.; Jaroniec, M.; Dou, S. X.; Dai, L. M. High-Performance Sodium Ion Batteries Based on a 3D Anode from Nitrogen-Doped Graphene Foams. *Adv. Mater.* **2015**, *27*, 2042-2048.

148. Wang, S.; Xia, L.; Yu, L.; Zhang, L.; Wang, H.; Lou, X. W. D. Free‐Standing Nitrogen‐Doped Carbon Nanofiber Films: Integrated Electrodes for Sodium‐Ion Batteries with Ultralong Cycle Life and Superior Rate Capability. *Adv. Energy Mater.* **2016**, *6*, 1502217.

149. Huo, K. F.; An, W. L.; Fu, J. J.; Gao, B.; Wang, L.; Peng, X.; Cheng, G. J.; Chu, P. K. Mesoporous nitrogen-doped carbon hollow spheres as high-performance anodes for lithium-ion batteries. *J. Power Sources* **2016,** *324,* 233-238.

150. Wang, Z. G.; Li, Y. M.; Lv, X. J. N-doped ordered mesoporous carbon as a high performance anode material in sodium ion batteries at room temperature. *Rsc Adv* **2014,** *4,* 62673-62677.

151. Jung, J. W.; Lee, C. L.; Yu, S.; Kim, I. D. Electrospun nanofibers as a platform for advanced secondary batteries: a comprehensive review. *J. Mater. Chem. A* **2016,** *4,* 703-750.

152. Wang, H. G.; Yuan, S.; Ma, D. L.; Zhang, X. B.; Yan, J. M. Electrospun materials for lithium and sodium rechargeable batteries: from structure evolution to electrochemical performance. *Energy Environ. Sci.* **2015,** *8,* 1660-1681.

153. Rademacher, J. T.; Kanakarajan, K.; Czarnik, A. W. Improved Synthesis of 1,4,5,8,9,12-Hexaazatriphenylenehexacarboxylic Acid. *Synthesis-Stuttgart* **1994,** 378-380.

154. Kurpil, B.; Savateev, A.; Papaefthimiou, V.; Zafeiratos, S.; Heil, T.; Ozenler, S.; Dontsova, D.; Antonietti, M. Hexaazatriphenylene doped carbon nitrides-Biomimetic photocatalyst with superior oxidation power. *Appl Catal B-Environ* **2017,** *217,* 622-628.

155. Walczak, R.; Kurpil, B.; Savateev, A.; Heil, T.; Schmidt, J.; Qin, Q.; Antonietti, M.; Oschatz, M. Template- and Metal-Free Synthesis of Nitrogen-Rich Nanoporous "Noble" Carbon Materials by Direct Pyrolysis of a Preorganized Hexaazatriphenylene Precursor. *Angew Chem Int Edit* **2018,** *57,* 10765-10770.

156. Thommes, M.; Kaneko, K.; Neimark, A. V.; Olivier, J. P.; Rodriguez-Reinoso, F.; Rouquerol, J.; Sing, K. S. W. Physisorption of gases, with special reference to the evaluation of surface area and pore size distribution (IUPAC Technical Report). *Pure Appl. Chem.* **2015,** *87,* 1051-1069.

157. Neimark, A. V.; Lin, Y. Z.; Ravikovitch, P. I.; Thommes, M. Quenched solid density functional theory and pore size analysis of micro-mesoporous carbons. *Carbon* **2009,** *47,* 1617-1628.

158. Faber, K.; Badaczewski, F.; Oschatz, M.; Mondin, G.; Nickel, W.; Kaskel, S.; Smarsly, B. M. In-Depth Investigation of the Carbon Microstructure of Silicon Carbide-Derived Carbons by Wide-Angle X-ray Scattering. *J. Phys. Chem. C* **2014,** *118,* 15705-15715.

159. Huang, H.; Kundu, D.; Yan, R.; Tervoort, E.; Chen, X.; Pan, L.; Oschatz, M.; Antonietti, M.; Niederberger, M. Fast Na‐Ion Intercalation in Zinc Vanadate for High‐Performance Na‐Ion Hybrid Capacitor. *Adv. Energy Mater.* **2018,** 1802800.

160. Tian, Z. H.; Fechler, N.; Oschatz, M.; Heil, T.; Schmidt, J.; Yuan, S. G.; Antonietti, M. C2NxO1-x framework carbons with defined microporosity and Co-doped functional pores. *J. Mater. Chem. A* **2018,** *6,* 19013-19019.

161. Oschatz, M.; Antonietti, M. A search for selectivity to enable CO2 capture with porous adsorbents. *Energy Environ. Sci.* **2018,** *11,* 57-70.

162. Hao, G. P.; Mondin, G.; Zheng, Z. K.; Biemelt, T.; Klosz, S.; Schubel, R.; Eychmuller, A.; Kaskel, S. Unusual Ultra-Hydrophilic, Porous Carbon Cuboids for Atmospheric-Water Capture. *Angew Chem Int Edit* **2015,** *54,* 1941-1945.

163. Yan, R. Y.; Antonietti, M.; Oschatz, M. Toward the Experimental Understanding of the Energy Storage Mechanism and Ion Dynamics in Ionic Liquid Based Supercapacitors. *Adv. Energy Mater.* **2018,** *8,* 1800026.

164. Zhao, Q. L.; Yang, D. F.; Whittaker, A. K.; Zhao, X. S. A hybrid sodium-ion capacitor with polyimide as anode and polyimide-derived carbon as cathode. *J. Power Sources* **2018,** *396*, 12-18.

165. Luo, J. M.; Fang, C.; Jin, C. B.; Yuan, H. D.; Sheng, O. W.; Fang, R. Y.; Zhang, W. K.; Huang, H.; Gan, Y. P.; Xia, Y.; Liang, C.; Zhang, J.; Li, W. Y.; Tao, X. Y. Tunable pseudocapacitance storage of MXene by cation pillaring for high performance sodium-ion capacitors. *J. Mater. Chem. A* **2018,** *6*, 7794-7806.

166. Zhu, Y. E.; Yang, L. P.; Sheng, J.; Chen, Y. N.; Gu, H. C.; Wei, J. P.; Zhou, Z. Fast Sodium Storage in TiO2@CNT@C Nanorods for High-Performance Na-Ion Capacitors. *Adv. Energy Mater.* **2017,** *7*, 1701222.

167. Babu, B.; Shaijumon, M. M. High performance sodium-ion hybrid capacitor based on Na2Ti2O4(OH)(2) nanostructures. *J. Power Sources* **2017,** *353*, 85-94.

168. Wang, R. T.; Wang, S. J.; Zhang, Y. B.; Jin, D. D.; Tao, X. Y.; Zhang, L. Graphene-coupled Ti3C2 MXenes-derived TiO2 mesostructure: promising sodium-ion capacitor anode with fast ion storage and long-term cycling. *J. Mater. Chem. A* **2018,** *6*, 1017-1027.

169. Ding, J.; Wang, H.; Li, Z.; Cui, K.; Karpuzov, D.; Tan, X.; Kohandehghan, A.; Mitlin, D. Peanut shell hybrid sodium ion capacitor with extreme energy–power rivals lithium ion capacitors. *Energy Environ. Sci.* **2015,** *8*, 941-955.

170. Forse, Alexander C.; Griffin, John M.; Merlet, C.; Carretero-Gonzalez, J.; Raji, A.-Rahman O.; Trease, Nicole M.; Grey, Clare P. Direct observation of ion dynamics in supercapacitor electrodes using in situ diffusion NMR spectroscopy. *Nat. Energy* **2017,** *2*, 16216.

171. Borchardt, L.; Oschatz, M.; Paasch, S.; Kaskel, S.; Brunner, E. Interaction of electrolyte molecules with carbon materials of well-defined porosity: characterization by solid-state NMR spectroscopy. *Phys. Chem. Chem. Phys.* **2013,** *15*, 15177-84.

172. Forse, A. C.; Griffin, J. M.; Wang, H.; Trease, N. M.; Presser, V.; Gogotsi, Y.; Simon, P.; Grey, C. P. Nuclear magnetic resonance study of ion adsorption on microporous carbide-derived carbon. *Phys. Chem. Chem. Phys.* **2013,** *15*, 7722-30.

173. Deschamps, M.; Gilbert, E.; Azais, P.; Raymundo-Pinero, E.; Ammar, M. R.; Simon, P.; Massiot, D.; Beguin, F. Exploring electrolyte organization in supercapacitor electrodes with solid-state NMR. *Nat. Mater.* **2013,** *12*, 351-8.

174. Prehal, C.; Koczwara, C.; Jäckel, N.; Schreiber, A.; Burian, M.; Amenitsch, H.; Hartmann, M. A.; Presser, V.; Paris, O. Quantification of ion confinement and desolvation in nanoporous carbon supercapacitors with modelling and in situ X-ray scattering. *Nat. Energy* **2017,** *2*, 16215.

175. Boukhalfa, S.; He, L.; Melnichenko, Y. B.; Yushin, G. Small-angle neutron scattering for in situ probing of ion adsorption inside micropores. *Angew. Chem. Int. Ed. Engl.* **2013,** *52*, 4618-22.

176. Li, Z.; Jiang, Y.; Yuan, L. X.; Yi, Z. Q.; Wu, C.; Liu, Y.; Strasser, P.; Huang, Y. H. A Highly Ordered Meso@Microporous Carbon-Supported Sulfur@Smaller Sulfur Core-Shell Structured Cathode for Li-S Batteries. *ACS Nano* **2014,** *8*, 9295-9303.

177. Schüth, F. Encapsulation Strategies in Energy Conversion Materials. *Chem. Mater.* **2014,** *26*, 423-434.

178. Cychosz, K. A.; Guillet-Nicolas, R.; Garcia-Martinez, J.; Thommes, M. Recent advances in the textural characterization of hierarchically structured nanoporous materials. *Chem. Soc. Rev.* **2017,** *46*, 389-414.

179. Ambroz, F.; Macdonald, T. J.; Martis, V.; Parkin, I. P. Evaluation of the BET Theory for the Characterization of Meso and Microporous MOFs. *Small Methods* **2018,** 2, 1800173.

180. Weingarth, D.; Zeiger, M.; Jäckel, N.; Aslan, M.; Feng, G.; Presser, V. Graphitization as a Universal Tool to Tailor the Potential-Dependent Capacitance of Carbon Supercapacitors. *Adv. Energy Mater.* **2014,** *4,* 1400316.

8.   List of Publications

8.1.   Peer-reviewed journal publications

[1] **Yan, R.;** Josef, E.; Huang, H.; Leus, K.; Niederberger, M.; Antonietti, M.; Oschatz, M. Understanding the charge storage mechanism to achieve high capacity and fast ion storage in sodium-ion capacitor anodes by using electrospun nitrogen-doped carbon fibers. *Advanced Energy Materials*, under review.

[2] **Yan, R.;** Leus, K.; Antonietti, M.; Oschatz, M. Nitrogen-rich carbon nanoparticles embedded in conductive mesoporous carbon matrix as anode materials for sodium-ion capacitors with high rate capability. In preparation.

[3] Huang, H.; Kundu, D.; **Yan, R.;** Tervoort, E.; Chen, X.; Pan, L.; Oschatz, M.; Antonietti, M.; Niederberger, M. Fast Na-ion intercalation in zinc vanadate for high-performance Na-ion hybrid capacitor. *Advanced Energy Materials*, 2018, DOI: 10.1002/aenm.201802800.

[4] Hwang, J.; **Yan, R.;** Oschatz, M.; Schmidt, B. Solvent Mediated Morphology Control of Zn MOFs as Carbon Templates for Application in Supercapacitors. *Journal of Materials Chemistry A*, 2018, DOI: 10.1039/C8TA07700B

[5] Antonietti, M.; Chen, X.; **Yan, R.;** Oschatz, M. Storing electricity as chemical energy: beyond traditional electrochemistry and double-layer compression. *Energy & Environmental Science*, 2018, DOI: 10.1039/C8EE01723A.

[6] Lama, S.M.; Weber, J.L.; Heil, T.; Hofmann, J.P.; **Yan, R.;** Jong, K.P.; Oschatz, M. Tandem promotion of iron catalysts by sodium-sulfur and nitrogen-doped carbon layers on carbon nanotube supports for the Fischer-Tropsch to olefins synthesis. *Applied Catalysis A: General.* 2018, 568, 213.

[7] Lai, F.; Feng, J.; **Yan, R.;** Wang, G.C.; Antonietti, M.; Oschatz, M. Breaking the limits of ionic liquid-based supercapacitors: mesoporous carbon electrodes functionalized with manganese oxide nanosplotches for dense, stable, and wide-temperature energy storage. *Advanced Functional Materials*, 28, 1801298.

[8] **Yan, R.;** Antonietti, M.; Oschatz, M. Toward the experimental understanding of the energy storage mechanism and ion dynamics in ionic liquid based supercapacitors. *Advanced Energy Materials*, 2018, 1800026.

[9] **Yan, R.;** Heil, T.; Presser. V.; Walczak R.; Antonietti, M.; Oschatz M. Ordered mesoporous carbons with high micropore content and tunable structure prepared by combined hard- and salt-templating as electrode materials in electric double-layer capacitors. *Advanced Sustainable Systems*, 2018, 2, 1700128.

8.2.   Conference contributions

Oral presentations as the presenting author

2018.07.01-07.06   Carbon2018. The World Conference on Carbon, Madrid, Spain
Title: Towards better understanding of ion storage/diffusion mechanism in supercapacitors based on hierarchical porous carbons
R. Yan, M. Oschatz, and M. Antonietti

2018.09.24-09.26   Electrochemistry 2018, Ulm, Germany
Title: Illuminating ion storage and diffusion mechanisms in hierarchical porous carbon materials for supercapacitors
R. Yan, M. Oschatz, and M. Antonietti

Poster presentations as the presenting author

2017.07.10-07.14   5th International Symposium on Enhanced Electrochemical Capacitors, Jena, Germany
Title: Synthesis of ordered mesoporous carbon with high micropore content by combined hard/salt-templating for electric double-layer capacitors
R. Yan, M. Oschatz, and M. Antonietti

2017.09.10-09.14   GDCh Scientific Forum Chemistry 2017 - Anniversary Congress "GDCh - 150 Years", Berlin, Germany
Title: Synthesis of ordered mesoporous carbon with high micropore content by combined hard/salt-templating for electric double-layer capacitors
R. Yan, M. Oschatz, and M. Antonietti

2018.07.16-07.17   AM30 SYMPOSIUM DRESDEN 2018: Advanced Carbon and 2D Materials, Dresden, Germany
Title: New carbon materials and energy storage concepts for ionic-liquid-based supercapacitors
R. Yan, M. Oschatz, and M. Antonietti

9.   Declaration

Die vorliegende Dissertation entstand im Zeitraum zwischen Oktober 2016 und Februar 2019 am Max-Planck-Institut für Kolloid und Grenzflächenforschung unter Betreuung von Prof. Dr. Dr. h.c. Markus Antonietti.

Hiermit erkläre ich, dass die vorliegende Arbeit selbstständig angefertigt wurde und keine anderen als die angegebenen Hilfsmittel und Quellen verwendet wurden.

The present work was carried out during the period from October 2016 to February 2019 at the Max Planck Institute of Colloids and Interfaces under supervision of Prof. Dr. Dr. h.c. Markus Antonietti.

I declare that I have written this work on my own and used no other than the named aids and references.

Runyu Yan

Potsdam, February 2019